

AD-A246 961



2

DOCUMENTATION PAGE

Form Approved
OMB No. 0704-0188

DTIC
ELECT

1b. RESTRICTIVE MARKINGS

2a. SECURITY CLASSIFICATION AUTHORITY

3. DISTRIBUTION/AVAILABILITY OF REPORT
Approved for Public Release;
Distribution Unlimited

2b. DECLASSIFICATION/DOWNGRADING SCHEDULE

4. PERFORMING ORGANIZATION REPORT NUMBER(S)
POLY-WRI-1587-91

5. MONITORING ORGANIZATION REPORT NUMBER(S)
AFOSR-TR- 92 0095

6a. NAME OF PERFORMING ORGANIZATION
Polytechnic University
Weber Research Institute

6b. OFFICE SYMBOL
(if applicable)

7a. NAME OF MONITORING ORGANIZATION
Air Force Office of Scientific Research/NM

6c. ADDRESS (City, State, and ZIP Code)
Route 110
Farmingdale, NY 11735

7b. ADDRESS (City, State, and ZIP Code) Bldg 410
Bolling Air Force Base
Washington, D. C. 20332-6448

8a. NAME OF FUNDING/SPONSORING ORGANIZATION
Air Force Office of Scientific Research

8b. OFFICE SYMBOL
(if applicable)
NM

9. PROCUREMENT INSTRUMENT IDENTIFICATION NUMBER
AFOSR-90-0069

8c. ADDRESS (City, State, and ZIP Code)
Bolling Air Force Base
Washington, D. C. 20332-6448

10. SOURCE OF FUNDING NUMBERS

PROGRAM ELEMENT NO.	PROJECT NO.	TASK NO.	WORK UNIT ACCESSION NO.
6110Q2F	2301	A7	

11. TITLE (Include Security Classification)
"Nonequilibrium Behavior of Carriers in Semiconductors Subjected to Strong Space-Time Varying Fields" (U)

12. PERSONAL AUTHOR(S)
Erich E. Kunhardt

13a. TYPE OF REPORT
Final Technical

13b. TIME COVERED
FROM 12/1/89-11/30/91

14. DATE OF REPORT (Year, Month, Day)
Dec. 1991

15. PAGE COUNT
82

16. SUPPLEMENTARY NOTATION

17. COSATI CODES

FIELD	GROUP	SUB-GROUP

18. SUBJECT TERMS (Continue on reverse if necessary and identify by block number)

19. ABSTRACT (Continue on reverse if necessary and identify by block number)
During this funding period, the macrokinetic theory for electron transport (developed for semiconductors during the previous funding period) has been implemented for multi-valley semiconductor. The model has been applied to GaAs subjected to rapidly varying (in time) fields. The set of material parameters used has been obtained by minimizing the error between calculated and measured transport parameters over the range of values of applied field for which experimental results are available. An experimental facility for investigating the transient dynamics of high power semiconducting switches has been established.

20. DISTRIBUTION/AVAILABILITY OF ABSTRACT
 UNCLASSIFIED/UNLIMITED SAME AS RPT. DTIC USERS

21. ABSTRACT SECURITY CLASSIFICATION
Unclassified

22a. NAME OF RESPONSIBLE INDIVIDUAL
Lt Col James A. Lupo

22b. TELEPHONE (Include Area Code)
202/767-4939

22c. OFFICE SYMBOL
NM

UNCLASSIFIED

I. Overview of Research Program

High Power Semiconductor Switches (HPSS) have received considerable attention for the promise they offer to pulse power technologies. This promise is founded on the fact that with semiconducting materials as the switching medium, it is in principle possible to obtain: a) high current densities over large areas, b) conductivity modulation over several orders of magnitude, and c) high dielectric field strengths. Optically or electrically triggered bulk and junction devices are being investigated in a variety of geometries and covering a wide range of parameters. Semiconducting materials that have been considered are Si, GaAs, and very recently, diamond. Because of its high mobility and hold-off voltage, GaAs devices have been the focus of most of the effort. However, a major difficulty has surfaced with regards to the forward voltage drop of GaAs devices in the on-state. That is, the phenomenon of lock-on; upon switching, the device evolves into a self-sustaining state characterized by a constant voltage with high average field ($\geq 4 \text{ kV/cm}$); and consequently, intolerable losses. A number of possible causes have been proposed involving either contact or bulk properties of the devices. However, the physics behind this phenomenon is yet to be understood.

With AFOSR support, our research activities have focused on developing theoretical models and experimental diagnostic techniques for investigating this and other transient characteristics of these devices. Our aim has been to develop a quantitative understanding of the role of the various microscopic processes, material parameters, traps, and space-charge in shaping the behavior of the devices. During this contract period, we have developed a non-equilibrium model for describing the dynamics of carriers in multi-valley semiconductors. This model has been applied to GaAs devices subjected to rapidly varying (in time) fields. A code developed during the previous contract period has been used to obtain a set of material parameters for

92 5 05 044

92-05571



GaAs by minimizing the error between calculated and measured values for transport parameters. The experimental facility to investigate the dynamics of switching, in particular space-charge redistribution, has also been completed during this period. In the next section a summary of the accomplishments made during the period of this contract is given. Sections III-V are devoted to a discussion of the results.

II. Review of Achievements and Activities During the Contract Period

During this funding period, we have accomplished the following:

(1) The concept of a macrokinetic distribution (MKD) developed in the previous contract period to describe the non-equilibrium dynamics of carriers in single-valley semiconductors, has been extended to multi-valley semiconductors. A two-valley model has been implemented and the results compared to those obtained using Monte Carlo methods. Excellent agreement has been obtained in situations where a single valley model is inadequate due to significant inter-valley carrier transfer. The macro-kinetic model is considerably easier to implement numerically than those based on the Boltzmann transport equation and requires orders of magnitude less computer time to run. The theory is presented in Sec. III.

(2) The theory described above has been successfully applied to modeling of electron transport in GaAs subjected to rapidly varying fields. This scheme provides an efficient scheme for device modeling, and overcomes the difficulty of evaluating the relaxation times in multi-valley conservation equations without a priori assumption of a displaced-Maxwellian distribution for the carriers. This application is discussed in Sec. IV.

(3) The modelling of charge transport in GaAs requires a number of material parameters, such as the effective mass, acoustic deformation potential, various phonon energies, energy separation between valleys, inter-valley and intra-valley deformation potentials, etc. At present, there are large uncertainties in the

experimental and theoretical values for some of these parameters. The Monte Carlo code developed in the previous funding period has been modified to develop a set of material parameters for GaAs by minimizing the error between calculated and measured values of the transport parameter over the range of applied electric fields for which experimental results are available. This investigation and the results obtained are presented in Sec. V.

(4) The experimental facility to investigate the dynamics of field collapse in high power photoconductive switches has been completed and preliminary results have been obtained. A discussion of the facility is presented in Appendix A.

Published Papers:

1. "A Theory of Nonequilibrium Carrier Transport in Multi-valley Semiconductors," J. Appl. Phys. 67, 1807 (1990).
2. "A Transport Model for Carriers in Small Spatial/Temporal Scale Compound Semiconductor Devices," Int. J. Comp. and Math. in E.E.E., December 1991.
3. "Monte Carlo Investigation of Acoustic, Inter-valley and Intra-valley Deformation Potentials for GaAs," Solid State Communications, 79, 651 (1991).

A number of presentations were also made during this period. Abstracts are given in Appendix B. Also during this period, one student (M. Cheng) received his Ph.D. and is currently on the faculty at the University of New Orleans. A postdoctoral fellow (A. Garvie) joined the research and has been responsible for setting up the experimental facility.



Accession For	
NTIS Grant	<input checked="" type="checkbox"/>
DTIC Tab	<input type="checkbox"/>
Unannounced	<input type="checkbox"/>
Justification	
By	
Distribution/	
Availability Codes	
Dist	Avail and/or Special
A-1	

III. A Theory of Nonequilibrium Carrier Transport in Multivalley Semiconductors

I. INTRODUCTION

The observation of the Gunn effect^{1,2} confirmed the prediction^{3,4} of electron transfer between light-mass and heavy-mass valleys in GaAs and InP. This transfer has subsequently been found^{5,6} to have a significant influence on electron transport in multivalley semiconductors, particularly in nonequilibrium conditions and also at fields where intervalley scattering is a dominant process. For example, in high-frequency devices with a short active channel, the intervalley transitions play an important role near the cathode contact.⁵ This can generally be said of any device with small temporal and/or spatial scale. Similarly, the velocity-under-shoot behavior⁶ of electrons in GaAs subjected to a picosecond pulse electric field is explained, in part, in terms of the electron transfer from upper valleys to the central valley, which scattering process results in a randomization of the momentum.

At the kinetic level, the semiclassical description of carrier dynamics in multivalley semiconductors is given in terms of the phase-space distribution functions for the carriers in each valley. These distributions obey Boltzmann transport equations (BTEs) that are coupled by intervalley scattering processes. Difficulties in dealing with the scattering terms in the coupled system of equations make this approach unattractive. To simplify the problem, these terms have been approximated by using the relaxation approximation for both intervalley and intravalley scatterings^{7,8}; however, this approach loses its generality at high fields. An alternate procedure to the BTE for obtaining the distribution function in each valley is to use Monte Carlo (MC) methods. Although easy to implement, this procedure is computationally time consuming, particularly for device simulations.

A number of approaches have been proposed with the objective of obtaining a model that is easier to implement while including the pertinent physics. Most of them make use⁹⁻¹⁴ of a finite set of moments of the BTE. The difficulty in implementing this approach is the determination of the

unknown coefficients appearing in the truncated moment equations. This is especially true in multivalley semiconductors, which require a set of moment equations for each valley. The difficulty has resulted in the fact that most treatments of transport in multivalley semiconductors using moment equations assume only a single valley. In this approximation, a single distribution function, averaged over the valleys, is taken to represent the distributions in all valleys; consequently, the moments correspond to averages over the valleys. Moreover, with this distribution, the unknown coefficients in the "equivalent" single-valley moment equations can be easily evaluated.⁹ However, the dynamics of carrier transfer are not properly taken into account when using this single-valley description.^{6,11,14} As an alternative, and in order to keep a multivalley description, the assumption is made that the distribution function in each valley is a (different) displaced Maxwellian distribution.^{5,15,16} These distributions are then used to evaluate the unknown coefficients in the moment equations for each valley. However, this assumption is rather severe, since the distribution may be appreciably different from a displaced Maxwellian in some semiconductors.¹⁷⁻¹⁹

In this paper a theory of nonequilibrium carrier transport in multivalley semiconductors is presented. It is based on the concept of a macrokinetic distribution (MKD)^{14,20,21} and on moments of the BTE. No *a priori* assumptions are made in this theory about the shape of the carrier distribution in momentum, \mathbf{k} , space. The MKD is a momentum-dependent function with macroscopic space-time scales and obeys an equation that is macroscopically equivalent to the BTE. The MKD can also be obtained using MC methods. The unknown parameters and rates appearing in the multivalley moment equations can be evaluated using the MKD. It is shown that in the case of strong intervalley transitions, the single-valley description does not account for energy and momentum exchanges between valleys. This leads to a significant difference between the multi- and single-valley behavior for the relaxation of mean energy and momentum.¹⁴ For simplicity, a semiconductor test model is set up to develop the theoretical details of the macrokinetic model and to

carry out the numerical calculations. The band structure and the scattering mechanisms used in this model are given in the Appendix. Results are presented for the response of electrons to a step change in electric field and compared to those obtained using MC methods and an equivalent single-valley model.

In the next section, a brief overview of the macrokinetic theory for a single-valley band is given. The multivalley description is shown in Sec. III. In Sec. IV the results and comparisons are presented. Concluding remarks are given in Sec. V.

II. THE MACROKINETIC MODEL

This model has been discussed for a single-valley band in a previous paper¹⁴; consequently, only a brief description is presented here. It is *a priori* assumed that for the situation of interest a finite set of moment equations can be used to describe carrier behavior. A MKD, f_M , is introduced that is macroscopically equivalent to the microscopic phase-space distribution, $f(\mathbf{k}, \mathbf{r}, t)$. The f_M obeys an equation¹⁴ that is equivalent to the BTE in the space-time scale of the moment equations. The equation for f_M and the moment equations constitute the model. This set can be used to describe the nonequilibrium behavior of carriers in the time scale corresponding to the characteristic times in the moment equations.

Since $\tau > \tau_e > \tau_m$ in semiconductors, where τ , τ_e , and τ_m are carrier density, energy, and momentum relaxation times, respectively, the moment equations can be ordered and a finite set selected depending on the level of description or degree of space-time coarseness desired in the model. To a given finite set of moment equations corresponds a MKD that serves to close the set. The equation for this MKD is obtained from the BTE. For a single-valley band, the BTE is written as

$$\partial_t f + \mathbf{v} \cdot \nabla f + \frac{q\mathbf{E}}{\hbar} \cdot \nabla_{\mathbf{k}} f = \left[\frac{\partial f}{\partial t} \right]_c, \quad (1)$$

where \mathbf{v} is the velocity and \mathbf{E} is the electric field. The corresponding first three moment equations for the single valley are

$$\partial_t n + \nabla \cdot (n\mathbf{u}) = n/\tau, \quad (2a)$$

$$\partial_t (n\bar{\epsilon}) + \nabla \cdot (\epsilon \mathbf{v}) - qn\mathbf{E} \cdot \mathbf{u} = - [n(\bar{\epsilon} - \epsilon_0)/\tau_e], \quad (2b)$$

$$\partial_t (n\bar{\mathbf{p}}) + \nabla \cdot (\mathbf{p} \cdot \mathbf{v}) - qn\mathbf{E} = - (n\bar{\mathbf{p}}/\tau_m), \quad (2c)$$

where the bracket represents an average over the distribution, n is the carrier density, \mathbf{u} is the average velocity, $\bar{\epsilon}$ is the mean energy, $\bar{\mathbf{p}}$ is the average momentum, and ϵ_0 is the thermal energy. The carrier density, energy, and momentum relaxation times are defined by

$$\frac{n}{\tau} = \int \left(\frac{\partial f}{\partial t} \right)_c d\mathbf{k}, \quad (3a)$$

$$- \frac{n(\bar{\epsilon} - \epsilon_0)}{\tau_e} = \int \epsilon \left(\frac{\partial f}{\partial t} \right)_c d\mathbf{k}, \quad (3b)$$

$$- \frac{n\bar{\mathbf{p}}}{\tau_m} = \int \mathbf{p} \left(\frac{\partial f}{\partial t} \right)_c d\mathbf{k}. \quad (3c)$$

Subsequently, the various levels of description that can be obtained using Eqs. (2) are discussed.

A. The S_1 description, valid for time scale $\geq \tau$

In this time scale, the dynamics of the carriers can be described by Eq. (2a). Consequently, the corresponding MKD is taken to have the same space-time dependence as the carrier density; that is,

$$f(\mathbf{k}, \mathbf{r}, t) = f_M^{(1)}[\mathbf{k}, n(\mathbf{r}, t)]. \quad (4)$$

Using Eqs. (2a) and (4) in Eq. (1), the equation for $f_M^{(1)}$ is obtained. Solving for $f_M^{(1)}$ and using it to evaluate \mathbf{u} and τ in Eq. (2a) leads to the well-known drift-diffusion equation for $n(\mathbf{r}, t)$. That is,

$$n\mathbf{u} = n\mu\mathbf{E} - D\nabla n, \quad (5)$$

where μ is the mobility and D is the diffusion coefficient and are obtained in terms of the known function $f_M^{(1)}$.¹⁴

B. The S_2 description, valid for time scale $\geq \tau_e$

In this case, the description is in terms of a MKD that depends on the carrier density and mean energy,

$$f(\mathbf{k}, \mathbf{r}, t) = f_M^{(2)}[\mathbf{k}, n(\mathbf{r}, t), \bar{\epsilon}(\mathbf{r}, t)], \quad (6)$$

and the corresponding first two moment equations [Eqs. (2a) and (2b)]. The equation for $f_M^{(2)}$ has been shown¹⁴ to be, for uniform conditions,

$$qE_{\text{eq}} \partial_{\mathbf{k}} f_M^{(2)} = \left(\frac{\partial f_M^{(2)}}{\partial t} \right)_c, \quad (7a)$$

where

$$qE_{\text{eq}} = [\bar{\epsilon}(t) - \epsilon_0]/u_s \tau_e, \quad (7b)$$

with

$$nu_s = \int f_M^{(2)}(\mathbf{k}, n, \bar{\epsilon}) \mathbf{v} d\mathbf{k}. \quad (7c)$$

Equation (7a) represents a system that obeys a steady-state BTE with an equivalent field, E_{eq} , as the driving force. u_s is the "steady-state" average velocity that is seen to depend on the time-varying mean energy. Equation (7c) implies that in this description the mean momentum of carriers responds instantaneously to an equivalent field, E_{eq} .

The unknown rates in Eqs. (2a) and (2b) can be obtained in terms of the mean energy by evaluating the integrals in Eqs. (3a) and (3b) using the MKD obtained from Eq. (7a). The S_2 MKD can be obtained, for example, from MC simulations and the rates tabulated as functions of the mean energy or equivalent field. For a given problem, it is then only necessary to solve Eqs. (2a) and (2b).

C. The S_3 description, valid for time scale $\geq \tau_m$

The system of equations that describe the system in this time scale consists of the first three moment equations [Eqs. (2a)–(2c)] of the BTE and the corresponding MKD, which

is taken to depend on carrier density, mean energy, and average momentum:

$$f(\mathbf{k}, \mathbf{r}, t) = f_M^{(3)}[\mathbf{k}, n(\mathbf{r}, t), \bar{\epsilon}(\mathbf{r}, t), \bar{\mathbf{k}}(\mathbf{r}, t)].$$

In a previous paper,¹⁴ a relaxation process is used to model the evolution of the smaller time-scale distribution ($f_M^{(3)}$) into the larger time-scale distribution ($f_M^{(2)}$). An alternative is to approximate $f_M^{(3)}$ with $f_M^{(2)}$ in the evaluation of the averaged rates [Eqs. (3a)–(3c)]. This simple approach is valid when the momentum relaxation time is relatively small compared to the energy relaxation time. It is, in general, true for GaAs and Si unless the situation is considered at relatively low fields.^{6,22} Similarly to the S_1 and S_2 descriptions, the unknown coefficients in Eqs. (2a)–(2c) can be evaluated using $f_M^{(3)}$.

III. THE MULTIVALLEY DESCRIPTION

For simplicity a two-valley model is used to illustrate the theory. The BTEs for this model, assuming spatial uniformity, are given by

$$\begin{aligned} \partial_t f_1 + \frac{q\mathbf{E}}{\hbar} \cdot \nabla_{\mathbf{k}} f_1 &= \left(\frac{\partial f_1}{\partial t} \right)_{\text{intra}} + \left(\frac{\partial f_1}{\partial t} \right)_{1,\text{inter}} \\ &+ \left(\frac{\partial f_2}{\partial t} \right)_{1,\text{inter}}, \end{aligned} \quad (8a)$$

$$\begin{aligned} \partial_t f_2 + \frac{q\mathbf{E}}{\hbar} \cdot \nabla_{\mathbf{k}} f_2 &= \left(\frac{\partial f_2}{\partial t} \right)_{\text{intra}} + \left(\frac{\partial f_2}{\partial t} \right)_{2,\text{inter}} \\ &+ \left(\frac{\partial f_1}{\partial t} \right)_{2,\text{inter}}, \end{aligned} \quad (8b)$$

where $f_i(\mathbf{k}_i)$, is the distribution function in the i th valley,

$$\begin{aligned} \left(\frac{\partial f_i}{\partial t} \right)_{\text{intra}} &= \int P_{ii}(\mathbf{k}'_i, \mathbf{k}_i) f_i(\mathbf{k}'_i) d\mathbf{k}'_i \\ &- \int P_{ii}(\mathbf{k}_i, \mathbf{k}'_i) f_i(\mathbf{k}_i) d\mathbf{k}'_i, \end{aligned}$$

$$\left(\frac{\partial f_i}{\partial t} \right)_{i,\text{inter}} = - \int P_{ij}(\mathbf{k}_i, \mathbf{k}_j) f_i(\mathbf{k}_i) d\mathbf{k}_j,$$

$$\left(\frac{\partial f_j}{\partial t} \right)_{i,\text{inter}} = \int P_{ji}(\mathbf{k}_j, \mathbf{k}_i) f_j(\mathbf{k}_j) d\mathbf{k}_i,$$

with $ij = 1, 2$. The transition rates per state, P_{ij} , are given in the Appendix. The first term on the right-hand side of Eqs. (8) represents the electron-phonon collisions inside the same valley, and the last two terms represent the intervalley transitions.

The conservation (macroscopic) equation corresponding to a microscopic physical quantity, $\phi_i(\mathbf{k}_i)$, defined in each valley can be obtained by averaging over the distribution and using the BTE. The resulting equation is

$$\begin{aligned} \partial_t \langle \phi_i \rangle + \frac{q\mathbf{E}}{\hbar} \cdot \langle \nabla_{\mathbf{k}} \phi_i \rangle \\ = \left(\frac{\partial \langle \phi_i \rangle}{\partial t} \right)_{\text{intra}} + \left(\frac{\partial \langle \phi_i \rangle}{\partial t} \right)_{i,\text{inter}}, \end{aligned}$$

where

$$\langle \phi_i \rangle = \int f_i(\mathbf{k}_i) \phi_i(\mathbf{k}_i) d\mathbf{k}_i = n_i \bar{\phi}_i,$$

$$\begin{aligned} \left(\frac{\partial \langle \phi_i \rangle}{\partial t} \right)_{i,\text{inter}} &= \left(\frac{\partial \langle \phi_i \rangle}{\partial t} \right)_{i,\text{inter}} \\ &+ \left(\frac{\partial \langle \phi_j \rangle}{\partial t} \right)_{i,\text{inter}}, \end{aligned}$$

and $\langle \phi \rangle = n \bar{\phi} = n_1 \bar{\phi}_1 + n_2 \bar{\phi}_2$. For $\phi_i = 1$, $\hbar \mathbf{k}_i$, and ϵ , the moment equations for density, average momentum, and mean energy are obtained.

A. Density conservation equations, $\phi(\mathbf{k}_i) = 1$

$$\partial_t n_1 = n_2 \nu_{21} - n_1 \nu_{12}, \quad (9a)$$

$$\partial_t n_2 = n_1 \nu_{12} - n_2 \nu_{21}, \quad (9b)$$

where

$$\begin{aligned} n_1 \nu_{12} &= - \left(\frac{\partial n_1}{\partial t} \right)_{1,\text{inter}} = \left(\frac{\partial n_1}{\partial t} \right)_{2,\text{inter}} \\ &= \int P_{12}(\mathbf{k}_1, \mathbf{k}_2) f_1(\mathbf{k}_1) d\mathbf{k}_1 d\mathbf{k}_2, \end{aligned} \quad (10a)$$

$$\begin{aligned} n_2 \nu_{21} &= \left(\frac{\partial n_2}{\partial t} \right)_{1,\text{inter}} = - \left(\frac{\partial n_2}{\partial t} \right)_{2,\text{inter}} \\ &= \int P_{21}(\mathbf{k}_2, \mathbf{k}_1) f_2(\mathbf{k}_2) d\mathbf{k}_1 d\mathbf{k}_2. \end{aligned} \quad (10b)$$

Therefore, the total intervalley transition for carrier density in the multivalley system vanishes. That is,

$$\left(\frac{\partial n}{\partial t} \right)_{\text{inter}} = \left(\frac{\partial n}{\partial t} \right)_{1,\text{inter}} + \left(\frac{\partial n}{\partial t} \right)_{2,\text{inter}} = 0,$$

where $n = n_1 + n_2$. This implies that in the S_1 regime, where the time scale of interest is much greater than energy and momentum relaxation times, the single-valley description is sufficient to determine carrier behavior in multivalley semiconductors.

B. Momentum conservation equation, $\phi_i(\mathbf{k}_i) = \hbar \mathbf{k}_i = \mathbf{p}_i$

$$\partial_t (n_1 \bar{p}_1) - qEn_1 = - \frac{n_1 \bar{p}_1}{\tau_{m11}} - \frac{n_1 \bar{p}_1}{\tau_{m12}}, \quad (11a)$$

$$\partial_t (n_2 \bar{p}_2) - qEn_2 = - \frac{n_2 \bar{p}_2}{\tau_{m22}} - \frac{n_2 \bar{p}_2}{\tau_{m21}}, \quad (11b)$$

where

$$- \frac{n_i \bar{p}_i}{\tau_{mii}} = \left(\frac{\partial \langle \mathbf{p}_i \rangle}{\partial t} \right)_{\text{intra}} = - \int \frac{\mathbf{p}_i f_i(\mathbf{k}_i)}{\tau_{ii}(\mathbf{k}_i)} d\mathbf{k}_i, \quad (12a)$$

$$- \frac{n_i \bar{p}_i}{\tau_{mij}} = \left(\frac{\partial \langle \mathbf{p}_i \rangle}{\partial t} \right)_{i,\text{inter}} = - \int \frac{\mathbf{p}_i f_i(\mathbf{k}_i)}{\tau_{ij}(\mathbf{k}_i)} d\mathbf{k}_i, \quad (12b)$$

$$\left(\frac{\partial \langle \mathbf{p}_i \rangle}{\partial t} \right)_{i,\text{inter}} = 0,$$

with

$$\frac{1}{\tau_{ij}(\mathbf{k}_i)} = \int P_{ij}(\mathbf{k}_i, \mathbf{k}_j) d\mathbf{k}_j,$$

$$\frac{1}{\tau_{ii}(\mathbf{k}_i)} = \int P_{ii}(\mathbf{k}_i, \mathbf{k}'_i) d\mathbf{k}'_i.$$

τ_{ii}^{-1} and τ_{ij}^{-1} , given in the Appendix, are the intravalley and intervalley scattering rates, respectively. τ_{mii} and τ_{mij} are the intravalley and intervalley momentum exchange times, respectively. The total intervalley momentum exchange rate in this model is given by

$$\left(\frac{\partial \langle \mathbf{p} \rangle}{\partial t}\right)_{\text{inter}} = -\frac{n_1 \bar{p}_1}{\tau_{m12}} - \frac{n_2 \bar{p}_2}{\tau_{m21}}, \quad (13)$$

where $\langle \mathbf{p} \rangle = n\bar{p} = n_1 \bar{p}_1 + n_2 \bar{p}_2$ and $\bar{p}_i = m_i u_i$. In the case of strong intervalley transitions, τ_{ij}^{-1} is comparable to τ_{ii}^{-1} , and thus from Eqs. (12a) and (12b) τ_{mij}^{-1} is comparable to τ_{mii}^{-1} . Consequently, the total intervalley momentum exchange rate [Eq. (13)] is comparable to the total intravalley momentum exchange per unit time which is given by

$$\left(\frac{\partial \langle \mathbf{p} \rangle}{\partial t}\right)_{\text{intra}} = -\frac{n_1 \bar{p}_1}{\tau_{m11}} - \frac{n_2 \bar{p}_2}{\tau_{m22}}.$$

Note that the single-valley approximation does not properly account for the momentum exchange between valleys.

C. Energy conservation equation, $\phi_i(\mathbf{k}_i) = \epsilon$

$$\partial_t (n_1 \bar{\epsilon}_1) - qEn_1 u_1 = -\frac{n_1 (\bar{\epsilon}_1 - \epsilon_0)}{\tau_{\epsilon 11}} + \frac{n_2 \bar{\epsilon}_2}{\tau_{\epsilon 121}} - \frac{n_1 \bar{\epsilon}_1}{\tau_{\epsilon 112}}, \quad (14a)$$

$$\partial_t (n_2 \bar{\epsilon}_2) - qEn_2 u_2 = -\frac{n_2 (\bar{\epsilon}_2 - \epsilon_0)}{\tau_{\epsilon 22}} + \frac{n_1 \bar{\epsilon}_1}{\tau_{\epsilon 212}} - \frac{n_2 \bar{\epsilon}_2}{\tau_{\epsilon 221}}, \quad (14b)$$

where the intravalley and intervalley energy exchange times, $\tau_{\epsilon ii}$ and $\tau_{\epsilon ij}$, respectively, are defined as

$$\begin{aligned} \frac{n_i (\bar{\epsilon}_i - \epsilon_0)}{\tau_{\epsilon ii}} &= \left(\frac{\partial \langle \epsilon_i \rangle}{\partial t}\right)_{\text{intra}} \\ &= \int d\mathbf{k}'_i \int d\mathbf{k}_i \epsilon_i P_{ii}(\mathbf{k}'_i, \mathbf{k}_i) f_i(\mathbf{k}'_i) \\ &\quad - \int d\mathbf{k}_i \frac{\epsilon_i f_i(\mathbf{k}_i)}{\tau_{ii}(\mathbf{k}_i)}, \end{aligned} \quad (15a)$$

$$-\frac{n_j \bar{\epsilon}_j}{\tau_{\epsilon ij}} = \left(\frac{\partial \langle \epsilon_j \rangle}{\partial t}\right)_{\text{inter}} = - \int d\mathbf{k}_j \frac{\epsilon_j f_j(\mathbf{k}_j)}{\tau_{ij}(\mathbf{k}_j)}, \quad (15b)$$

$$\begin{aligned} \frac{n_j \bar{\epsilon}_j}{\tau_{\epsilon j}} &= \left(\frac{\partial \langle \epsilon_j \rangle}{\partial t}\right)_{\text{inter}} \\ &= \int d\mathbf{k}_j \frac{\epsilon_j + \Delta\epsilon_j \mp \hbar\omega_j}{\tau_{jj}(\mathbf{k}_j)} f_j(\mathbf{k}_j). \end{aligned} \quad (15c)$$

The phonon energy, $\hbar\omega_j$, and the energy separation between valleys, $\Delta\epsilon_j$, are given in the Appendix. It is noted that

$\tau_{\epsilon 121} \neq \tau_{\epsilon 221}$ and $\tau_{\epsilon 112} \neq \tau_{\epsilon 212}$, even in the case where $\Delta\epsilon_j$ equals zero since $\hbar\omega_j \neq 0$. The total energy exchange per unit time between valleys is

$$\left(\frac{\partial \langle \epsilon \rangle}{\partial t}\right)_{\text{inter}} = \frac{n_2 \bar{\epsilon}_2}{\tau_{\epsilon 121}} - \frac{n_2 \bar{\epsilon}_2}{\tau_{\epsilon 221}} + \frac{n_1 \bar{\epsilon}_1}{\tau_{\epsilon 212}} - \frac{n_1 \bar{\epsilon}_1}{\tau_{\epsilon 112}} \quad (16a)$$

or

$$\begin{aligned} \left(\frac{\partial \langle \epsilon \rangle}{\partial t}\right)_{\text{inter}} &= \Delta\epsilon_{21} (n_2 v_{21} - n_1 v_{12}) \\ &\quad + \hbar\omega_{21} n_2 (v_{21ab} - v_{21em}) \\ &\quad + \hbar\omega_{12} n_1 (v_{12ab} - v_{12em}), \end{aligned} \quad (16b)$$

where v_{ijem} (v_{ijab}) is the averaged transition rate from the i th to j th valley through the process of phonon emission (absorption), and given by Eq. (10) with only the phonon emission (absorption) transition rate. The first term on the right-hand side RHS of Eq. (16b) equals $\Delta\epsilon_{21} \partial_t n_1$, and does not vanish for $\Delta\epsilon_{21} \neq 0$ unless carriers are in equilibrium between valleys. This clearly shows that for semiconductors with $\Delta\epsilon_j \neq 0$ the mean energy can only reach steady state in the same scale as the carrier density in each valley. The second and third terms on the RHS of Eq. (16b) are significant in comparison to the intravalley energy exchange when the intervalley transition is dominant. Again, the dynamics of energy exchange between valleys is not properly taken into account when using a single-valley description.

To obtain the carrier density, mean energy, and momentum from the multivalley moment equations, the (unknown) averaged rates [Eqs. (9), (11), and (14)] have to be determined. To do so and proceeding as for a single-valley band (Sec. II), the MKD in the i th valley, f_{Mi} , is used to directly evaluate Eqs. (10), (12), and (15) (this is not necessary in practice for a single-valley band since the desired rates can also be calculated using the steady-state equations if the steady-state moments are known^{9,14}). Depending on the time scale of interest, the MKD and the corresponding macrokinetic equation in each valley can be obtained for each level of description as shown in Sec. II. In the next section, results are presented using an S_3 description (in the momentum scale) with an S_2 MKD, $f_{Mi}^{(2)}$, i.e., with $f_{Mi}^{(3)} \approx f_{Mi}^{(2)}$, $f_{Mi}^{(2)}$ can be obtained in terms of mean energy from MC methods and the integrals [Eqs. (10), (12), and (15)] can be similarly determined. The resulting (closed) set of moment equations constitute a model of nonequilibrium carrier transport in multivalley semiconductors.

IV. RESULTS

Results are presented in this section for the band model discussed in Sec. III. This band model has two different valleys with effective masses equal to $0.08m_0$ (lower valley) and $0.3m_0$ (upper valley), respectively, where m_0 is the free-electron mass. The ϵ - \mathbf{k} relation of carriers in each valley is characterized by

$$\epsilon_i = \hbar^2 k_i^2 / 2m_i.$$

The results obtained with this model are also compared to those obtained using a single-valley "equivalent" description¹⁴ and multivalley MC simulations.¹⁷ For further sim-

plification, a test model is also used for the k -space transition rates. The scattering model is given in the Appendix. These transition rates are used in all the calculations presented in this paper.

To illustrate the dynamics of the carriers in multivalley semiconductors, the transient behavior of electrons (in the test model) influenced by a step change in electric field is presented. The applied field is along the z direction and equal to E_1 for $t < t_1$ and E_2 for $t > t_1$. For $t < t_1$, the system is in steady state. A finite difference technique²³ has been used to solve the moment equations for the single-valley descriptions [Eqs. (2a)–(2c) without space dependence] and for the multivalley description [Eqs. (9), (11), and (14)].

In the first example, $E_1 = 5$ kV/cm, $E_2 = 15$ kV/cm, and $t_1 = 0.3$ ps. The behavior in time of the total mean energy and average velocity obtained from numerical solutions in Eqs. (9), (11), and (14) are shown in Fig. 1. The rates in these equations are evaluated from the integrals, Eqs. (10), (12), and (15) using the MKD in each valley. The MKD is obtained from MC simulations in term of energy, as dis-

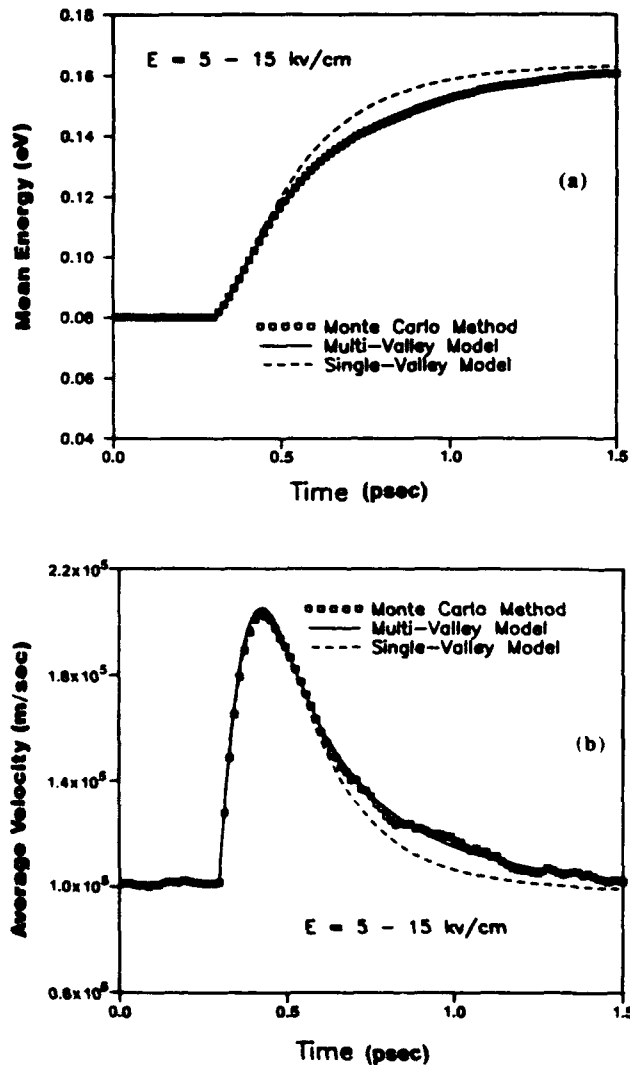


FIG. 1. Evolution of total mean energy and average velocity as a consequence of a step change in applied field from 5 to 15 kV/cm. (a) Mean energy and (b) average velocity.

cussed in Sec. II. The results obtained using other methods are also shown. It can be seen that the single-valley variables respond to the change in electric fields faster than those corresponding to a multivalley model (both the moment description and the MC method). Moreover, the transient energy and velocity obtained from the multivalley moment equations based on the macrokinetic model are in excellent

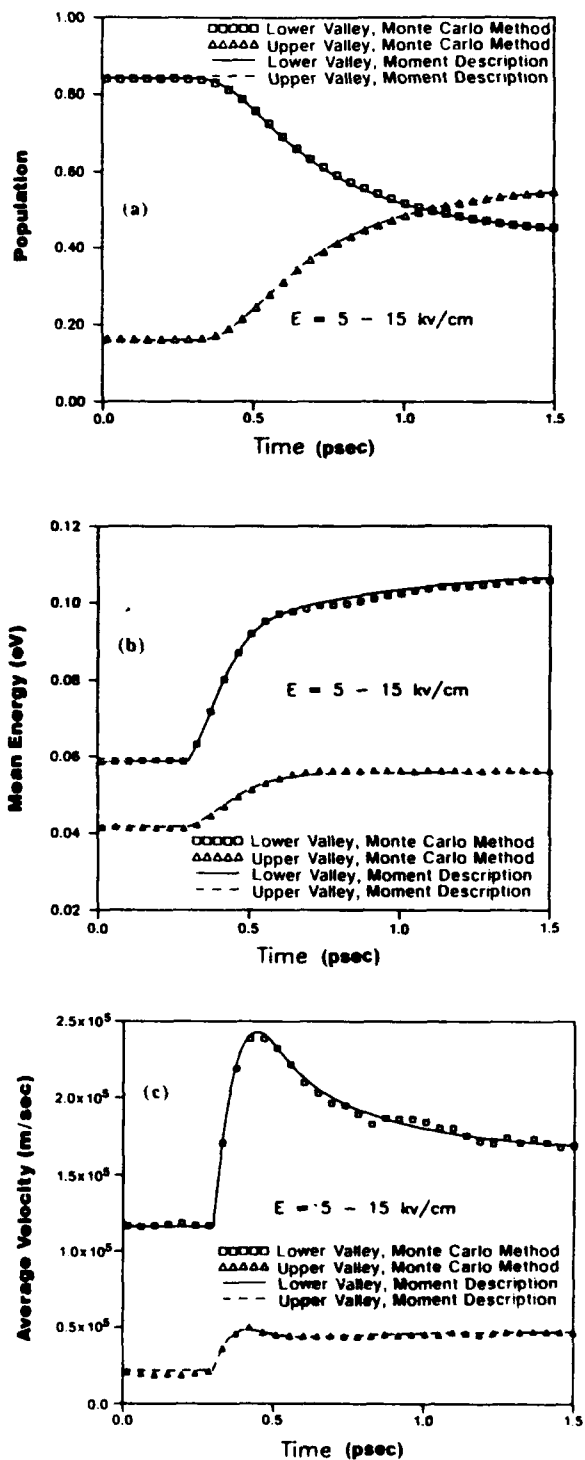


FIG. 2. Evolution of normalized population, mean energy, and average velocity of the carriers in each valley as a consequence of a step change in applied field. Same conditions as Fig. 1. (a) Population, (b) mean energy, and (c) average velocity.

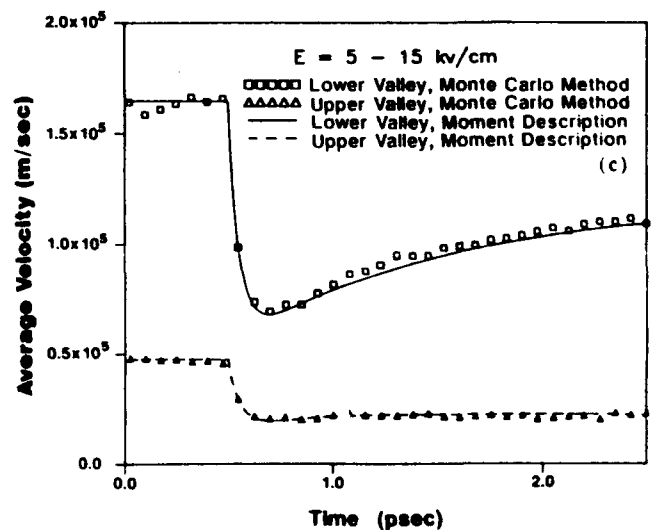
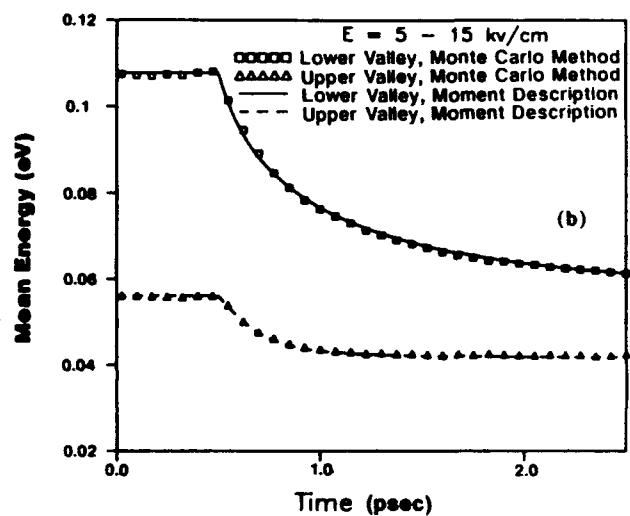
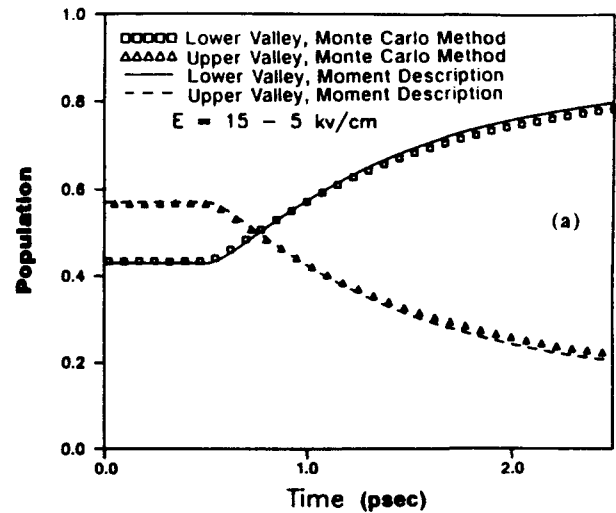
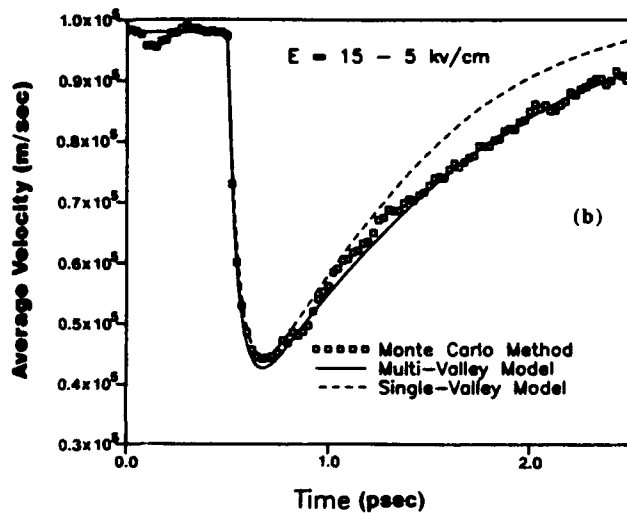
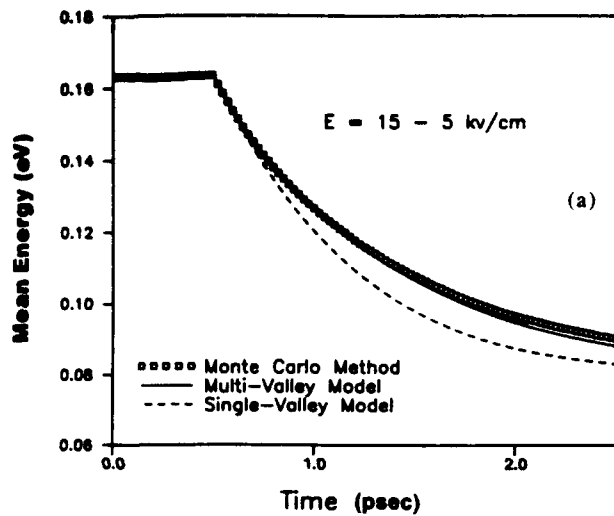


FIG. 3. Evolution of total mean energy and average velocity of the test model as a consequence of a step change in applied field from 15 to 5 kV/cm. (a) Mean energy and (b) average velocity.

agreement with those obtained from MC calculations (see Fig. 1).

The slower carrier relaxation observed using a multivalley description as compared to a single-valley description can be explained with the aid of Eqs. (13) and (16b). The slowest time scale in the model is that of the carrier density. The slow response of the carrier density to changes in the field [see Fig. 2(a)] influences the change in mean energy through the first term on the RHS of Eq. (16b), and thus the velocity response since the moment relaxation times are strongly dependent on energy. In the case of strong intervalley transitions, the intervalley momentum and energy exchanges in Eq. (13) and the last two terms in Eq. (16b) also determine the dynamical evolution of energy and momentum. The evolution of carrier density, mean energy, and average velocity in each valley is shown in Fig. 2. This also shows excellent agreement between the macrokinetic model using a multivalley description and the MC method.

Similar comparisons are shown in Figs. 3 and 4 for a step change in field from $E_1 = 15$ kV/cm to $E_2 = 5$ kV/cm and

FIG. 4. Evolution of normalized population, mean energy, and average velocity of carriers in each valley as a consequence of a step change in applied field. Same conditions as Fig. 3. (a) Population, (b) mean energy, and (c) average velocity.

$t_1 = 0.5$ ps. The slower responses of mean energy and average velocity to the change in field using multivalley description as compared to a single-valley description (Fig. 3) can also be seen. This is due to the slower carrier density response [see Fig. 4(a)] to the time-varying field as discussed for the step-up change. The evolution of carrier density, mean energy, and average velocity in each valley using the macrokinetic model and the MC method is shown in Fig. 4. Again, excellent agreement is obtained between these two descriptions.

For each step field, MC simulations (50 000 electrons have been used) require more than 4 h of computation time in the Micro-Vax II. However, solving the moment equations for the single-valley description and for the multivalley description takes about 1.7 and 7.0 s, respectively, in the same computer.

V. CONCLUDING REMARKS

A theory of nonequilibrium transport of carriers in multivalley semiconductors has been presented. It is based on the macrokinetic model¹⁴ for the distribution function in each valley. It is shown that in the case of nonequilibrium and strong intervalley scatterings the transfer effect of carriers between valleys is not properly taken into account when using a single-valley description. The carriers are observed to respond faster to changes in the applied field when using a single-valley "equivalent" model as compared to a multivalley model. That is, the single-valley model by not properly accounting for the dynamics of intervalley energy and the momentum exchanges drives the carrier to equilibrium faster than the multivalley model. Moreover, since the scales at which the relaxation occurs is that of the moment equations, the MKD can correctly yield the macroscopic scattering rates. This can be seen from the excellent agreement between the results from multivalley moment model and the MC results.

ACKNOWLEDGMENT

This work is supported by the Air Force Office of Scientific Research.

APPENDIX

The multivalley semiconductor test model used in this paper has a central valley with mass equal to $0.08m_0$ and two equivalent satellite valleys with mass equal to $0.03m_0$. The energy difference between the lower (central) valley and upper valleys is $\Delta\epsilon_{21} = 0.15$ eV. All valleys have a parabolic band structure. The ϵ - k relation is given by $\epsilon = \hbar^2 k^2 / 2m_i$.

The transition rate for intravalley scattering from state \mathbf{k} , to \mathbf{k}' is given by

$$S_{ii}(\mathbf{k}, \mathbf{k}') = (2\pi/\hbar) |H_{ii}|^2 \delta(\epsilon'_i - \epsilon_i \pm \hbar\omega_i) \quad (\text{A1})$$

and by

$$S_{ij}(\mathbf{k}, \mathbf{k}_j) = (2\pi/\hbar) |H_{ij}|^2 \delta(\epsilon_j - \epsilon_i \pm \hbar\omega_{ij} - \Delta\epsilon_{ij}) \quad (\text{A2})$$

for intervalley scattering from state \mathbf{k}_i to \mathbf{k}_j , where $ij = 1, 2, i \neq j$, $\Delta\epsilon_{12} = -\Delta\epsilon_{21}$, and H_{ij} (or H_{ji}) is the matrix element between the initial and the final states. Thus, transition rate per state in Sec. II is given by

$$P_{ii}(\mathbf{k}_i, \mathbf{k}'_i) = (V/2\pi) S_{ii}(\mathbf{k}_i, \mathbf{k}'_i),$$

$$P_{ij}(\mathbf{k}_i, \mathbf{k}_j) = (V/2\pi) S_{ij}(\mathbf{k}_i, \mathbf{k}_j),$$

where V is the crystal volume. The scattering mechanism in each valley is given as follows:

(i) Intravalley scattering: The intravalley phonon energy in each valley is taken to be equal, and $\hbar\omega_1 = \hbar\omega_2 = 0.035$ eV. The matrix element, H_{ii} , is assumed to be constant for either the emission process or the absorption process. Therefore, Eq. (1) can be rewritten as

$$S_{ii}(\mathbf{k}_i, \mathbf{k}'_i) = \frac{2\pi}{\hbar} B_i \left\{ \begin{array}{l} N_i \delta(\epsilon'_i - \epsilon_i - \hbar\omega_i) \\ (N_i + 1) \delta(\epsilon'_i - \epsilon_i + \hbar\omega_i) \end{array} \right\}, \quad (\text{A3})$$

where B_i is a constant and N_i is the phonon distribution. In this model, N_i is assumed to be in equilibrium and given by

$$N_i = \frac{1}{\exp(\hbar\omega_i/k_B T) - 1},$$

where $k_B T$ is the thermal energy. In Eq. (A3) N_i and $N_i + 1$ correspond to the processes of phonon absorption and emission, respectively. The total scattering rate out of the state \mathbf{k}_i for this process is, therefore, given by

$$\frac{1}{\tau_{ii}(\mathbf{k}_i)} = \frac{V}{(2\pi)^3} \int S_{ii}(\mathbf{k}_i, \mathbf{k}'_i) d\mathbf{k}'_i.$$

For a parabolic valley, the total scattering is found to be

$$\frac{1}{\tau_{ii}(\mathbf{k}_i)} = D_i \sqrt{\epsilon'_i} \left\{ \begin{array}{l} N_i \\ N_i + 1 \end{array} \right\}, \quad (\text{A4})$$

where

$$D_i = \frac{\sqrt{2} m_i^{3/2} V B_i}{\pi \hbar^4},$$

$$\epsilon'_i = \epsilon_i \pm \hbar\omega_i.$$

In this test model, $D_1 = 2.5 \times 10^{13} \text{ s}^{-1} \text{ eV}^{-1/2}$ and $D_2 = 5.0 \times 10^{13} \text{ s}^{-1} \text{ eV}^{-1/2}$.

(ii) Intervalley scattering: Intervalley phonon energy is taken to be $\hbar\omega_{12} = \hbar\omega_{21} = 0.035$ eV. Similarly, H_{ij} is taken to be constant. Equation (A2) is rewritten as

$$S_{ij}(\mathbf{k}_i, \mathbf{k}_j)$$

$$= \frac{2\pi}{\hbar} B_{ij} \left\{ \begin{array}{l} N_{ij} \delta(\epsilon_j - \epsilon_i - \hbar\omega_{ij} - \Delta\epsilon_{ij}) \\ (N_{ij} + 1) \delta(\epsilon_j - \epsilon_i + \hbar\omega_{ij} - \Delta\epsilon_{ij}) \end{array} \right\}, \quad (\text{A5})$$

where B_{ij} is constant, N_{ij} is the intervalley phonon distribution which is in equilibrium and given by

$$N_{ij} = \frac{1}{\exp(\hbar\omega_{ij}/k_B T) - 1}.$$

In Eq. (A5) N_{ij} and $N_{ij} + 1$ correspond to the processes of phonon absorption and emission, respectively. Similarly, the total scattering rate out of \mathbf{k}_i for this process is written as

$$\frac{1}{\tau_{ij}(\mathbf{k}_i)} = \frac{V}{(2\pi)^3} \int S_{ij}(\mathbf{k}_i, \mathbf{k}_j) d\mathbf{k}_j.$$

For our model, it can be rewritten as

IV. A Transport Model for Carriers in Small Spatial/Temporal Scale Compound Semiconductor Devices

I. Introduction

Device modeling requires a proper transport model to describe the carrier transport phenomena that characterize device performances, such as the upper frequency limit and power efficiency. The choices of transport models, in general, depend on space/time scales of interest. For example, the conventional model for device analysis is based on the drift-diffusion model which assumes a quasi-equilibrium distribution of carriers and thus can not account for non-equilibrium behavior due to rapidly space/time-varying fields, such as overshoot [1-5] and undershoot [6] phenomena. This model is, therefore, inadequate when frequencies approach several 10 GHz and/or devices are scaled down to submicrometer size. In such small-scale devices, a transport model including pertinent physics of non-equilibrium phenomena is thus desirable. Most of transport models that have been used [7-13] to account for non-equilibrium phenomena of carriers in compound semiconductor devices is based on the single-valley conservation equations. It has been assumed that the energy and momentum relaxation times in the conservation equations only depend on the carrier mean energy (theoretically, on all moments of the carrier distribution function [14,15]) and are described by the phenomenological equations [7,8]. In compound semiconductor devices, carrier behavior is described by the distribution function in each valley. These distributions in different valleys obey the Boltzmann transport equations (BTE's) that are coupled by inter-valley scattering processes. Consequently, the macroscopic description is given by a set of multi-valley conservation equations which are thus coupled by carrier inter-valley transitions. However, the relaxation times in the multi-valley conservation equations can not be determined from the phenomenological equations [7,8]. The difficulty in determining these times has led to the fact that the use of the conservation equations for carrier dynamics in compound semiconductor devices has assumed [1,2,7-13] only a single valley where the

carrier density, mean energy and average momentum are averaged over all valleys.

Inter-valley transfer has significant influences on non-equilibrium carrier dynamics in compound semiconductor devices. It has been previously found [14-16] that the use of the single-valley conservation equations for the carrier dynamics in GaAs results in faster response to a rapid change in electrical field than actually occurs. This behavior is caused by the slow averaged inter-valley transitions [16] that are not properly taken into account in the single-valley conservation equations. In situations where inter-valley scattering is dominant, the multi-valley conservation equations are therefore necessary. In order to determine the relaxation times for solving the multi-valley conservation equations and to account for inter-valley transfer effects, the assumption has been made in most papers [17-23] that the distribution function in each valley is a displaced Maxwellian. These distributions are then used to evaluate the relaxation times. However, it is well-known that in hot electron situations the electron distribution function appreciably differs from a displaced Maxwellian in compound semiconductors [24,25].

In this paper, a non-equilibrium transport model for compound semiconductor devices has been developed based on the concept of the Macro-Kinetic Distribution (MKD) functions [14-16] (whose time scales are characterized by moments of the distribution). The model provides an efficient scheme for device modeling, and can account for the transfer effects without *a priori* assumption of a displaced Maxwellian distribution. The mathematical formulation of this multi-valley transport model is given in the next section. The resulting model is applied to electron transport in three-valley GaAs with non-parabolic bandstructure subjected to rapidly time-varying fields. The results compared to those obtained from a Monte Carlo method [25] are presented in Sec.III. Conclusions are given in Sec.IV.

II. The Multi-Valley Transport Model

The exact description of carrier transport in compound semiconductors subjected to space/time-varying fields in semi-classical regime is given by the BTE's that are coupled by inter-valley scattering processes and written as

$$\frac{\partial f_i}{\partial t} + \mathbf{v}_i \cdot \nabla f_i + \frac{q\mathbf{E}}{h} \cdot \nabla_{\mathbf{k}} f_i = \left(\frac{\partial f_i}{\partial t} \right)_{\text{intra}} + \sum_{j=1, j \neq i}^{N_v} \left(\frac{\partial f_i}{\partial t} \right)_{j, \text{inter}} + \sum_{j=1, j \neq i}^{N_v} \left(\frac{\partial f_j}{\partial t} \right)_{i, \text{inter}}, \quad (1)$$

where $f_i(\mathbf{r}, \mathbf{k}_i, t)$ is the i th-valley distribution in phase space, N_v is the number of valleys, \mathbf{v}_i is the carrier velocity, \mathbf{k}_i is the wave vector, \mathbf{E} is the electric field, and h is the Planck constant divided by 2π . The first term of the RHS represents the intra-valley scattering, and the inter-valley scattering processes out of and into the i th valley are described by the second and third terms of the RHS, respectively. The carrier density, energy and momentum conservation equations in each valley can be obtained from Eq. (1) by averaging over the distribution, and are given by

$$\frac{\partial n_i}{\partial t} + \nabla \cdot (n_i \mathbf{u}_i) = \sum_{j=1, j \neq i}^N n_j \mathbf{v}_{j\bar{i}} - \sum_{j=1, j \neq i}^N n_i \mathbf{v}_{ij}, \quad (2)$$

$$\frac{\partial(n_i \bar{p}_i)}{\partial t} + \nabla(n_i \bar{p}_i \cdot u_i) = q E n_i - \nabla(n_i k_B T_{ei}) - \frac{n_i \bar{p}_i}{\tau_{mii}} - \sum_{j=1, j \neq i}^N \frac{n_i \bar{p}_i}{\tau_{mij}}, \quad (3)$$

$$\begin{aligned} & \nabla(n_i \bar{e}_i) + \nabla \cdot [n_i u_i (\bar{e}_i + k_B T_{ei})] \\ &= q E \cdot n_i u_i - \frac{n_i (\bar{e}_i - e_o)}{\tau_{eii}} + \sum_{j=1, j \neq i}^N \frac{n_j \bar{e}_j}{\tau_{eji}} - \sum_{j=1, j \neq i}^N \frac{n_i \bar{e}_i}{\tau_{eij}}, \end{aligned} \quad (4)$$

where k_B is the Boltzmann constant, and T_{ei} is the electron temperature related to carrier mean energy \bar{e}_i by

$$\bar{e}_i = \frac{1}{2} m_i^* u_i^2 + \frac{3}{2} k_B T_{ei},$$

m_i^* is the macroscopic effective mass of carriers, and n_i , \bar{p}_i , and u_i are carrier density, average momentum, and average velocity in the i th valley, respectively. The averaged inter-valley carrier transition rates (ν_{ij}) are defined as

$$n_i \nu_{ij} = \int P_{ij}(k_i, k_j) f_i(k_i) dk_i dk_j, \quad (5)$$

where P_{ij} is the transition rate from i th to j th valley. The intra-valley and inter-valley momentum exchange times (τ_{mii} and τ_{mij} , respectively) are defined as

$$-\frac{n_i \bar{p}_i}{\tau_{mii}} = \int P_i P_{ii}(k'_i, k_i) f_i(k'_i) dk_i dk'_i - \int \frac{P_i f_i(k_i)}{\tau_{ii}(k_i)} dk_i, \quad (6a)$$

$$-\frac{n_i \bar{p}_i}{\tau_{mij}} = - \int \frac{P_i f_i(k_i)}{\tau_{ij}(k_i)} dk_i, \quad (6b)$$

and the intra-valley and inter-valley energy exchange times (τ_{eii} , τ_{eji} , and τ_{eij}) are given by

$$\frac{n_i (\bar{e}_i - e_o)}{\tau_{eii}} = \int dk'_i \int dk_i e_i P_{ii}(k'_i, k_i) f_i(k'_i) - \int dk_i \frac{e_i f_i(k_i)}{\tau_{ii}(k_i)}, \quad (7a)$$

$$-\frac{n_i \bar{e}_i}{\tau_{eij}} = - \int dk_i \frac{e_i f_i(k_i)}{\tau_{ij}(k_i)}, \quad (7b)$$

$$\frac{\bar{n}_j \bar{\epsilon}_j}{\tau_{eiji}} = \int d\mathbf{k}_j \frac{(\epsilon_j + \Delta\epsilon_{ji} \mp h\omega_{ji}) f_j(\mathbf{k}_j)}{\tau_{ji}(\mathbf{k}_j)}, \quad (7c)$$

with

$$\frac{1}{\tau_{ij}(\mathbf{k}_i)} = \int P_{ij}(\mathbf{k}_p, \mathbf{k}_j) d\mathbf{k}_j,$$

$$\frac{1}{\tau_{ii}(\mathbf{k}_i)} = \int P_{ii}(\mathbf{k}_p, \mathbf{k}'_i) d\mathbf{k}'_i.$$

The energy separation between *j*th and *i*th valleys is given by $\Delta\epsilon_{ji} = E_{gj} - E_{gi}$, where E_{gj} (E_{gi}) is the energy gap between the *j*th (*i*th) valley and valence band, and $h\omega_{ji}$ is the inter-valley phonon energy.

Unlike the single-valley model, these relaxation times or rates cannot be easily determined from the phenomenological equations [7,8] but require direct evaluation of the integrals in Eqs. (5)-(7). Instead of using the displaced-Maxwellian distribution, an MKD [14-16] can be used to evaluate these integrals and thus the relaxation times or rates. The concept of the MKD has been introduced, in the previous work [14,16], to describe carrier behavior in various time scales. Depending on the device scale, an MKD in each valley corresponding to the scale of interest is chosen to evaluate the relaxation times. The coarseness of the macroscopic description, therefore, depends on the choice of the MKD, f_M . The choice is based on the fact that, generally, $\tau > \tau_\epsilon > \tau_m$ in semiconductors, where τ , τ_ϵ , and τ_m are the carrier density, energy, and momentum relaxation times, respectively. For example, if the scale of interest is in the order of τ_ϵ , the MKD is chosen to be $f_{M\epsilon}(k) = f_{M\epsilon}(k, n, \bar{\epsilon})$ whose time scale is described by τ and τ_ϵ ; thus $f_{M\epsilon}$ contains only information in the scale greater than or as small as τ_ϵ . In this case, the relaxation times evaluated from the integrals of Eqs. (5)-(7) using $f_{M\epsilon}$ depend only on the mean energy; namely, $\tau_\alpha = \tau_\alpha(\bar{\epsilon})$, where τ_α represents τ , τ_ϵ , or τ_m . Similarly, in the scale smaller than τ_ϵ (therefore near τ_m), a higher-resolution MKD can be taken as $f_{Mm}(k) = f_{Mm}(k, n, \bar{\epsilon}, \bar{k})$, and thus $\tau_\alpha = \tau_\alpha(\bar{\epsilon}, \bar{k})$. In this paper, only the energy-time-scale MKD, $f_{M\epsilon}$, is discussed. The momentum-time-scale MKD, f_{Mm} , will be studied in the future.

In the energy time scale, the time scale of the carrier distribution in *i*th valley can be changed [15] in this form:

$$f_i(\mathbf{k}, r, t) = f_{M\epsilon i}[\mathbf{k}_p, n_i(r, t), \bar{\epsilon}_i(r, t)] \quad (8)$$

That is, in the energy time scale, the space-time dependence of f_i is taken to result from changes in n_i , and $\bar{\epsilon}_i$. Using Eq. (8) in the BTE, given in Eq. (1), to change the scale of evolution of the distribution function, it leads to a "macro-kinetic" equation for the MKD in the scale of τ_ϵ . The equation for the energy-time-scale MKD has been found to be, for field along *z* direction

$$qE_{eqi} \frac{\partial f_{Mei}}{\partial k_{zi}} = \left(\frac{\partial f_{Mei}}{\partial t} \right)_c \quad (9a)$$

where

$$qE_{eqi} = \frac{\bar{e}_i(t) - e_0}{u_{si} \tau_{ei}} \quad (9b)$$

with

$$n_i u_{si} = \int f_{Mei}(k_p, n_p, \bar{e}_p) v_i dk_i. \quad (9c)$$

Eq. (9a) represents a distribution function that obeys a steady-state BTE with a time-varying "equivalent" field of the *i*th valley, E_{eqi} , as the driving field, and E_{eqi} is given by Eq. (9b) as a function of \bar{e}_i . This MKD thus responds instantaneously to E_{eqi} , and the information in the time scale smaller than τ_{ei} is filtered. f_{Mei} can be obtained from Eq. (9a), and the relaxation times or rates in each valley can be evaluated from the integrals given in Eqs. (5)-(7) using f_{Mei} in terms of E_{eqi} or \bar{e}_i . These rates or times are, therefore, tabulated for solving the multi-valley conservation equations given in Eqs. (2)-(4).

III. The Applications of the Developed Transport Model

The developed non-equilibrium multi-valley transport model has been applied to electron transport in n-type three-valley GaAs subjected to step fields. In this three-valley GaAs, a homogeneous electron density is assumed. Results obtained from the multi-valley and single-valley conservation equations based on f_{Mei} are compared to those from the three-valley Monte Carlo simulation.

In GaAs, at fields below 2.0 kV/cm, the electron population in the upper (*L* and *X*) valleys is negligible, and thus the single-valley conservation equations can properly describe the electron transport behavior. The excellent agreement between average electron velocities obtained from the single-valley conservation equations and Monte Carlo method is illustrated in Fig. 1 where a step field (from 0.2 to 2.0 kV/cm) is applied to the n-type GaAs at 300 K. However, when applied field increases, the upper-valley population becomes significant and inter-valley scattering dominates the scattering processes. In this case, the single-valley description provides insufficient information on electron transfer between valleys and a multi-valley description is necessary. The deviation between average electron velocities as a consequence of a step change in field from 40 to 5 kV/cm in GaAs determined by the single-valley description and Monte Carlo method is clearly shown in Fig. 2(a) where the multi-valley results based on the developed transport model are also included. Similar to the results in the previous work [16], the single-valley results respond to the rapid change in field faster than the Monte Carlo results. The velocity described by the multi-valley conservation equations is in good agreement with that from Monte Carlo calculations;

however, the difference is still observable. The difference of the average velocities between the multi-valley conservation equations and Monte Carlo calculations in Fig. 2(a) actually results from the deviation of average velocities of electrons in Γ valleys as illustrated in Fig. 2(b). However, these two approaches provide nearly the same evolution of the L -valley velocity shown in Fig. 2(c).

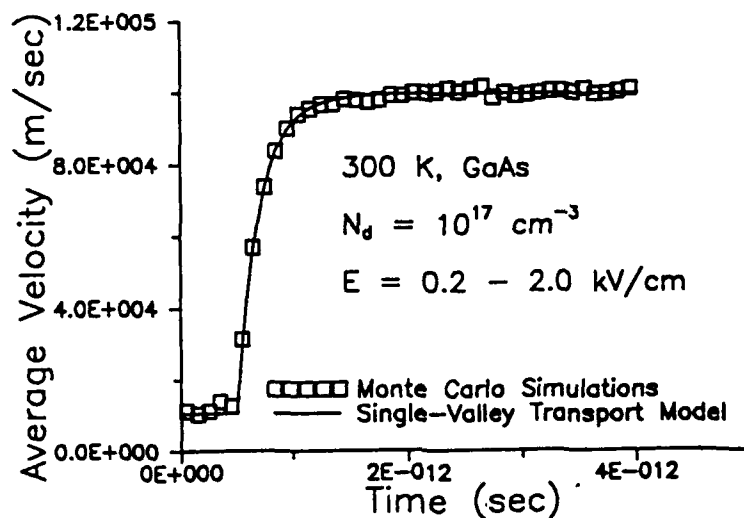


Fig. 1 Evolution of average velocity of electrons in n-type GaAs subjected to a step change in field.

The difference of the Γ -valley velocities shown in Fig. 2(b) determined from these two approaches mainly results from the oversimplified description for the macroscopic effective mass, m^* , used for solving the multi-valley conservation equations. That is, m^* is assumed to be a function of electron mean energy and the energy dependence of m^* is determined by the steady state relation between average momentum and velocity; i.e., $m^* = m^*(\bar{\epsilon}) = \bar{p}_{ss}(\bar{\epsilon})/u_{ss}(\bar{\epsilon})$, where $\bar{\epsilon}$ is the instantaneous mean energy of electrons. Although this description for m^* has been widely used [8-13] in device analysis, it has been found in the present calculations that the velocity dependence of m^* might be significant. Fig. 2(d) shows the evolution of m_{Γ}^* obtained from the Monte Carlo method compared to that of the energy-dependent effective mass. It is noted that electrons in Γ valley described by $m_{\Gamma}^*(\bar{\epsilon})$ is lighter [see Fig. 2(d)] during the interval of velocity undershoot [see Fig. 2(b)]. The smaller $m_{\Gamma}^*(\bar{\epsilon})$ is, therefore, responsible for the larger velocity [see Fig. 2(b)] obtained from the multi-valley transport model, which assumes $m^* = m^*(\bar{\epsilon})$, during the undershoot interval. However, the velocity undershoot shown in Fig. 2(c) is not pronounced in L valley, and therefore $m_L^*(\bar{\epsilon})$ shown in Fig. 2(e) provides an excellent description. As a consequence, the L -valley velocities determined by the multi-valley transport model and Monte Carlo method are in excellent agreement.

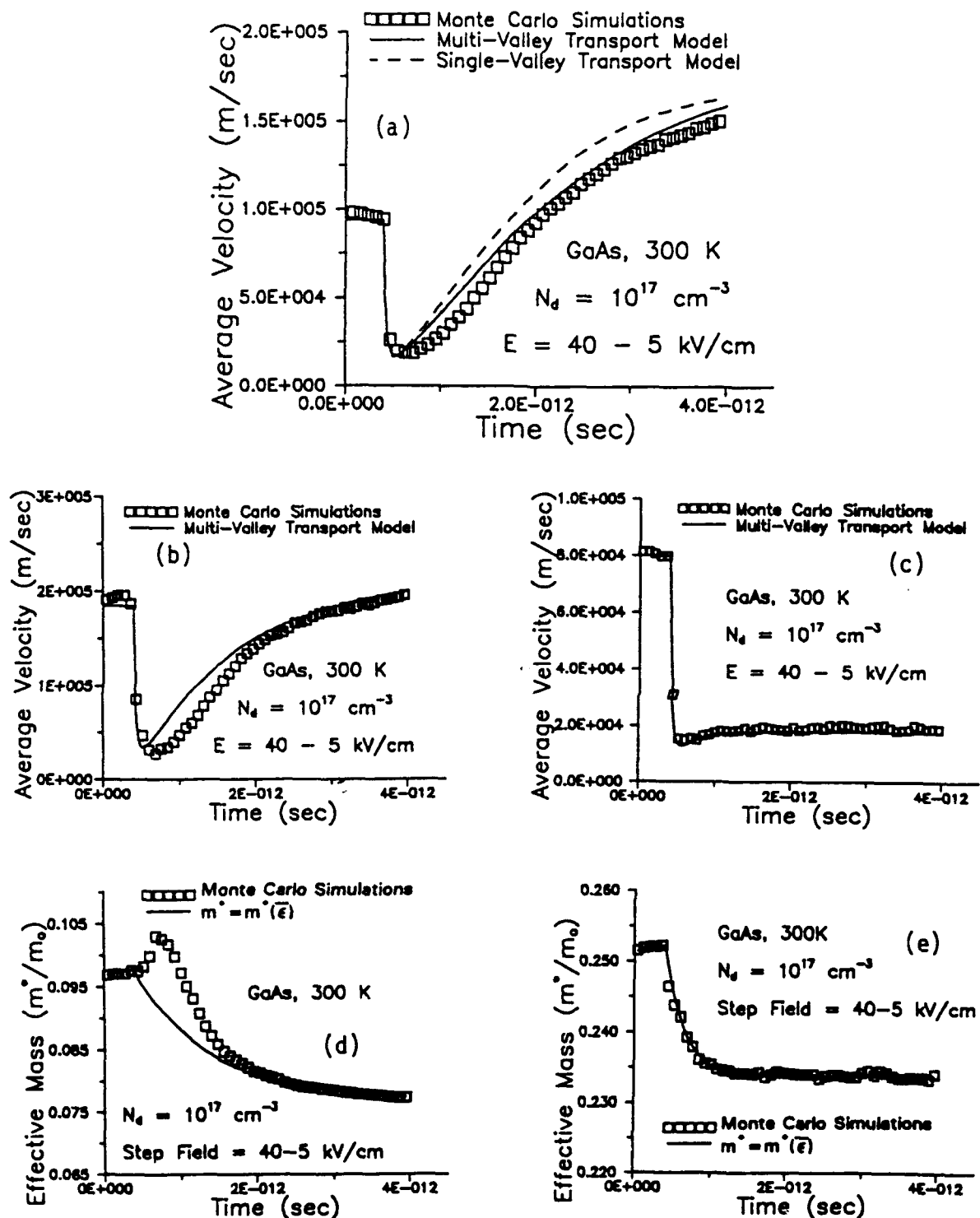


Fig. 2 Evolution of average velocity and macroscopic effective mass of electrons. (a) Total average velocity, (b) Γ -valley velocity, (c) L -valley velocity, (d) Γ -valley effective mass, and (e) L -valley effective mass.

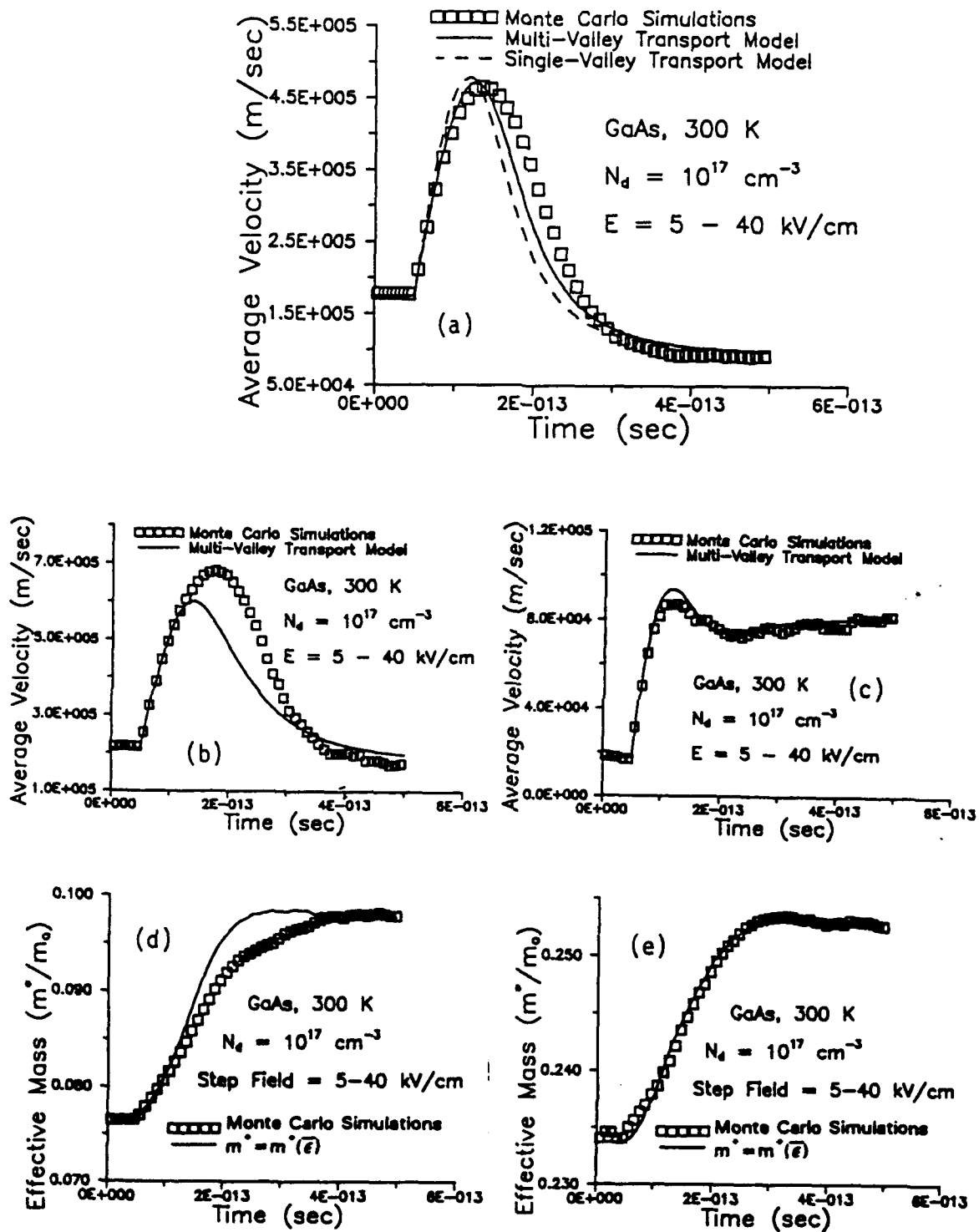


Fig. 3 Evolution of average velocity and macroscopic effective mass of electrons. (a) Total average velocity, (b) Γ -valley velocity, (c) L -valley velocity, (d) Γ -valley effective mass, and (e) L -valley effective mass.

Similar behavior has also been observed during the overshoot interval. The average electron velocity in the n-type GaAs under the influence of a step change in field from 5 to 40 kV/cm is illustrated in Fig. 3(a) where three different approaches are included for comparison. Again, the average velocity described by the single-valley approximation reaches steady state faster than the multi-valley description. The difference between the average velocities in Fig. 3(a) obtained from the multi-valley conservation equations and Monte Carlo calculations results from the relatively low overshoot velocity in Γ valley described by the conservation equations (compared to the Monte Carlo results), as shown in Fig. 3(b). The deviation of Γ -valley velocities between these two approaches is, again, the consequence of the oversimplified dependence of $m_{\Gamma}^*(\bar{\epsilon})$ used in the conservation equations. During the overshoot interval, larger energy-dependent effective mass, $m_{\Gamma}^*(\bar{\epsilon})$, [see Fig. 3(d)] is used in conservation equations, and thus results in smaller overshoot velocity in Fig. 3(b). However, $m_L^*(\bar{\epsilon})$ is almost the same as the effective mass obtained from the Monte Carlo calculations, as shown in Fig. 3(e), since the velocity overshoot in L valley is not pronounced [see Fig. 3(c)]. This leads to good agreement of the L -valley velocities obtained from these two approaches.

IV. Conclusions

A non-equilibrium multi-valley transport model has been developed and used to study the electron transport phenomena in three-valley GaAs. The results show that the single-valley transport model provides an excellent description for electron transport in GaAs at fields below 2.0 kV/cm because inter-valley scattering is negligible. At high fields where inter-valley scattering is significant, a model including information on carrier transfer between valleys is desirable. The developed transport model can provide inter-valley transfer effects, as can be seen from the excellent results presented in Figs. 2(c) and 3(c). The results illustrated in Figs. 2 and 3 have suggested that the macroscopic effective mass might be strongly dependent on the average velocity when velocity overshoot or undershoot behavior is pronounced. The proper description for the macroscopic effective mass will be studied in the future.

Acknowledgement - This work was supported by the Air Force Office of Scientific Research.

References

- [1] J. G. Ruch, "Electron Dynamics in Short-channel Field Effect Transistors," *IEEE Trans. Electron Dev.*, Vol. ED-19, p. 652, 1972.
- [2] T. J. Maloney and J. Frey, "Transient and Steady-state Electron Transport in GaAs and InP," *J. Appl. Phys.*, Vol. 48, p. 781, 1977.
- [3] A. Ghis, E. Constant, and B. Boittiaux, "Ballistic and Overshoot Electron Transport in Bulk Semiconductors and in submicronic devices," *J. Appl. Phys.*, Vol. 54, p. 214, 1983.
- [4] R. B. Hammon, "Electron-velocity Overshoot Observed in Impulse-excited GaAs Photoconductor," *Physica B*, Vol. 134, p. 475, 1985.

- [5] K. Meyer, M. Pessot, G. Mourou, "Subpicosecond Photoconductivity Overshoot in GaAs Observed by Electro-optic Sampling," *Appl. Phys. Lett.*, Vol. 53, p. 2254, 1988.
- [6] E. Constant, "Non-Steady-State Carrier Transport in Semiconductors in Perspective," in *Hot-Electron Transport in Semiconductors*, Edited by L. Reggiani, Berlin Heidelberg, Springer-Verlag, 1985, p.227.
- [7] R. S. Huang and P. H. Sadbrooke, "The Physics of Excess Electron Velocity in Submicron Channel FET's," *J. Appl. Phys.*, Vol. 48, p. 4791, 1977.
- [8] M. Shur, "Influence of Nonuniform Field Distribution on Frequency Limits of GaAs Field-Effect Transition," *Elect. Lett.*, Vol. 12, p. 615, 1976.
- [9] P. A. Rolland, G. Salmer, E.Constant, and R.Fauquemebergues, "Comparative Frequency Behavior of GaAs, InP, and GaInAs Transferred Electron Devices-Derivation of a Simple Comparative Criterion," *IEEE Trans. Elect. Dev.*, Vol. ED-28, p. 341, 1981.
- [10] W. R. Curtice and Y. H. Yun, "A Temperature Model for the GaAs MESFET," *IEEE Trans. Elect. Dev.*, Vol. ED-28, p. 954, 1981.
- [11] B. Carnez, A. Cppy, A. Kaszynski, E. Constant, and G. Salmer, "modeling of a Submicrometer Gate Field-effect Transistor Including Effects of Non-stationary Electron Dynamics," *J. Appl. Phys.*, Vol. 15, p. 784, 1980.
- [12] C. M. Snowden and D. Loret, "Two-dimension Hot Electron Model For Short Gate Length GaAs MESFETs," *IEEE Trans. Elect. Dev.*, Vol. ED-34, p. 212 1987.
- [13] N. Goldsman, J. Frey, "Efficient and Accurate Use of the Energy Transport Method in Device Simulation," *IEEE Trans. Elect. Dev.*, Vol. ED-35, p. 1524, 1988.
- [14] Ming-Cheng Cheng, "Non-Equilibrium Transport of Carriers in Multi-Valley Semiconductors," *Ph.D. Dissertation*, Polytechnic University, 1990.
- [15] E. E. Kunhardt, M. Cheng, and J. Wu, "Non-equilibrium Macroscopic Models of Carrier Dynamics in a Semiconductor," *J. Appl. Phys.*, Vol. 64, p. 1220, 1988.
- [16] M. Cheng and E. E. Kunhardt, "A Theory of Non-equilibrium Carrier Transport in Multi-valley Semiconductors," *J. Appl. Phys.*, Vol. 67, p. 1907, 1990.
- [17] T. Toyabe and H. Kodera, "A Theory for Inter-valley Transport Effect in Two-valley Semiconductors," *Jpn. J. Appl. Phys.*, Vol. 13, p. 1404, 1974.
- [18] P. N. Butcher and W. Fawcett, *Proc. Phys. Soc.*, Vol. 86, p. 1205, 1965.
- [19] K. Blotekjaer, "Transport Equations for Electrons in Two-valley Semiconductors," *IEEE Electron Dev.*, Vol. ED-17, p. 38, 1970.
- [20] D. Jones and H. D. Rees, "Accumulation Transit Mode in Transferred-electron Oscillators," *Elect. Lett.*, Vol. 8, p. 566, 1972; "Electron-relaxation effects in transferred-electron devices revealed by a new simulation method," *Electron Lett.*, Vol. 8, p. 363, 1972; "Overlength modes of transferred electron oscillators," *Elect. Lett.*, Vol. 9, p. 105, 1973.
- [21] D. Jones and H. D. Rees, "A reappraisal of instabilities due to the transfer electron effects," *J. Phys. C.: Solid State Phys.*, Vol. 6, p. 1781, 1973.
- [22] R. Bosch and H. N. Thim, "Computer Simulations of Transferred Electron Devices using the Displaced Maxwellian Approach," *IEEE Trans. Elect. Dev.*, Vol. ED-21, p. 16, 1974.

- [23] E. Rosencher, "Ballistic Transport in Semiconductors: A Displaced Maxwellian Approach," *J. Phys.*, Vol. 42, p. C7-351. 1981.
- [24] K. Hess, "Phenomenological Physics of Hot Carriers in Semiconductors", in *Physics of Nonlinear Transport in Semiconductors*, edited by K. Ferry, J. R. Barker, and C. Jacoboni, New York, Plenum Press, p. 1, 1988.
- [25] M. Cheng, and E. E. Kunhardt, "Electron Energy Distribution, Transport Parameters, and Rate Coefficients in GaAs," *J. Appl. Phys.*, Vol. 63, p. 2322, 1988.

V. Monte Carlo Investigation of Acoustic Intervalley and Intravalley Deformation Potentials for GaAs

1. Introduction

The study of charge transport in semiconductors and devices requires a number of material parameters, such as the effective mass, acoustic deformation potential, various phonon energies, energy separations between valleys, and intervalley and intravalley deformation potentials, etc. These parameters are necessary for determination of the carrier mobility, diffusion coefficients, energy and momentum relaxation times, and thermal conductivity. However, there are large uncertainties in the experimental and theoretical values of some of these parameters. In GaAs, considerably different values for the acoustic deformation potential¹⁻¹⁰ in the Γ valley (D_{Γ}), effective mass¹⁰⁻¹³ in the L valley (m_L), energy separations¹²⁻¹⁷ between Γ and L valleys ($\Delta\epsilon_{\Gamma L}$), and L-L intravalley and Γ -L intervalley deformation potentials^{10-12, 18-26} (D_{LL} and $D_{\Gamma L}$, respectively) have been suggested in the past decade. For example, a value of 7.0 eV for D_{Γ} of GaAs^{11, 12, 27, 32} has been used for studies of electron transport in GaAs, or heterostructure GaAs-GaAlAs. Although this value, together with some adjustable (uncertain) material parameters, has given reasonable theoretical steady-state results^{11, 12, 32} compared to the experimental data,^{33, 34} recent experimental^{1, 4} and theoretical^{7, 9} results have suggested a larger value for D_{Γ} .

The experiment¹ of free electron absorption of Se-doped GaAs has given a value of 15.7 eV for D_{Γ} . The analysis² of temperature dependence of mobility in n-type GaAs has led to $D_{\Gamma}=16.0\pm 0.5$ eV. Recently, it has been found³⁵ that a high-mobility heterostructure exhibits linear temperature dependence on the inverse mobility of electrons at very low temperature. This indicates that the contribution of acoustic-phonon scattering dominates the temperature dependence of mobility at very low temperature. The analysis³⁻⁵ of this phenomena has yielded a value of 13.0–14.0 eV for D_{Γ} , in agreement with the 13.5 eV suggested by Price.^{33, 34} However, a relatively

small value of $D_{\Gamma}=9.3$ eV has been obtained from the measurement⁶ of the band-edge deformation potential in GaAs. More recently, theoretical calculations have also arrived at similar values: 8, 9.3, and 9.6 eV for D_{Γ} .⁷⁻⁹ The various calculated or measured values for D_{Γ} may be due to the incomplete model and/or experimental errors. Moreover, the choices of the values for the other material parameters of GaAs in Γ valley (such as m_{Γ} and the optical-phonon energy $\hbar\omega_p$) used in the calculations may also give rise to the deviation in the value of D_{Γ} .

However, these results suggested a value for D_{Γ} somewhat between 9.0 and 16.0 eV, instead of 7.0 eV that is usually used.^{11, 12, 27-32} Moreover, the change of the value of D_{Γ} from 7.0 eV will also necessitate the modification of some other material parameters (including $D_{\Gamma L}$ and D_{LL}) that were determined¹¹ numerically based on the Monte Carlo simulations using $D_{\Gamma}=7.0$ eV. In this paper, Monte Carlo simulations,³² using nonparabolic bandstructure, for electron transport in GaAs at 300 K have been carried out to investigate the effect of the acoustic deformation potential D_{Γ} on the low-field mobility of electrons, and thus to arrive at a reasonable value of D_{Γ} . The dependence of the mobility and velocity-field relation on the material parameters including D_{Γ} , $\hbar\omega_p$, m_{Γ} , m_L , $D_{\Gamma L}$, D_{LL} , and $\Delta\epsilon_{\Gamma L}$, is discussed for fields less than 15.0 kV/cm. The influence of D_{Γ} , $D_{\Gamma L}$, and D_{LL} on the peak velocity, threshold field for Gunn effect, and negative differential mobility is also presented. Although the material parameters used in Monte Carlo simulations are taken to be constant, it should be pointed out that all parameters can actually vary with energy.

2. Low-Field Mobility

At very low field, polar optical-phonon scattering dominates the scattering processes in GaAs at room temperature. However, the low-field mobility of electrons, μ , also strongly depends on acoustic-phonon scattering since it is a nearly isotropic scattering in contrast to the forward scattering of polar optical phonons. The value of μ is, therefore, strongly dependent on D_{Γ} . In addition to D_{Γ} , our calculation also show that μ exhibits high sensitivity to

the value of optical-phonon energy $\hbar\omega_p$. This is because its value is comparable to thermal energy at room temperature, and thus an increase in the value of $\hbar\omega_p$ used in Monte Carlo calculations at low fields (where energy mean energy is close to the thermal energy) will considerably reduce the number of electrons suffering the optical-phonon emission. Moreover, near the thermal energy, the optical-phonon scattering rate slightly decreases with the value of $\hbar\omega_p$. Consequently, the increase in $\hbar\omega_p$ can raise the value of μ . The dependence of low-field mobility on optical phonon energy is shown in Fig.1 for different values of D_{ac} . Fig.1 also illustrates the strong dependence of low-field mobility on the effective mass m_r . Results of μ shown in Fig.1 using $D_{ac}=9.3$ eV and $m_r=0.063m_0$ are close to those using $D_{ac}=13.5$ eV and $m_r=0.059m_0$. The value of D_{ac} can be, therefore, estimated from Fig.1 using the reliable experimental results for effective mass m_r , optical-phonon energy $\hbar\omega_p$, and low-field mobility μ :

The experiments³⁷⁻⁴⁰ of Hall effect measurements lead to a value of electron Hall mobility, μ_H , slightly greater than 8600 $\text{cm}^2/\text{v-s}$ for pure GaAs at room temperature, where $\mu_H = r_H \mu$ (based on the van der Pauw method⁴¹), and r_H is the Hall factor which depends on magnetic field. The value of r_H was measured^{42,43} to be approximately 1.1 at the magnetic field used in the measurements.³⁷⁻⁴⁰ The low-field mobility of electrons in GaAs at room temperature is, therefore, calculated to be approximately 7900 $\text{cm}^2/\text{v-s}$. This value is in good agreement with the theoretical values:^{44,45} 7900 and 8000 $\text{cm}^2/\text{v-s}$. According to the analysis⁴⁶ of the infrared reflection spectra of GaAlAs mixed crystal using Kramers-Kronig technique, $\hbar\omega_p$ is found to be equal to 36.2 meV which is suggested by many authors^{2,12,30} and also close to the value 36.0 or 36.1 meV used in recent papers.^{1,22,40,45,47} Besides, the experimental measurements⁴⁸ have led to $m_r/m_0 = 0.064 \pm 0.002$ for GaAs at room temperature, which is in good agreement with the values used in some papers¹¹⁻¹³: 0.063 and 0.0638 .

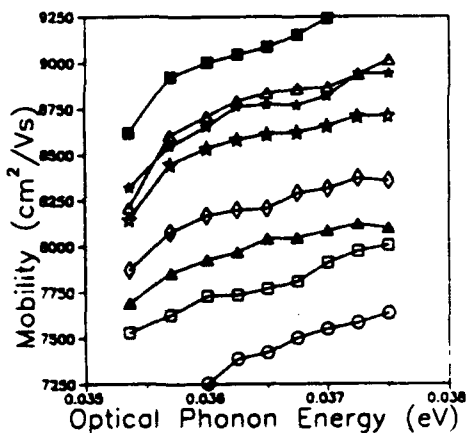


Fig. 1. Low-field mobility of electrons in GaAs as a function of optical-phonon energy for different values of D_{ac} and m_r . The effect mass m_r is taken to be $0.063m_0$ for all results except for those represented by + where $m_r=0.059m_0$. Symbols: \odot $D_{ac}=16.0$ eV; \square $D_{ac}=14.0$ eV; \triangle $D_{ac}=13.0$ eV; \diamond $D_{ac}=12.0$ eV; \star $D_{ac}=10.0$ eV; \blacktriangle $D_{ac}=9.3$ eV; \blacksquare $D_{ac}=7.0$ eV; \blacklozenge $D_{ac}=13.5$ eV.

If the values of μ , $\hbar\omega_p$, and m_r are chosen to be 8000 $\text{cm}^2/\text{v-s}$, 36.1 meV, and $0.063m_0$, respectively, the acoustic deformation potential D_{ac} of GaAs is to be as large as 12.7 eV according to Fig.1. However, the use of $D_{ac}=16.0$ eV, $\hbar\omega_p=36.1$ meV, and $m_r=0.063m_0$ gives $\mu \sim 7250$ $\text{cm}^2/\text{v-s}$. On the other hand, the mobility as high as 8700 $\text{cm}^2/\text{v-s}$ is obtained when using $D_{ac}=9.3$ eV, $\hbar\omega_p=36.1$ meV, and $m_r=0.063m_0$.

3. Velocity-Field Relation Near and Above the Threshold Field

At fields near the threshold field, the velocity-field relation also, in part, depends on the value of D_{ac} . This dependence is illustrated in Fig.2. The material parameters used in calculations for Fig.2 are from Ref.11 except for D_{ac} . The experimental results^{33,34} are also included for comparison. As shown in Fig.2, in addition to the smaller low-field mobility of electrons μ , the larger D_{ac} also leads to smaller peak velocity, and larger threshold field. As field increases to a value above 15.0 kV/cm, the calculated average velocity is almost independent of the value of D_{ac} because of much stronger intervalley scattering. In Fig.2, the deviation from experimental results at fields around the threshold field is evident when using larger D_{ac} . However, in Fig.2, a smaller value of optical-phonon energy ($\hbar\omega_p=35.36$ meV) than 36.1 meV (as discussed in the previous section) has been used. Based on Fig.1, the use of $\hbar\omega_p=36.1$ meV will raise the low-field mobility, and thus will increase the slope of the velocity-field curve at low field in Fig.2. Also, a relatively large value of Γ -L deformation potential ($D_{\Gamma L}=1.0 \times 10^9$ eV/cm) has been used in Fig.2. Although this value for $D_{\Gamma L}$ has been widely used in many papers,^{11,32,49-52} values for $D_{\Gamma L}$ between 1.5×10^8 and 7.0×10^8 eV/cm have been suggested in recent papers^{16-21,23-26} (see the recent review and theoretical calculations in Refs. 25 and 26). In addition, values for effective mass m_r , and the energy separation between Γ and L valleys $\Delta\epsilon_{\Gamma L}$,

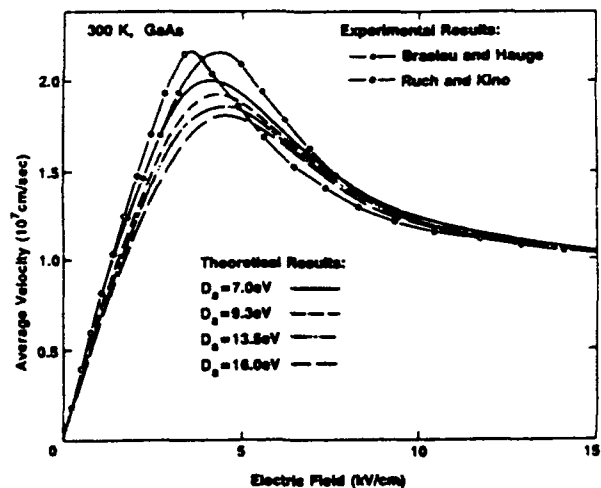


Fig. 2. Average velocity of electrons in GaAs as a function of electric field for different values of D_{ac} varying from 7.0 eV to 16.0 eV. Also included are the experimental results (Refs. 33 and 34).

(0.222 m_0 and 0.33 eV are used, respectively, in Fig. 2) used in many papers are considerably different. The value for m_L has been ranged from 0.18 m_0 to 0.29 m_0 ,^{11,12,20,21} and between 0.28 eV and 0.34 eV for $\Delta\epsilon_{TL}$.^{1,10-14,21,24}

Our calculations indicate that reducing the value of D_{TL} leads to a decrease in the threshold field and peak velocity. This is because electrons are heated up more easily when using smaller D_{TL} . Therefore, energy distribution of electrons in the Γ valley becomes flatter, which increases the number of electrons with energy above $\Delta\epsilon_{TL}$. On the other hand, increasing the value of $\Delta\epsilon_{TL}$ results in increases in the threshold field and peak velocity. The threshold field and peak velocity are not sensitive to the deformation potential, D_{LL} , but vary slightly with m_L . Moreover, the negative slope of the velocity-field curve (ie, the negative differential mobility) at fields between the threshold field and approximately 8.0 kV/cm strongly depends on D_{TL} , and is strongly dependent on D_{LL} and m_L for fields greater than 7.0 kV/cm.

Fig.3 shows that the same threshold field can be achieved by properly varying the values of D_{TL} and D_{sr} . The use of larger D_{sr} (13.5 eV) is to result in a larger threshold field which, however, is compensated by the use of a smaller D_{TL} (4.5×10^8 eV/cm). As a consequence, the velocity-field curve with $D_{TL} = 4.5 \times 10^8$ eV/cm and $D_{sr} = 13.5$ eV exhibits the same threshold as the one with $D_{TL} = 7.0 \times 10^8$ eV/cm and $D_{sr} = 10.0$ eV. Based on the same reasons, the use of $D_{sr} = 7.0$ eV and $D_{TL} = 1.22 \times 10^9$ eV/cm can also provide the same threshold. The peak velocity is smaller when using $D_{sr} = 13.5$ eV due to stronger acoustic-phonon scattering. In addition, the negative slope at fields 4.0 and 8.0 kV/cm is relatively large for the curve using $D_{TL} = 4.5 \times 10^8$ eV/cm. This is because electrons are heated up more easily, as previously mentioned, and more electrons are pumped into upper (low-mobility) valleys; thus the velocity decreases faster with applied field.

Fig.4 illustrates that Monte Carlo simulations using $\Delta\epsilon_{TL} = 0.33$ eV and $D_{TL} = 8 \times 10^8$ eV/cm give the same peak velocity and threshold field as those using $\Delta\epsilon_{TL} = 0.35$ eV

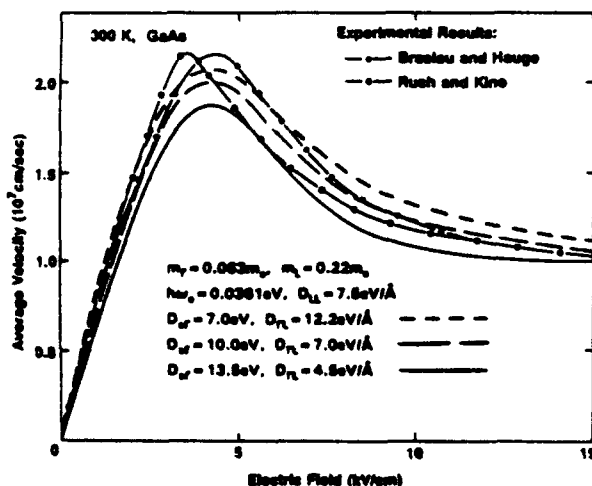


Fig. 3. Average velocity of electrons in GaAs as a function of electric field for different values of D_{sr} and D_{TL} . Also included are the experimental results (Refs. 33 and 34).

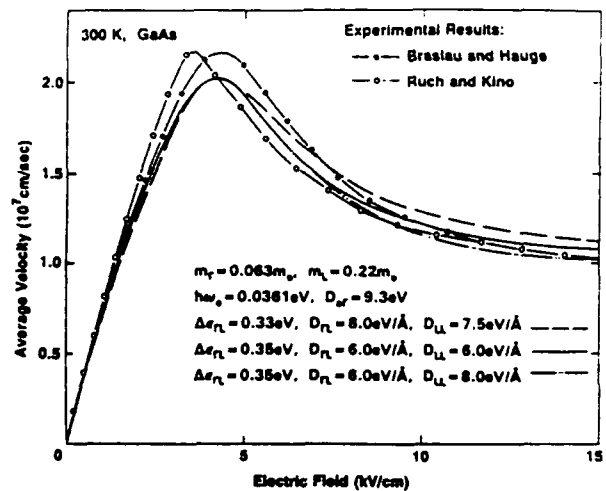


Fig. 4. Average velocity of electrons in GaAs as a function of electric field for different values of $\Delta\epsilon_{TL}$, D_{TL} , and D_{LL} . Also included are the experimental results (Refs. 33 and 34).

and $D_{TL} = 6.0 \times 10^8$ eV/cm. Same values for m_r , m_L , D_{sr} , and $h\omega_s$ are used in the simulations for Fig.4. The use of larger D_{TL} (8.0×10^8 eV/cm) intends to increase both of the peak velocity and the threshold which can be balanced by using a smaller value of $\Delta\epsilon_{TL}$ (0.33 eV). Again, the negative slope at fields between 4.0 and 7.5 kV/cm is larger for the smaller D_{TL} . The dependence of the negative slope on the value of D_{LL} at fields greater than 7.0 kV/cm is also illustrated in Fig.4. The average velocity with the value of $D_{LL} = 8.0 \times 10^8$ eV/cm decreases faster than the one with $D_{LL} = 6.0 \times 10^8$ eV/cm as field increases; both uses the same $\Delta\epsilon_{TL}$ and D_{TL} . This is because the larger D_{LL} causes higher scattering rate in the L valleys.

4. Conclusions

In this paper, the acoustic deformation potential, D_{sr} , has been estimated to be 12.7 eV according to the dependence of the low-field mobility on D_{sr} and $h\omega_s$, as shown in Fig.1. However, the information provided by the available experimental measurements is not sufficient to determine the intervalley and intravalley deformation potentials. As can be seen in Fig.3 and 4, proper adjustments of the uncertain parameters (m_L , $\Delta\epsilon_{TL}$, D_{TL} , and D_{LL}) can provide reasonable Monte Carlo results of the velocity-field curve to fit the experimental results.^{33,34} There is no unique set of the parameters that can generate results in good agreement with experimental measurements of the velocity-field curve. In order to further restrict the set, it is, therefore, desirable to also include the comparison between experimental and theoretical results of the longitudinal diffusion coefficient which strongly depends on the value of m_L , $\Delta\epsilon_{TL}$, D_{TL} and D_{LL} at fields near and above the threshold field. However, the available experimental results^{33,35,36} for the diffusion coefficient are evidently different. For example, the longitudinal diffusion coefficient was suggested to be above 800.0 cm^2/sec at 3.0 kV/cm in Ref.33 and less than 450 cm^2/sec in Refs. 35 and

54. Moreover, as previously mentioned, the experimental and theoretical values for the effective mass m_L , and the energy separation $\Delta\epsilon_{FL}$ that have been used in previous studies, are considerably different. To determine the value for D_{FL} and D_{LL} , more reliable experimental results for longitudinal diffusion coefficient, the energy separation between Γ and L valleys, and the L-valley effective mass are desirable.

In submicron and high-speed semiconductor devices, carrier transport behavior is characterized by energy and momentum relaxation times⁵⁵⁻⁵⁷ which strongly depend on

intervalley and intravalley scattering at fields above the threshold, and thus on the values of D_{FL} and D_{LL} . To develop a transport model for these devices, and to study carrier dynamics in fast transient situations, it is necessary to obtain more accurate values for D_{FL} and D_{LL} .

Acknowledgements - The work presented in this paper was submitted by M. Cheng in partial fulfillment of the requirements for the Ph.D. degree in Electrical Engineering at the Polytechnic University. This work was supported by The Air Force Office of Scientific Research.

References

1. P. Feffer, I. Gorczyca & W. Zawadzki, *Solid State Commun.* **51**, 179 (1984).
2. H. J. Lee, J. Basinski, L. Y. Juvarel & J. C. Woolley, *Can. J. Phys.* **57**, 233 (1979).
3. E. E. Mendez, P. J. Price & M. Heiblum, *Appl. Phys. Lett.* **45**, 294 (1984).
4. B. J. F. Lin, D. C. Tsui & G. Weimann, *Solid State Commun.* **56**, 287 (1985).
5. B. J. F. Lin, D. C. Tsui, *Surf. Sci.* **174**, 397 (1986).
6. D. D. Nolte, W. Walukiewicz & E. E. Haller, *Phys. Rev. Lett.* **59**, 501 (1987).
7. M. Cardona & N. E. Christensen, *Phys. Rev. B* **35**, 6182 (1987).
8. W. Walukiewicz, *Phys. Rev. B* **37**, 8530 (1988).
9. C. Priester, G. Allan & M. Lannoo, *Phys. Rev. B* **37**, 8519 (1988).
10. S. Adachi, *J. Appl. Phys.* **58**, R1 (1985).
11. M. A. Littlejohn, J. R. Hauser and T. H. Glisson, *J. Appl. Phys.* **48**, 4587 (1977).
12. J. Pozela & Reklaitis, *Solid State Commun.* **27**, 1073 (1978).
13. D. E. Aspnes, *Phys. Rev. B* **14**, 5331 (1976).
14. D. E. Aspnes & M. Cardona, *Bull. Am. Phys. Soc.* **23**, 410 (1977).
15. J. R. Chelikowsky & M. Cohn, *Phys. Rev. B* **14**, 556 (1976).
16. O. K. Anderson, *Phys. Rev. B* **12**, 3060 (1975).
17. N. E. Christensen, *Phys. Rev. B* **30**, 5753 (1984).
18. C. L. Collins & P. Y. Yu, *Phys. Rev. B* **30**, 4501 (1984).
19. K. Kash, P. A. Wolf & W. A. Bonner, *Appl. Phys. Lett.* **42**, 173 (1983).
20. S. Krishnamurthy & A. Sher, *Appl. Phys. Lett.* **53**, 1853 (1988).
21. J. Shah, B. Deveaud, T. C. Damen, W. T. Tsang, A. C. Gosard & P. Laugli, *Phys. Rev. Lett.* **59**, 222 (1987).
22. D. N. Mirlin, V. F. Sapega, I. Ya. Karlik & R. Katilius, *Solid State Commun.* **61**, 799 (1987).
23. V. Barelkis, V. Viktoravichyus, A. Gal'dikas & Milyushite, *Sov. Phys. Semicond.* **14**, 847 (1980).
24. Landolt-Bornstein, *Numerical Data and Functional Relationships in Science and Technology*, Vol. 22, edited by O. Madelung, (Springer, Berlin 1987).
25. M. Cardona and S. Zollner, in *Properties of GaAs* (INSPEC data base, 1990)
26. Stefan Zollner, Sudha Gopalan, and Manuel Cardona, *Appl. Phys. Lett.* **54**, 614 (1989); *J. Appl. Phys.* **68**, 1682 (1990).
27. W. Walukiewicz, H. E. Ruda, J. Lagowski & H. C. Gatos, *Phys. Rev. B* **30**, 4571 (1984); *Phys. Rev. B* **32**, 2645 (1985).
28. K. Lee & M. S. Shur, T. J. Drummond & H. Morkoc, *J. Appl. Phys.* **54**, 6432 (1983).
29. B. J. F. Lin, D. C. Tsui, M. A. Paalanen & A. C. Gosard, *Appl. Phys. Lett.* **45**, 695 (1984).
30. D. Y. Xing, M. Liu & C. S. Ting, *Phys. Rev. B* **37**, 10283 (1988).
31. H. Shichijo & K. Hess, *Phys. Rev. B* **23**, 4197 (1989).
32. M. Cheng & E. E. Kunhardt, *J. Appl. Phys.* **63**, 2322 (1988).
33. J. G. Ruch & G. S. Kino, *phys. Rev.* **174**, 921 (1968).
34. N. Braslau & P. S. Hauge, *IEEE Trans. Elect. Devices* ED-17, 616 (1970).
35. P. J. Price, *Surf. Sci.* **143**, 145 (1984).
36. P. J. Price, *Phys. Rev. B* **32**, 2643 (1985).
37. G. E. Stillman, C. M. Wolfe & J. O. Dimmock, *Proc. 3rd Int. Conf. Photocond.* p.269, Pergamon, Oxford (1971).
38. D. E. Bolger, J. Franks, J. Gordon & Whittaker, *Gallium Arsenide*, p.16, Inst. of Phys. Soc., London (1967).
39. G. T. Stillman, C. M. Wolfe & J. O. Dimmock, *Semiconductors and Semimetals Vol. 12*, edited by R. K. Willardson and A. C. Beer, p.169, Academic, New York (1976).
40. D. L. Rode, *Semiconductors and Semimetals Vol. 10*, edited by R. K. Willardson and A. C. Beer, Chap. 1, Academic, New York (1975).
41. L. J. van der Pauw, *Phillips Res. Rep.* **13**, 1 (1958).
42. G. E. Stillman, C. M. Wolfe & J. O. Dimmock, *J. Phys. Chem. Solid*, **31**, 1199 (1970).
43. D. L. Rode, *Phys. Stat. Sol.* **55**, 687 (1973).
44. D. L. Rode & S. Knight, *Phys. Rev. B* **3**, 2534 (1971).
45. W. Walukiewicz, L. Lagowski, L. Jastrzebski, M. Lichtensteiger & H. C. Gatos, *J. Appl. Phys.* **50**, 899 (1979).
46. M. Hegems & G. L. Pearson, *Phys. Rev. B* **1**, 1576 (1970).
47. K. Wan, J. F. Young, R. L. S. Devine & W. T. Moore, *J. Appl. Phys.* **11**, 5598 (1988).
48. See the discussion in Ref.35, p.180.
49. K. Brennan, K. Hess & G. T. Infrate, *IEEE Elect. Dev. Lett.* EDL-4, 332 (1983).
50. K. F. Brenna, D. K. Park, K. Hess, and M. A. Littlejohn, *J. Appl. Phys.* **63**, 5004 (1988).
51. P. I. Rockett, *IEEE Trans. Elect. Devices* ED-35, 849 (1988).

52. H. Schichijo & K. Hess, Phys. Rev. B 23, 4197 (1981).
53. V. Bareikis, V. Viktoravichyus, A. Gal'dikas & Milyushite, Sov. Phys. Semicond. 14, 847 (1980).
54. D. Gasquet, M. de Murcia, J. P. Nougier, C. Gontrand, Physica 134B, 264 (1985).
55. E. E. Kunhardt, M. Cheng, and C. Wu, J. Appl. Phys. 64, 1220 (1988).
56. M. Cheng and E. E. Kunhardt, J. Appl. Phys. 67, 1907 (1990).
57. Ming-Cheng Cheng and E. E. Kunhardt, *Proc. of the Seventh Int. Conf. on Numerical Analysis of Semiconductor Devices and Integrated Circuit*, p.161 (NASECODE VII Conf., Copper Mountain, Colorado, 1991).

APPENDIX A: EXPERIMENTAL FACILITY

AN ELECTRO-OPTIC SAMPLING SYSTEM FOR INVESTIGATION OF TRANSIENT FIELD
DYNAMICS IN HIGH POWER SWITCHES

Andrew Garvie and Mary Eschwei
Polytechnic University
Route 110
Farmingdale NY 11735

November 91

1.0 INTRODUCTION

Electro-optic sampling [Valdmanis et al 1983, Kolner and Bloom, 1986] measures electric field magnitudes with both high spatial and temporal resolution via a medium with electric field dependent refractive indices. These characteristics provide a first opportunity to experimentally investigate short time-scale phenomena, including velocity overshoot [Nuss et al., 1987, Meyer et al. 1988], local field variations in semiconductor materials, and opto-electronic switching not previously observable directly. The technique has been applied to the observation of pulse propagation in GaAs integrated circuits where the GaAs is used as both the circuit substrate and the electro-optic medium [Weisenfeld et al. 1987, Zhang and Jain (1987), Rodwell et al. 1986], and subpicosecond photoconductivity [Iverson et al., 1988, Chamoun et al., 1989]. Space-charge phenomena are key problems to the understanding of interfacial polarization and electret formation, carrier transport across metal-semiconductor, and metal-insulator barriers, transition from electrode limited to bulk limited conduction processes in metal-semiconductor-metal systems, and to the understanding of the self-sustained conduction, known as lock-on [Brinkmann et al 1991], seen in semiconductors at high fields. Non-equilibrium charge carrier transport in semiconductors yields information about carrier-phonon [Kutt et al, 1991] and carrier-carrier interactions and high field phenomena like velocity overshoot, ballistic transport, and resonant tunneling. Previously used techniques have been either electronic or optical but but lack the time resolutions adequate to observe relaxation phenomena on the tens of femtoseconds to picosecond time-scales.

2.0 THEORETICAL AND DESIGN ASPECTS

An apparatus for measurement of the field strengths of short pulses produced by photocarriers in semiconductors requires, for many applications, sensitivity to small fields and high spatial and temporal resolution. These characteristics can be obtained from a combination of the high frequency response of the polarizability of electro-optic materials (such as LiTaO_3 and LiNbO_3), ultra-short pulses of modelocked laser systems and narrow bandpass detection systems. This section describes the principles upon which electro-optic sampling is based and methods available to implement them.

2.1 The Index Ellipsoid and Impermeability Tensor

The electric field at a point in a dielectric is the sum of two fields: D/ϵ_0 associated with free charges and $-P/\epsilon_0$ associated with bound charges, that is,

$$D = \epsilon_0 E + P, \quad (1)$$

where P , the *electric polarization* is the dipole moment per unit volume at a given point and is a macroscopic quantity. In general, P is a tensor and can be expressed as

$$\begin{aligned} P_x &= \epsilon_0 (\chi_{11} E_x + \chi_{12} E_y + \chi_{13} E_z), \\ P_y &= \epsilon_0 (\chi_{21} E_x + \chi_{22} E_y + \chi_{23} E_z), \\ P_z &= \epsilon_0 (\chi_{31} E_x + \chi_{32} E_y + \chi_{33} E_z) \end{aligned} \quad (2)$$

allowing D to be expressed in terms of E :

$$\begin{aligned} D_x &= \epsilon_{11} E_x + \epsilon_{12} E_y + \epsilon_{13} E_z, \\ D_y &= \epsilon_{21} E_x + \epsilon_{22} E_y + \epsilon_{23} E_z, \\ D_z &= \epsilon_{31} E_x + \epsilon_{32} E_y + \epsilon_{33} E_z. \end{aligned} \quad (3)$$

or $D_i = \epsilon_{ij} E_j$ where $\epsilon_{ij} = \epsilon_0 (1 + \chi_{ij})$ and for ϵ a real dielectric tensor $\epsilon_{ij} = \epsilon_{ji}$.

The energy density U_0 in the stored electric field in an anisotropic medium can be written in terms of the electric field vector and the displacement tensor

$$U_0 = \frac{1}{2} E \cdot D. \quad (4)$$

From this the surfaces of constant energy in D space are determined:

$$\frac{D_x^2}{\epsilon_x} + \frac{D_y^2}{\epsilon_y} + \frac{D_z^2}{\epsilon_z} = 2U_0, \quad (5)$$

where ϵ_x, ϵ_y , and ϵ_z are the principal dielectric constants. If we replace $D/2U_0$ by r and define the principle indices of refraction n_x, n_y , and n_z by $n_i^2 = \epsilon_i/\epsilon_0$ ($i=x,y,z$), the previous equation becomes

$$\frac{x^2}{n_x^2} + \frac{y^2}{n_y^2} + \frac{z^2}{n_z^2} = 1. \quad (6)$$

This is the equation of an ellipsoid, known as the *index ellipsoid* or *optical indicatrix*. It determines the two indices of refraction and the two corresponding directions of D associated with the two independent plane

waves that can propagate along an arbitrary direction \mathbf{s} in the crystal.

The impermeability tensor is related to the refractive index tensor by $\eta_{ij} = \epsilon_0^{-1} (\epsilon^{-1})_{ij}$ and the quantum theory of solids predicts that the optical dielectric impermeability tensor depends on the distribution of charges in the crystal. Hence, the application of an electric field will result in a

redistribution of bond charges and possibly a slight deformation of the ion lattice, resulting in a change in the optical impermeability tensor. The phenomena is known as the *electro-optic* effect and the electro-optic coefficients are traditionally defined by

$$\eta_{ij}(\mathbf{E}) - \eta_{ij}(0) = \Delta\eta_{ij} = r_{ijk} E_k + s_{ijkl} E_k E_l \quad (7)$$

where \mathbf{E} is the applied electric field, the constants r_{ijk} are the linear (or Pockels) electro-optic coefficients, and the s_{ijkl} are the quadratic (or Kerr) electro-optic coefficients.

In the principle axis system for the impermeability tensor, ϵ is a diagonal matrix. So

$$\eta_{ij} = \epsilon_0 \begin{pmatrix} \epsilon_{11} & 0 & 0 \\ 0 & \epsilon_{22} & 0 \\ 0 & 0 & \epsilon_{33} \end{pmatrix}^{-1} \quad (8)$$

On applying an electric field to a *non-centrosymmetric* crystal the quadratic term is assumed to be of much smaller magnitude than the linear term and the index ellipsoid becomes

$$\eta_{ij}(\mathbf{E}) x_i x_j = \left(\frac{\delta_{ij}}{n_i^2} + r_{ijk} E_k \right) x_i x_j = 1. \quad (9)$$

where δ_{ij} is the Kronecker delta:

$$\delta_{ij} = \begin{cases} 1, & i=j \\ 0, & i \neq j. \end{cases}$$

For a lossless and optically inactive medium the dielectric tensor ϵ_{ij} is symmetric and so the impermeability tensor η_{ij} must also be symmetric. Consequently the indices i and j can be permuted in the above equation.

The permutation symmetries are summarized as

$$r_{ijk} = r_{jik}$$

Because of the permutation symmetries, it is convenient to introduce

contracted indices to abbreviate the notation. Using this notation $r_{ijk} \Rightarrow r_{mk}$ where

ij	11	22	33	23	13	12
m	1	2	3	4	5	6.

LiTaO_3 is of the rhombohedral crystal class, R3C or C_{3v}^6 space group, 3m or C_{3v} point group and the electro-optic tensor has the form [Yariv and Yeh, 1984]

$$r_{mk} = \begin{pmatrix} 0 & -r_{22} & r_{13} \\ 0 & r_{22} & r_{13} \\ 0 & 0 & r_{33} \\ 0 & r_{51} & 0 \\ r_{51} & 0 & 0 \\ -r_{22} & 0 & 0 \end{pmatrix}_{\text{LiTaO}_3} \quad (10)$$

The contraction of the indices is a matter of convenience and the matrix elements (6x3) do not have the usual tensor transformation or multiplication properties.

When an electric field is applied, the crystal equation (9) will, in general, no longer represent the principle axis system. In a typical alignment, where the field is E_z , the index ellipsoid is described by

$$\eta_{ij} x_i x_j = \left(\frac{1}{n_x^2} + r_{13} E_z \right) x^2 + \left(\frac{1}{n_y^2} + r_{23} E_z \right) y^2 + \left(\frac{1}{n_z^2} + r_{33} E_z \right) z^2 + 2r_{63} xy E_z + 2r_{53} xz E_z + 2r_{43} yz E_z = 1. \quad (11)$$

For LiTaO_3 this expression reduces to

$$\left(\frac{1}{n_x^2} + r_{13} E_z \right) x^2 + \left(\frac{1}{n_y^2} + r_{13} E_z \right) y^2 + \left(\frac{1}{n_z^2} + r_{33} E_z \right) z^2 = 1 \quad (12)$$

The effective refractive indices are field dependent, providing a practical means of altering the relative phase of the E field components of the light beam propagating perpendicular to the z direction.

2.2 Transverse Field Light Modulators

The phase change between polarizations can be determined by placing the crystal between two linear polarizers in a configuration known as a *Pockels cell* as shown in Fig.1 . A linearly polarized beam of intensity I_0

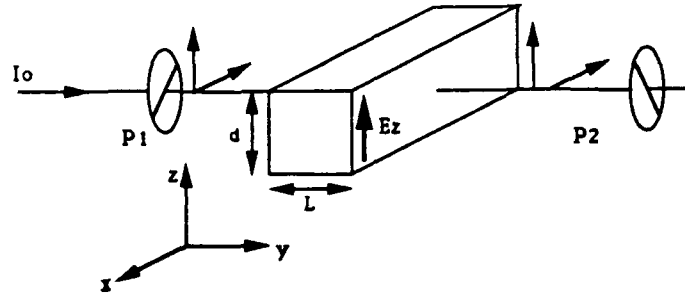


Fig.1 A Pockel's cell. The relative phase shift introduced to the two perpendicular polarizations by the field dependent birefringence alters the intensity I transmitted through polarizer P_2 .

enters the crystal and after propagating a length L through the applied field has a relative phase shift Γ between the two polarizations aligned with the principle axes. The output intensity of the analyzer can be determined using *Jones calculus*, in which matrices represent the amplitude and phase changes introduced to the beam by individual optical components. For the case of a phase inducing material between two crossed polarizers

$$\begin{pmatrix} E'_x \\ E'_z \end{pmatrix} = \frac{1}{2} \begin{pmatrix} 1 & 1 \\ 1 & 1 \end{pmatrix} \begin{pmatrix} 1 & 0 \\ 1 & e^{i\Gamma} \end{pmatrix} \begin{pmatrix} 1 & -1 \\ -1 & 1 \end{pmatrix} \begin{pmatrix} E_x \\ E_z \end{pmatrix}. \quad (13)$$

Hence the intensity of the transmitted beam is

$$I = I_0 \sin^2(\Gamma/2) \quad (14)$$

where $\Gamma = \phi_z - \phi_x = k_0 L(n'_z - n'_x)$ and k_0 is a constant. For LiTaO_3

$$1/n'_x{}^2 = 1/n_x^2 + r_{13} E_z, \text{ and } 1/n'_z{}^2 = 1/n_z^2 + r_{33} E_z.$$

Assuming $1/n_x^2 \gg r_{13} E_z$ and using $dn = -\frac{1}{2} n^3 d(1/n^2)$

$$1/n'_x{}^2 - 1/n_x^2 \approx d(1/n_x^2) = r_{13} E_z$$

$$n'_x - n_x \approx dn_x = -\frac{1}{2} n_x^3 r_{13} E_z.$$

From this, an expression for the field dependent refractive index can be obtained;

$$n'_x = n_x - \frac{1}{2} n_x^3 r_{13} E_z.$$

Similarly

$$n'_y = n_y - \frac{1}{2} n_y^3 r_{13} E_z,$$

and

$$n'_z = n_z - \frac{1}{2} n_z^3 r_{33} E_z.$$

So the phase shift introduced between the two polarizations of a beam travelling in the y direction is

$$\Gamma = \frac{2\pi}{\lambda} (n'_y - n'_x) L - \frac{\pi}{\lambda} (n_x^3 r_{33} - n_y^3 r_{13}) E_z L \quad (15)$$

where L is the distance travelled through the field and λ is the free space wavelength.

2.3 Half-wave Voltage

The half wave voltage, V_π is a useful parameter for characterizing electro-optic modulators. It is the voltage required to introduce a phase shift between the emerging orthogonal polarizations by π radians and is often quoted as a measure of Pockels cell responsivity.

$$V_\pi = \lambda d / (L(n_x^3 r_{33} - n_y^3 r_{13})) \quad (16)$$

where d is the separation of the electrodes. For the LiTaO₃ modulator described in section 3, with d = 0.7 mm, L taken to be 0.3 mm, $\lambda = 580$ nm and $n_x^3 r_{33} - n_y^3 r_{13} = 2.285 \times 10^{-10}$ m/V the half-wave voltage is

$$V_\pi = 5.9 \text{ KV.}$$

2.4 Quarter-wave Phase-shift Bias

From equ 14 the intensity change as a function of phase shift is maximum when the Γ is $\pi/2$ and at this phase shift the relationship is approximately linear as shown in Fig.2. Advantage of these characteristics can be made by introducing an adjustable (Soliel-Babinet) compensator into the beam path and tuning to introduce a constant phase shift $\Gamma_0 = \pi/2$. In this way the sensitivity to small phase shifts, $\Delta\Gamma = \pi V/V_\pi$, introduced by variations in field strength, given by

$$I = I_0 \sin^2((\Gamma_0 + \Delta\Gamma)/2) \quad (17)$$

is maximized and most linear. Here V is the voltage associated with the field E_z . Note that $\Gamma_0 = \pi/2$ and small $\Delta\Gamma$, $I \approx (I_0/2)(1 + \Delta\Gamma)$.

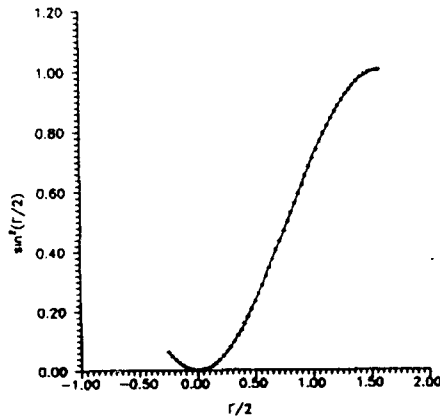


Fig.2 A linear response the transmitted beam is obtained for small phase changes at the quarter wave bias point ($\Gamma_0 = \pi/2$).

2.5 Microstrip Design

The field E_z need not be constant. In fact the rapid time variation of the field is the motivation for the use of electro-optic sampling. The response time of the polarization of the crystal is of the order of femtoseconds, hence the modulation can occur on short time scales, providing an opportunity for characterization of rapidly changing fields.

To provide an accurate means of determining short duration field pulses, propagation from the point of origin to the probing location within the LiTaO_3 must occur with minimum distortion of the field. Such a requirement places constraints on the wave-guiding structure used. In general, wave guides support more than one mode, and the phase velocity of each mode is frequency dependent giving rise to dispersion. Any discontinuities in the wave-guide excite all modes and give rise to reflections. Of the numerous waveguiding structures in use, *balanced stripline* (Fig.3) and *coplanar stripline* provide suitable transmission line geometries. The case of a balanced stripline is described here. Because of its symmetry it can be analyzed as a *microstrip* of height h in which the LiTaO_3 serves as a substrate for thin film metal conductors of width w . Since the field lines between the narrow conducting strip and the ground plane do not lie entirely inside the substrate the propagating mode is not truly transverse electromagnetic (TEM) but quasi-TEM. The field lines lie in two media, the substrate and the vacuum, and as a result the relative

dielectric constant, ϵ_r , does not provide an accurate description of the phase velocity and is replaced by the effective dielectric constant, ϵ_{eff} , which is smaller than ϵ_r .

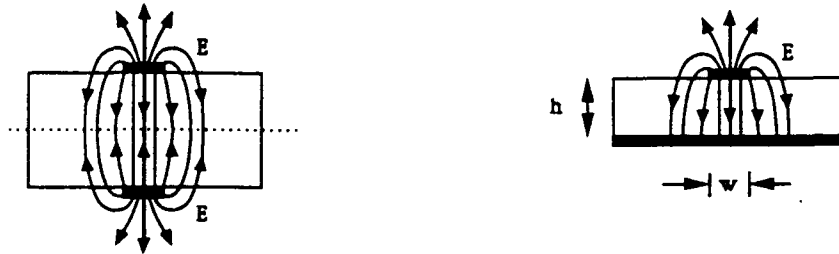


Fig.3 (a) Balanced stripline

(b) Microstrip.

The phase velocity in the microstrip is given by

$$v_p = c/\epsilon_{eff}$$

and the transmission line characteristic impedance is

$$Z_0 = 1/v_p C$$

where C is the capacitance per unit length of the line.

In the first electro-optic measurements made the pulse source was external to the microstrip and standard 50 Ω connectors and coaxial lines were used to connect the two. To minimize the discontinuity at the transition. The distance between the inner and outer conductors of the connector was be matched to the height of the stripline, 2h.

Closed forms of expressions for the determination of transmission line parameters have been determined by a number of authors and are outlined in the review of Bahl and Trivedi (1977). Hammerstad (1975) provides an accurate expression for determination of the characteristic impedance in terms of the relative dielectric constant.

For $w/h \leq 1$,

$$Z_0 = (60/\sqrt{\epsilon_{eff}}) \ln(8.h/w + 0.25 W/h)$$

where

$$\epsilon_{eff} = \frac{\epsilon_r + 1}{2} + \frac{\epsilon_r - 1}{2} [(1+12.h/w)^{-1/2} + 0.04(1-w/h)^2]$$

and for $w/h \geq 1$,

$$Z_0 = \frac{120 \pi \sqrt{\epsilon_{eff}}}{w/h + 1.393 + 0.667 \ln(w/h + 1.444)}$$

where

$$\epsilon_{eff} = \frac{\epsilon_r + 1}{2} + \frac{\epsilon_r - 1}{2} (1 + 12.5 h/w)^{-1/2}. \quad (18)$$

The w/h ratio obtained from Hammerstad's expression are plotted in Fig.4 as a function of Z_0 .

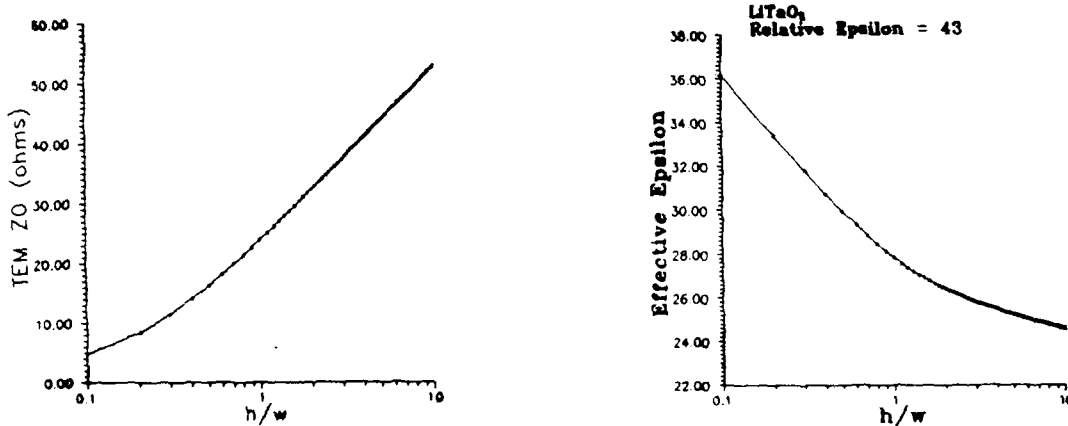


Fig.4 (a) The calculated microstrip impedance, and (b) the effective dielectric constant as a function of the microstrip height to width ratio as predicted by Hammerstad, 1975.

At higher frequencies the electric field lines are contained more within the substrate and ϵ_{eff} tends to ϵ_r which is frequency dependent. For waveforms with a broad frequency spectrum the varying phase velocities result in a change in the pulse shape with the distance travelled. Maintaining short distances between the pulse source and the probe location are, therefore, important to minimize the effects of dispersion.

2.6 Velocity Matching of the Pulse and Probe Beam.

As described so far the pulse and probe beam propagate perpendicular to one another in the crystal. In this geometry the length of the field pulse interacting with the probe beam is not simply the beam diameter, account must also be taken of the propagation of the pulse as it is traversed by the probe. This is illustrated in Fig.5 where the probe enters the pulse at A when the field location is specified by E_1 . At time t later, $t = d/u' = (W/\cos\alpha)(n/c)$ where d is the length travelled by the field pulse at

velocity v' in the crystal of refractive index n by the probe, the probe emerges at position B and the field has propagated to E_f . The field pulse travels a distance d_2 at speed v in time t , and the relative pulse and probe speed in the x direction is $v-v'$. Therefore a probe pulse of a zero width beam integrates features extending over a time τ ,

$$\tau = \left(\frac{v' - v}{v} \right) t \quad (19)$$

in the field. Substituting $v' = (n/c)\sin\alpha$ and $v = 1/(\epsilon_0 \epsilon_{eff} \mu_0)^{1/2}$ we obtain

$$\tau = (n - \sqrt{\epsilon_{eff}} \sin\alpha) \frac{W}{c \cdot \cos\alpha} \quad (20)$$

where c is the vacuum velocity of light. For the case of zero integration, i.e. $\tau = 0$

$$n = \sqrt{\epsilon_{eff}} \sin\alpha. \quad (21)$$

Snell's Law determines the angle of incidence of the probe beam:

$$\sin\beta = n^2 / \sqrt{\epsilon_{eff}}. \quad (22)$$

For the average value of n_o and $n_e = 2.1856$ and $\epsilon_{eff} = 26.0$, calculated from equ 18, $\beta = 69.5$ degrees. The case where $\alpha = 0$ leads to $\tau = nW/c = 2.1856$ ps, indicating that for pulse widths < 20 ps velocity matching will significantly improve the time resolution.

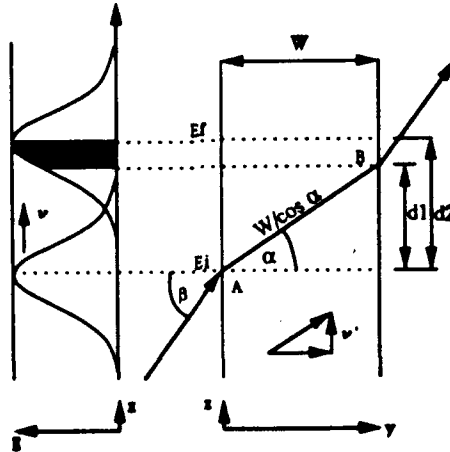


Fig.5 Velocity matching of the field and probe pulses by adjustment of the angle β improves temporal resolution.

2.7 Characterization and Reduction of Noise.

Noise on a signal is usually detrimental, imposing a practical limit

to the performance of the circuit. Noise is due to inherent effects in the system rather than spurious effects such as a faulty contact which could be eliminated. The three most commonly encountered types of noise are thermal, shot and 1/f noise [Buckingham, 1983].

Thermal noise arises from the random velocity fluctuations of the charge carriers (electrons and holes) in the resistive material. The mechanism is Brownian motion of the charge carriers due to the thermal energy of the material. Thermal noise is present when the resistive element is in thermal equilibrium with its surroundings and is often referred to as *Johnson noise*. The open circuit noise voltage of a resistor has a flat spectrum, that is the noise power in each hertz of frequency is a constant. The noise generated by a resistance R_L at temperature T is

$$V_{JN}(\text{rms}) = (4kTR_L B)^{1/2} \quad (23)$$

or written in terms of the mean square current

$$\overline{i_{JN}^2} = 4kTB/R_L, \quad (24)$$

where k is Boltzmann's constant and B is the bandwidth of the detector in hertz. (At 20°C $4kT = 1.62 \times 10^{-20} \text{V}^2/\text{Hz}\cdot\Omega$)

Shot noise is associated with the passage of current across a barrier, and in this sense is a non-equilibrium form of noise. Shot noise is frequently encountered in solid-state devices, whenever a net current flows across a potential barrier such as a depletion layer of a p-n junction. To illustrate the nature of shot noise, consider the example of a thermionic diode in which the electrons are randomly emitted from the cathode and then drift across to the anode under the influence of an electric field. The current associated with the stream of electrons fluctuates randomly about a mean value. If the charges act independently of one another, then the fluctuating current is given by

$$i_{SN} = (2qI_{dc} B)^{1/2} \quad (25)$$

where q is the electron charge.

1/f noise is a noise found in all systems and has been resilient to theoretical understanding but must be considered when establishing the noise level of a system. It is so named because the power density spectrum varies with frequency f as $|f|^{-\alpha}$, where α lies in the range $0.8 < \alpha < 1.2$.

All forms of noise are present to some degree at all frequencies,

however, at high enough detection frequencies the contribution by $1/f$ noise is negligible. The other contributions to noise can be reduced by narrow bandwidth measuring techniques. Assuming, temporarily, that the $1/f$ noise can be neglected the minimum detectable voltage can be determined from the signal to noise ratio where noise contributions are of the Johnson and shot types. For a photodiode current in a load resistor R_L the signal power is

$$P_{sig} = \overline{i_{sig}^2} R_L \quad (26)$$

and the total noise power is

$$P_{noise} = (\overline{i_{JN}^2} + \overline{i_{SN}^2}) R_L = 4kTB + 2qi_{DC}BR_L. \quad (27)$$

Hence, the signal to noise ratio is

$$S/N = \frac{\overline{i_{sig}^2} R_L}{4kTB + 2qi_{DC}BR_L}. \quad (28)$$

An illustrative measure of the signal to noise ratio (S/N) is obtained by considering a particular form of signal, for example, the case of the transmission line driven by a signal generator of output $V_0 \sin \omega t$ of small amplitude.

The modulated probe beam intensity of equ 17 can be written as

$$I = (I_0/2)(1 - \cos(\Gamma_0 + \Delta\Gamma)) \quad (29)$$

which for small $\Delta\Gamma$ reduces to

$$I = (I_0/2)(1 - \cos\Gamma_0 + \Delta\Gamma \sin\Gamma_0). \quad (30)$$

When the transmission line is driven by a signal generator of output $V_0 \sin \omega_m t$

$$\Delta\Gamma = (\pi V_0 / V_\pi) \sin \omega_m t, \quad (31)$$

hence the total current produced by a detection photodiode (see section 3) is

$$i_{tot} = \frac{i_0}{2} [1 - \cos \Gamma_0 + \frac{\pi V_0}{V_\pi} \sin \omega_m t \sin \Gamma_0]. \quad (32)$$

The average and time varying signals can be separated to yield

$$i_{DC} = \frac{i_0}{2} [1 - \cos \Gamma] = i_0 \sin^2(\Gamma_0/2) \quad (33)$$

$$i_{sig} = \frac{i_0}{2} \frac{\pi V_0}{V_{\pi}} \sin \omega_m t \sin \Gamma_0. \quad (34)$$

The mean squared shot-noise current density is thus

$$i_{SN}^2 = 2qi_{DC} = 2qi_0[\sin^2(\Gamma_0/2)] \quad (35)$$

and the mean squared signal current is

$$\overline{i_{sig}^2} = \frac{i_0^2}{8} \frac{\pi V_0^2}{V_{\pi}} \sin^2(\Gamma_0/2) \quad (36)$$

$$\Rightarrow S/N = \frac{\frac{i_0^2}{8} \frac{\pi V_0^2}{V_{\pi}} \sin^2(\Gamma_0/2)}{(2qi_0 \sin^2(\Gamma_0/2) + 4kT/R_L)B} \quad (37)$$

Setting $S/N = 1$,

$$(V_0)_{min} = \frac{4V_{\pi}}{\pi i_0} \left(\frac{(i_0 \sin^2(\Gamma_0/2) + 2kT/qR_L)qB}{\sin^2 \Gamma_0} \right)^{1/2} \quad (38)$$

For $\Gamma_0 = \pi/2$, $R_L = 1 \text{ K}\Omega$, at 300 K $2kT/qR_L = .51e-4$ and the expression is dominated by the first term in the numerator, so

$$(V_0)_{min} = \frac{V_{\pi}}{\pi} 2 \sqrt{qB/i_{DC}} \text{ volts.} \quad (39)$$

For a detection bandwidth of $B \approx 1 \text{ Hz}$, i_{DC} determined from the responsivity of the photodiode, and the V_{π} of section 2.3 the minimum detectable signal in the absence of $1/f$ noise is $(V_0)_{min} \approx 80 \mu\text{V}$.

2.8 Signal Measurement.

Probe beam intensities, I , are determined from the photocurrent response of a photodiode. The voltage developed across the load resistor R_L in response to the photocurrent is measured using the phase sensitive detection of a lockin amplifier. This method increases the signal to noise ratio via bandwidth narrowing. The signal to be measured is superimposed on noise and a means of preserving the signal while reducing the amount of (broadband) noise accepted is required. The use of a low-pass filter may work in some cases but where signal to noise ratios are low this is inadequate. A combination of modulation, to shift the signal to a low density part of the

noise spectrum, and signal averaging, to reduce the bandwidth, provides an increased signal to noise ratio. Bandwidth reduction is accomplished by long periods of data accumulation, reducing the effective bandwidth to $\Delta f=1/\tau$, where τ is the time constant.

Filtering the shifted signal with a bandpass filter of high Q would require accurate tuning of the center frequency and a slight mistuning would result in large errors. To overcome this problem the lockin amplifier first rectifies the incoming signal and then filters it. To accurately rectify, a reference signal synchronized to the modulation signal is required. The phase detector circuit of the lockin amplifier is shown schematically in Fig. 6.

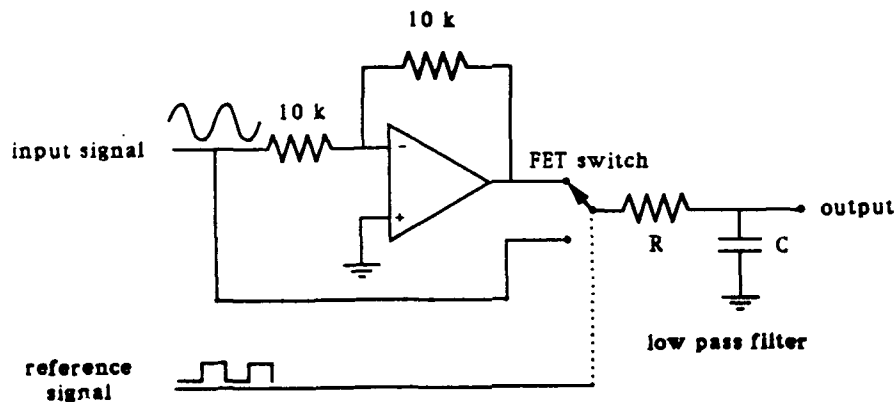


Fig.6 The reference signal to the FET switch rectifies the lockin amplifier input signal prior to low pass filtering that enhances the signal to noise ratio.

Assume that the applied signal is $E_s \cos(\omega t + \phi)$ and that the reference signal is a square wave with transitions at the zeros of $\sin(\omega t)$. Rectification is achieved by switching and the output is averaged by a low-pass filter of time constant greater than one period:

$$\tau = RC \gg T = 2\pi/\omega$$

Then the low-pass filter output is

$$\langle E_s \cos(\omega t + \phi) \rangle \Big|_0^{\pi/\omega} - \langle E_s \cos(\omega t + \phi) \rangle \Big|_{\pi/\omega}^{2\pi/\omega} = \frac{-2E_s}{\pi} \sin \phi. \quad (40)$$

The phase difference ϕ is between the input and the reference signals. The argument extends to more general periodic input waveforms. Hence the bandwidth narrowing capabilities of the lockin amplifier significantly increase the signal to noise ratio.

3.0 EXPERIMENTAL APPARATUS AND MEASUREMENTS.

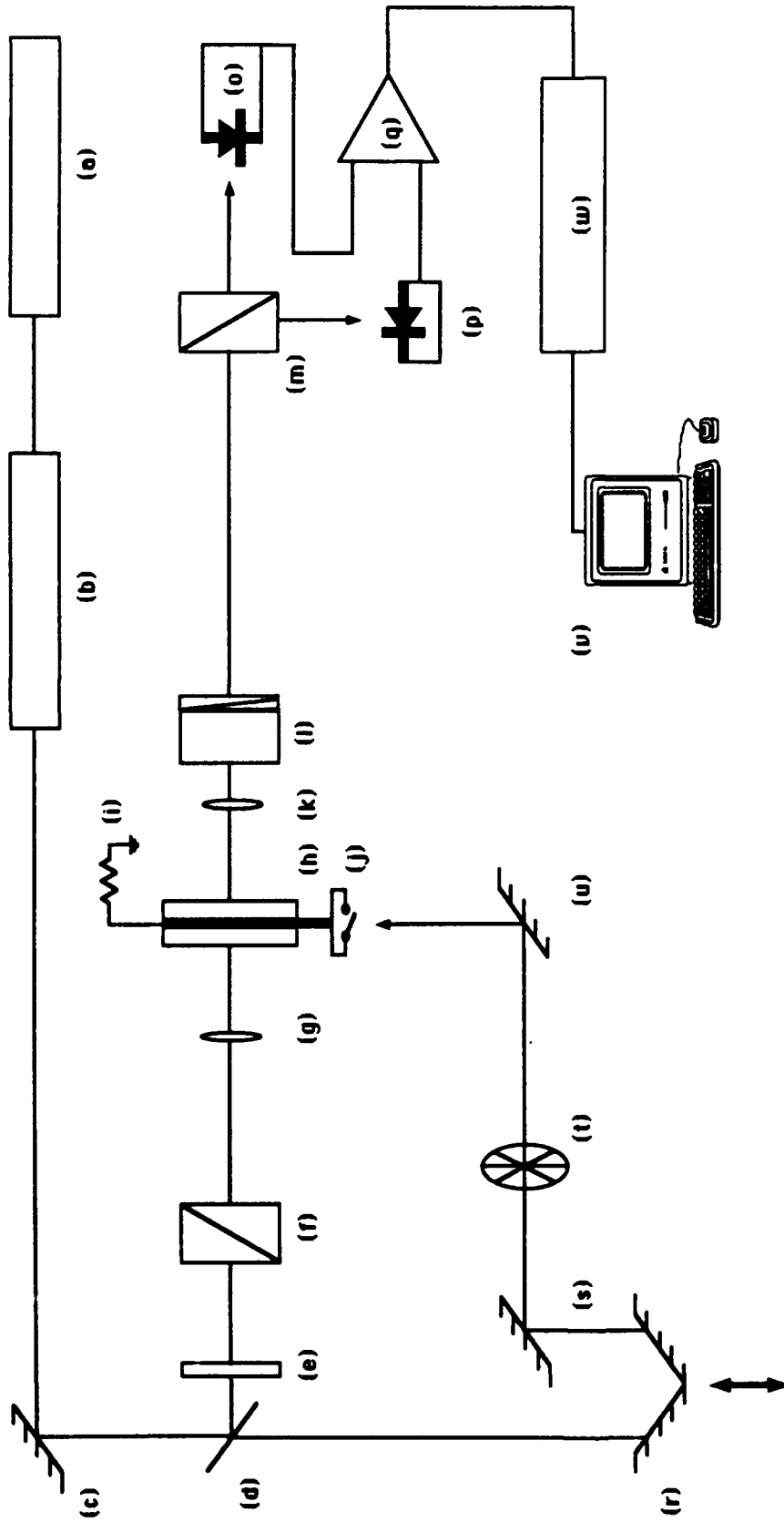
Fig.7 illustrates the arrangement of components used for electro-optic sampling. The synchronous pump and probe beams originate from a cw modelocked (82 MHz) Ar ion (Spectra-Physics model 171-07) pumped dye laser (Spectra-Physics model 375). The dye type was rhodamine 6G and output pulses were of ≈ 7 ps FWHM autocorrelated and the wavelength range was 560-600 nm. Glan-laser double escape window polarizing prisms (Karl Lambrecht) selected for extinction ratio of $1e-6$ were oriented at 90 degrees to one another and functioned as polarizer and analyzer of the Pockel's cell. These prisms transmit one polarization and reflect the second at approximately 65 degrees to the optical axis, rendering both polarizations available for determination of the phase change of the beam (see appendix A).

Microscope eyepiece lenses of focal length 11 mm focused the beam into the LiTaO_3 . The free space beam waist can be determined from the results of paraxial theory applied to Gaussian beams (Kogelnick, 1965) and is well approximated by

$$w = w_0 \frac{f/z}{(1 + f/z)^{1/2}} \quad (41)$$

where $z = \pi w_0^2/\lambda$, w_0 is the beam diameter incident on the focusing lens and λ is the wavelength. The beam diameter was determined using the knife-edge techniques of Khosrofian and Garetz, 1983 and Suzaki and Tachibana, 1975 which infer the diameter from the intensity propagating beyond a partially blocking knife edge as a function of knife-edge position. Respectively the beam diameters obtained were 0.98 and 1.01 mm. Substituting the average of these into equ 41 the beam waist diameter obtained, $2w$, is $4.4 \mu\text{m}$.

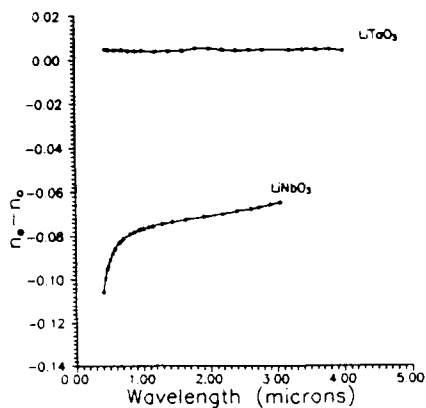
Aluminum electrodes of width 0.3 mm were evaporatively deposited on the LiTaO_3 to form the balanced transmission line with the large component of the field in the direction of the optical axis of the crystal. The substrate dimensions were 0.5 x 0.7 X 10.0 mm and the two narrow faces were optically polished for transparency to the probe beam. The remaining faces were lapped flat. LiTaO_3 was chosen in preference to LiNbO_3 because of its larger electro-optic response to a given applied field, Fig. 8(a). The substrate was mounted with one conducting film in contact with a brass support electrode of the same width. At each end a 27 GHz SMA connector was used to connect to the applied bias and a terminating resistor as shown in Fig.9. Termination and signal display were performed by a high speed oscilloscope.



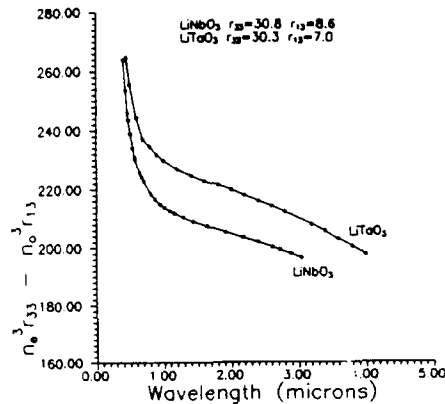
- (a) Ar ion laser
- (b) dye laser
- (c), (s), (u) mirror
- (d) beam splitter
- (e) half wave plate
- (f) beam splitting polarizing prism
- (g), (k) focusing, collimating lenses
- (h) birefringent sampling head
- (i) terminating resistor

- (j) optically activated switch
- (l) Soliel-Babinet compensator
- (o), (p) FND-100 photodiodes
- (q) differential amplifier
- (r) translating delay stage
- (t) beam chopper
- (v) computer
- (w) lockin amplifier

Fig. 7 ELECTRO-OPTIC SAMPLING SYSTEM



(a)



(b)

Fig.8 (a) Field dependent birefringence and (b)static birefringence (b) of LiTaO_3 and LiNbO_3 .

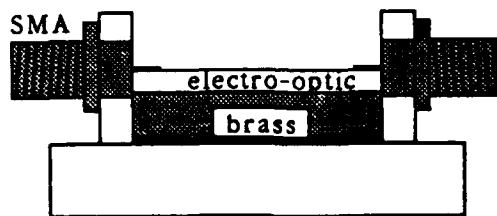


Fig.9 Connector and mount geometry of the electro-optic (LiTaO_3) transmission line.

Both LiNbO_3 and LiTaO_3 have non-zero birefringence when there is zero applied field, i.e. they have non-zero static birefringence, fig 8(b). A Soliel-Babinet compensator was used to both zero the phase shift introduced by the birefringence and to set the phase shift to the quarter wave bias point described in section 2.4.

FND-100 (EG&G Photon Devices) photodiodes were selected to detect the emerging polarization intensities because of their large surface area and high responsivity in the visible part of the spectrum. They were reverse biased (90 volts), and the voltage generated across a 1 K Ω load resistor was monitored on a DC voltmeter (Hewlett Packard E2373A) to determine the phase bias, see Fig.10. The output was also AC coupled with a 0.1 μF capacitor and the periodic waveform amplitude, due to the polarization change, measured using a lockin amplifier (Stanford Research, SR510)

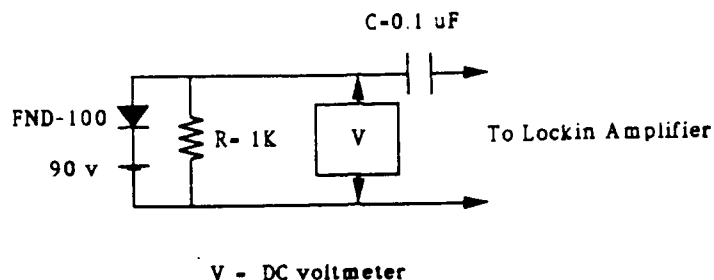


Fig. 10 Photodiode bias circuit, DC voltmeter for phase shift determination and AC coupling to the lockin amplifier.

Measurement of the field strength across the entire pulse width requires variation in the relative delay between the arrival time of the pump and probe pulses at the location of interaction within the sampling head. The variation was accomplished by changing the path length of the pump beam optical arm using a 180 degree reflector mounted on a translation stage (Klinger).

The signal periodicity and the reference waveform required by the lock-in amplifier for bandwidth narrowing were provided by a mechanical beam chopper (Stanford Research SR540), operating at 2 KHz, placed in the pump beam. At each time delay the lockin amplifier was allowed time to settle, determined by the selected time constant, τ , and the output was repeatedly sampled and data recorded and displayed on a computer. The signal to noise ratio is improved by longer settling times and larger number of samples, however, this leads to longer total experiment times during which laser and thermal instabilities of the electro-optic medium effect the detected signal. Hence, there is a compromise to be made between elimination of higher frequency noise and long term drift. Typically the time constant was chosen to be 300 ms.

Characterization of the relationship between an applied voltage and the system response a voltage of the form $V_0 \sin(\omega t)$ was applied to the LiTaO_3 modulator, and lockin voltage recorded. A typical response with slope of 4.71×10^{-3} is shown in figure 11. Many applications of the electro-optic sampling system demand high sensitivity. Hence calibration was extended to lower applied voltages. Figure 12 shows three examples of the system response in which the lockin amplifier output was sampled a different number of times at each applied voltage. The response is linear to within experimental error and the signal to noise ratio is seen to improve as the number of samples is increased from 1 to 200.

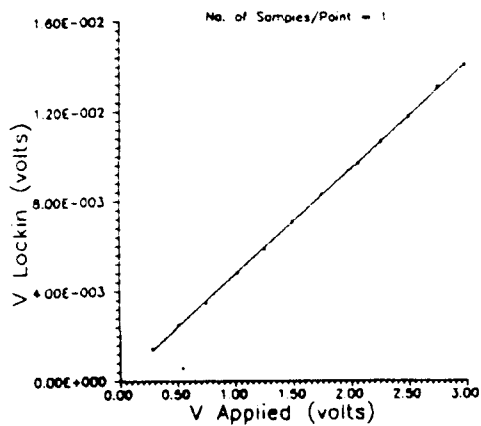


Fig. 11 Linear response of the electro-optic sampler to applied bias.

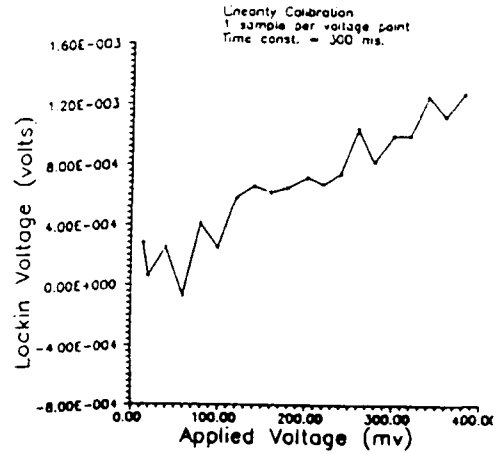


Fig 12(a)

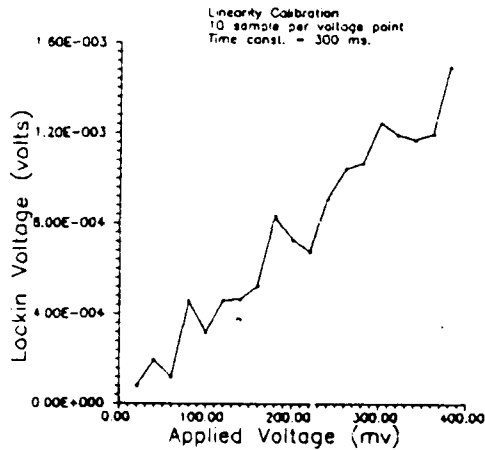


Fig. 12(b)

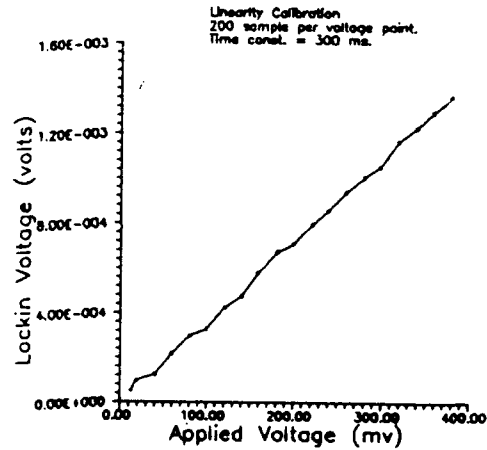


Fig. 12(c)

Fig. 12 The signal-to-noise ratio is enhanced by increasing the number of samples measured at each applied bias.

The potential for signal to noise enhancement was determined by repeated sampling of the lockin amplifier. The applied voltage was held constant and five data sets of n measurements were made, each measurement consisted of sampling the lockin amplifier m times. The average values and standard deviation are summarized in table 1 and fig 13.

Data Set	1	2	3	4	5
n	19	19	19	9	9
m	1	10	20	100	200
σ_{n-1} (*1e5)	5.23	2.67	2.92	1.57	1.22
\bar{x} (*1e3)	5.75	5.75	5.79	5.79	5.73

Table 1.

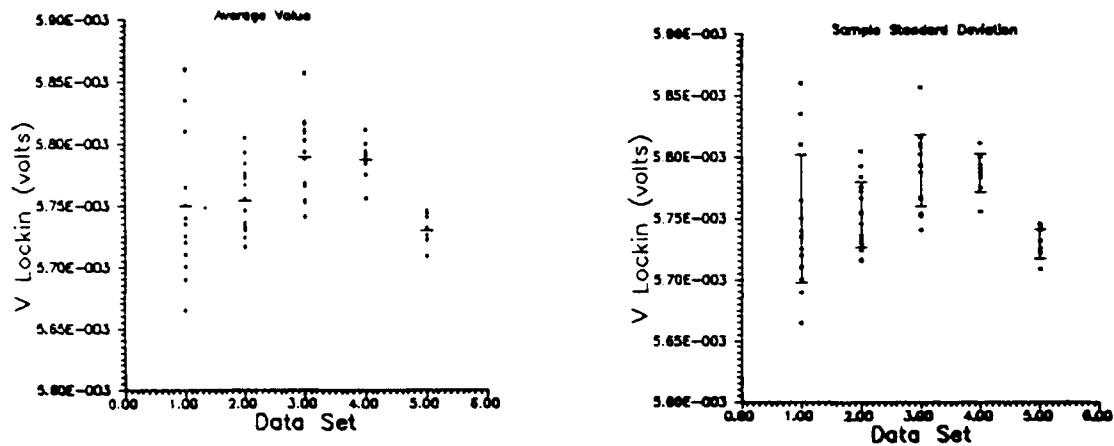


Fig.13 The average value and sample standard deviation for 1,10,20,100,200 samples at constant applied bias.

The standard deviation and the slope were used to determine the minimum resolvable voltage (sensitivity) for each data set.

no. of samples	1	10	20	100	200
sensitivity (mV)	22.4	11.5	12.5	6.5	6.7

By recording 200 samples at each applied voltage the error on the measured signal is reduced to 6.7 mV and the response is linear within the error. Recalling that the electrode separation is 0.7 mm, the minimum resolvable field is 0.095 V/cm and the minimum resolvable $E_z L$ product is 28.5 e-4 volts.

For short duration pulse field measurements it is necessary that the pump and probe beam path lengths result in the same delay to within the accuracy of the pulse duration. Careful measurement of the arm lengths is essential. The synchronous arrival of the pulses at the sampling head was

checked by temporarily replacing the LiTaO_3 by a cubic beam splitter. Alignment was such that both beams were incident on the same position of the reflecting face. The transmitted 50% of the pump beam and the reflected 50% of the probe beam were colinear and directed onto a fast photodiode (risetime=35 ps), the output of which was displayed on an oscilloscope. While monitoring the time difference between the two pulses the necessary minor adjustments of the arm lengths were made.

3.1 Electro-optic Sampling Measurements

As a test of the electro-optic sampling system a commercial photodiode (Antel ARS-2) was switched by the pump beam and the emerging pulse launched onto the balanced stripline. The connection was via 50 Ω , 27 GHz SMA connectors and the line was terminated with a Tektronix oscilloscope S4 sampling head (see fig 14). Fig.15 shows electro-optically determined field pulses at four x positions in the crystal. The pulse is launched into the crystal at $x = 0$ and measured at $x = 1.0, 4.0, 6.0$ and 8.5 mm. A lockin time constant of 300 ms was used and at each position 200 samples were taken. An approximate measure of the resulting sensitivity is obtained noting that the signal to noise ratio in the figure is approximately 1 in 60 and multiplying this value by the 150 mV amplitude of the signal measured on the oscilloscope. The resolution is then approximately 2.5 mV which is in agreement within a factor of three with the sensitivity determined above in section 3.0.

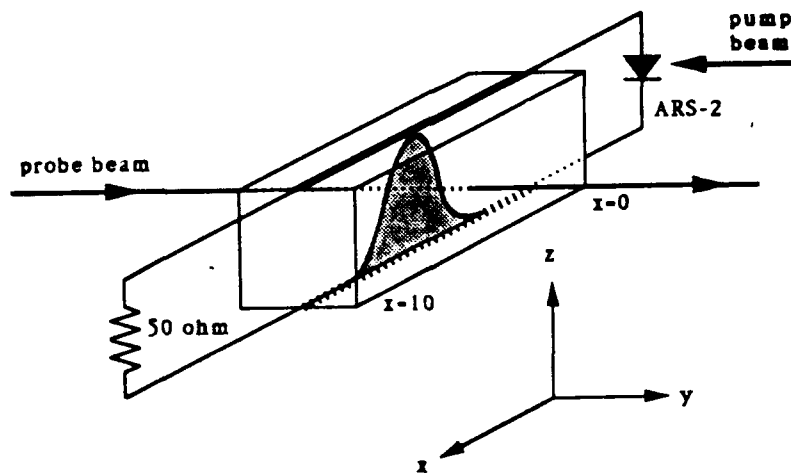


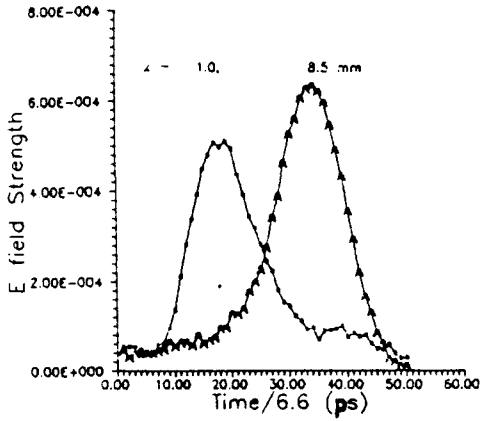
Fig.14 A pulse launched from a photodiode is sampled by the probe beam at position x.

The change in pulse shape as it propagates on the line is the result of dispersion and reflection. A full-wave analysis (see for example Carin and Webb, 1989) using a spectral domain formulation was made for a square pulse of similar gross features to that generated by the photodiode. The field strength was determined as a function of time at positions $x = 0$ and $x = 10$ excluding, Fig 17(a), and including, Fig 17 (b), the effects of dispersion. The effects of reflection and subsequently dispersion are seen to be significant in the development of the waveform. These phenomena can be expected to play a role in the evolution of the pulse propagating in the balanced stripline.

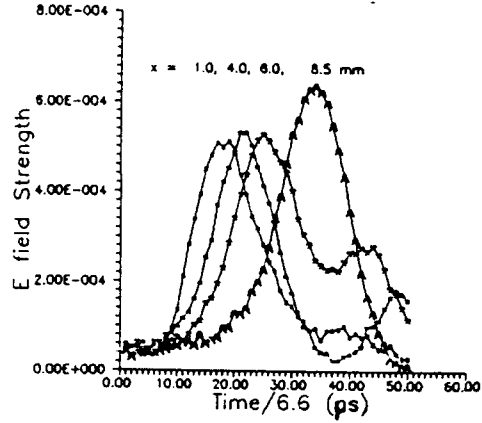
The characteristics of the electro-optic sampling system are a spatial resolution of less than $10 \mu\text{m}$, a sensitivity of less than 7 mV , and time resolution of approximately 7 ps . The pulse widths demonstrated are approximately 120 ps FWHM but it is at widths of $< 20 \text{ ps}$ that the technique offers measurement opportunities not available by other means. This time resolution is limited by the duration of the laser pulse, not the electro-optic effect or detection electronics, hence the temporal resolution could readily be improved by provision of shorter duration laser pulses.

The device has been used to map electric field pulses at several positions in a microstrip transmission line as a function of time. The measured pulse shapes closely resemble those calculated using an approximate model and this application demonstrates that the technique could be extended to determine reflection and transmission coefficients of pulses at interfaces, however, the purpose of this work is to provide a means of studying transient field dynamics in high power switches. Hence, the next step is to incorporate short time-scale semiconductor switches with the system.

The next section outlines the phenomena experienced by carriers at metal-semiconductor contacts, an inherent part of any switch geometry, and initial steps taken to fabricate metal-semiconductor contacts.

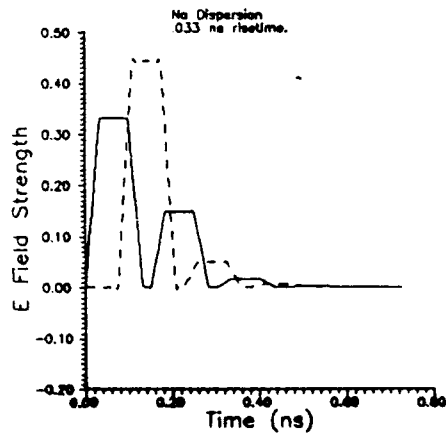


(a)

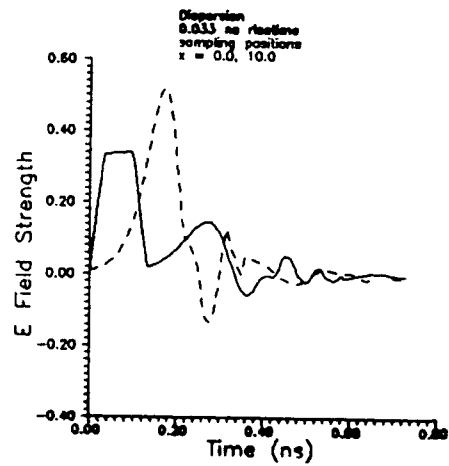


(b)

Fig. 15 Pulse shapes as a function of time at (a) two x positions and (b) four x positions.



(a)



(b)

Fig.16 Theoretically modeled pulse shapes at $x = 0$ and $x = 10$ mm for a square pulse input both without (a) and (b) with dispersion included in the model.

4.0 PHOTOCONDUCTIVE SWITCHES.

The switching times of semiconductor materials are determined by carrier production and recombination. Materials such as GaAs and silicon-on-sapphire are known to have recombination times of the order of several picoseconds. Such materials appropriately biased are thus capable of producing field pulses a few picoseconds in duration. Hence, they provide a more stringent test of the electro-optic sampling system or alternatively electro-optic sampling serves as a means of investigating the switching characteristics. In designing a suitable switch, consideration must be given to bulk and metal-semiconductor interface phenomena as the significance of the role of each to current limitation varies with material, geometry and applied bias. As an initial step in the development of switches for the study of carrier transport this section outlines the phenomena occurring at metal-semiconductor interfaces and describes some preliminary results of fabrication.

4.1 Metal Semiconductor Contacts

Metal semiconductor contacts are inherent in photoactivated semiconductor switches. Schottky, Stormer and Waibel (1931) showed that the potential drop in a metal-semiconductor-metal system occurs predominantly across the contact region. This implies that there is some form of barrier to conduction at the metal-semiconductor interface. Braun (1874) demonstrated that the current flows more easily in one direction than the other at the contact, i.e. the contact has rectifying properties. These properties were exploited extensively in radio broadcasting long before they were understood. The high resistance in one direction but not in the other was presumed due exclusively to a layer of foreign materials at the interface prior to work of Schottky (1938, 1939) and Davidov (1939) who showed that asymmetric behavior could arise as the result of the accumulation of space charge. It was also realized that equilibrium contact conditions at every contact between different materials involves charge exchange and although quantum mechanics predicts non-linear behavior at any lattice discontinuity space charge effects dominate.

4.2 Space Charge at the Interface.

Space charges are always present at interfaces and this can be

representatively demonstrated by considering two materials in contact and having a common current. Ohm's law states that $J = \sigma E$ and if we assume that $\sigma_1 \neq \sigma_2$ then $E_1 \neq E_2$ in the bulk sections. The non zero divergence at the interface and Poisson's equation $\nabla \cdot E = \rho / \epsilon$ leads to the conclusion that the space charge density, ρ , at the interface is non zero. This situation results to a double layer of space charge at the interface as illustrated in Fig. 17.

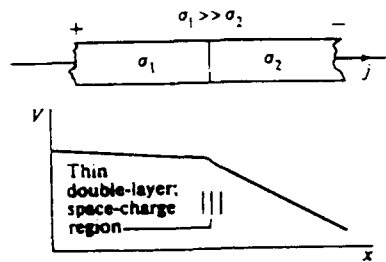


Fig. 17 Potential contour at any current-carrying contact between two materials of different carrier concentration (conductivity). Note the existence of space-charge double-layer at interface.

The flux term of the continuity equation, $J = e(n\mu E + D \cdot \nabla n)$, describes the general current density. For the special case of no gradients in the carrier density, n , this reduces to Ohm's law, $J = \sigma E$. The diffusion current density, $eD \cdot \nabla n$, is a departure from Ohm's law and arises because of the space charge density. This argument leads to the conclusion that third phases are not required for a non-linear resistance behavior in the contact but can be solely the result of space charge at the contact.

4.3 Formation of the Schottky Barrier.

Barriers arise in two distinctly different ways. Firstly through the difference in thermionic work functions of the two materials and secondly, from the action of surface states. Consider first, the difference in the thermionic work functions of materials for the case $\phi_s < \phi_m$, an important practical case. When the metal and semiconductor are separated the Fermi level of the N doped semiconductor is greater than that of the metal as in Fig. 2a. Here χ_s is the electron affinity of the semiconductor. On bringing the metal and semiconductor into thermal equilibrium by, for example connecting them with a wire (fig. 18b), the Fermi levels align and there is a net transfer of electrons from the semiconductor to the metal. These

electrons are provided by the donor atoms and as a result of the charge transfer there exists both a potential difference, V_1 , between the vacuum level in the semiconductor and that of the metal and a depletion layer of width w extending from the face of the semiconductor. The number density of donor atoms is orders of magnitude lower than the free electron concentration in the metal, hence the depletion layer is much thicker than the excess charge layer in the metal. As the separation is decreased (fig. 18c) the magnitude of the E field would tend to increase without limit. This, however, is not physical and is averted by the further transfer of electrons from the semiconductor to the metal until when in contact, Fig. 18d, the voltage V_1 is zero. The potential ϕ_{ns} ($= \phi_m - \chi_s$) is the barrier potential, the energy an electron at the Fermi level of the metal must gain to be raised over the top of the barrier and into the semiconductor. The voltage V_D associated with the energy between the bottom of the conduction band in the semiconductor bulk and the top of the barrier is known as the diffusion potential.

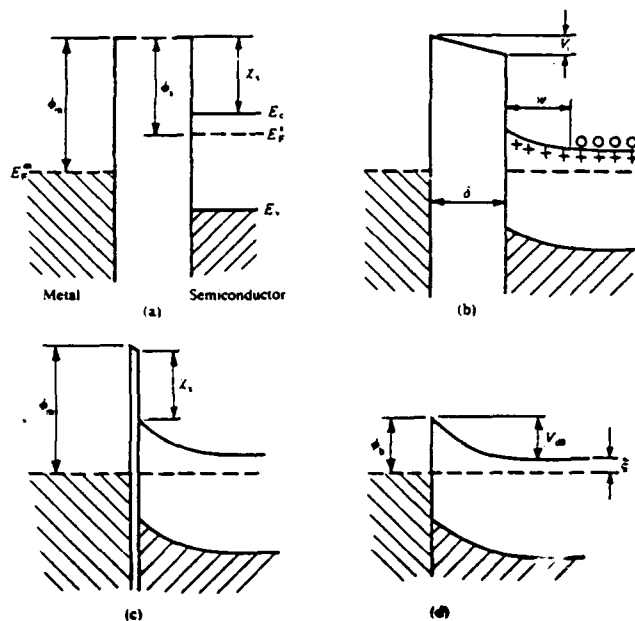


Fig. 18 Formation of a barrier between a metal and a semiconductor (a) neutral and isolated, (b) electrically connected, (c) separated by a narrow gap, (d) in perfect contact. o denotes electron in conduction band; + denotes donor ion.

The classical shape of the Schottky barrier (1938) is parabolic. This can be shown by assuming the semiconductor is homogeneous up to the boundary, that the uncompensated donors give rise to a uniform space charge density in the depletion region that is continuous rather than discrete. By twice integrating Poisson's equation for the depletion region the energy of the bottom of the conduction band is determined. For N-type material of permittivity ϵ , $d^2V/dx^2 = -\rho/\epsilon$, where ρ is the space charge density. Letting $E = -eV$, be the electron energy, Poisson's equation can be rewritten as $d^2E/dx^2 = -\rho/\epsilon$. Assuming donors in the depletion region are completely ionized and ignoring both the minority and majority carriers, $\rho = eN_d$, in the barrier and $\rho = 0$ outside the barrier, we introduce a space charge discontinuity that is wholly artificial but is a zero order description of a metal-semiconductor barrier.

$d^2E/dx^2 = e^2N_d/\epsilon$ in the barrier.

On integration,

$$\frac{dE}{dx} = \frac{e^2N_d}{\epsilon} x \Big|_{\lambda_0}^x = \frac{e^2N_d}{\epsilon} (x-\lambda_0)$$

where λ_0 is the barrier width, defined as the value of x for which the field is zero.

After a second integration

$$E(x) = \frac{e^2N_d}{\epsilon} (x^2/2 - \lambda_0 x) + \text{const.}$$

With the Fermi level regarded as the reference level,

$$E(\lambda_0) = -\frac{e^2N_d\lambda_0^2}{\epsilon} + \text{const} = \phi_n.$$

$$\Rightarrow \text{const.} = \phi_n + \frac{e^2N_d\lambda_0^2}{\epsilon}.$$

$$\text{So } E(x) - \phi_n = \frac{N_d e^2}{2\epsilon} (x - \lambda_0)^2.$$

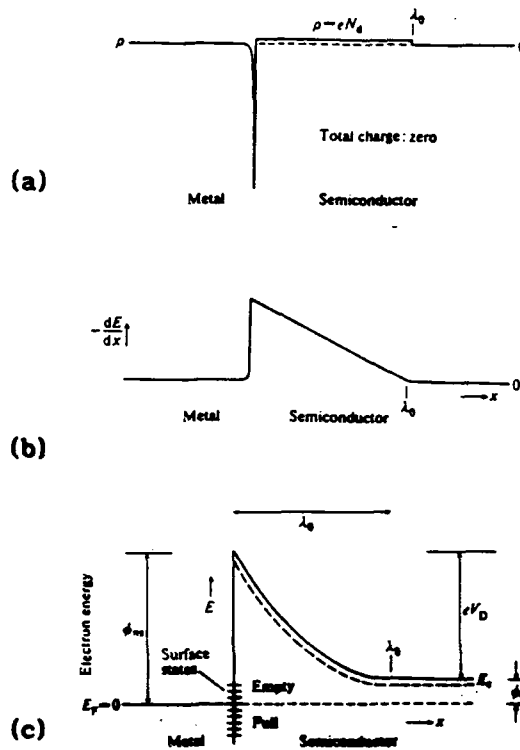


Fig. 19 (a) Space charge density, (b) field, and (c) electron energy at contact.

When $x = 0$, we have $E(0) - \phi_n = \frac{e^2N_d\lambda_0^2}{2\epsilon}$. This is the barrier height seen from the semiconductor side and the diffusion potential is $V_D = \frac{eN_d\lambda_0^2}{2\epsilon}$.

The band picture, used to explain bulk phenomena, of a semiconductor arises because of lattice periodicity. At the surface of a semiconductor the periodicity is interrupted and the usual band picture does not apply at the surface. As a result, surface states exist and act to trap electrons in N-type materials. The electrons are captured from the donors in the bulk before contact and the donors which are no longer compensated extend into the semiconductor a distance λ_0 . The barrier thickness depends on the donor concentration and the barrier height, thus the barrier thickness depends on the energetic position and the number of surface states.

The barrier discussed so far is an abstraction. It presupposes contact between perfectly clean materials. This in general is not the case of experience, where each surface may be covered with an impurity oxide layer or the metal and semiconductor can interact with one another to form a third

phase. The interaction may be inert or a chemical reaction may take place. Often the barrier is too thin (3-20 Å) or disordered to be studied by standard band theory.

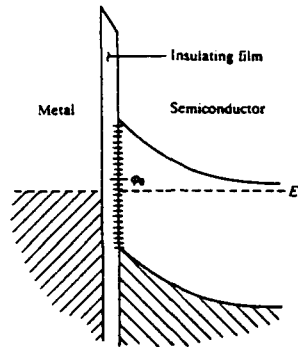


Fig. 20 Metal-semiconductor contact with surface states.

There are four important cases of third phases.

Non-metal	Metal	Comment
(a) near insulator	physically adsorbed	true work function Schottky barrier.
(b) covalent (eg. Ge, Si)	physically adsorbed	work function & surface state dependent.
(c) covalent	forms a compound with non-metal	e.g. silicide contacts
(d) covalent	thin oxide film	e.g. chemically etched silicon.

To a first approximation the most important feature of a contact, the barrier height ϕ_b , is a constant of the two materials. For highly ionic materials, e.g. most group II-VI compound semiconductors, the barrier height is a strongly dependent on the work function of the metal. These materials have a low density of surface states and therefore the Fermi level is unpinned. In contrast group IV and III-IV compounds are highly covalent and it is an experimental fact that the barrier height is $\frac{2}{3}E_g$ for N-type

materials and $\frac{1}{3}E_g$ for P-type materials where E_g is the bandgap. To explain this Bardeen (1947) proposed that the high density of surface states pinned the Fermi level. Fig. 21 shows the bandgap and the Fermi level with respect to the bottom of the conduction band for several semiconductor materials.

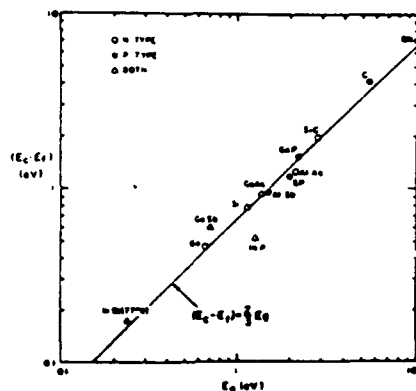


Illustration of the two-thirds rule for barrier height pinning at the metal-semiconductor interface for Au contacts on various covalent semiconductors. The location of the Fermi level relative to the conduction band ($E_c - E_f$) at the interface is plotted vs energy gap E_g (from Ref. [4]).

Fig. 21 Barrier energies for gold on several n-type covalent semiconductors; the straight line is where the barrier energy is 2/3 of the band gap [from C.A. Mead, 1966]

4.4 Current Transport Processes in a Forward Biased Schottky Diode.

Assuming the barrier height has been established, there are four mechanisms via which current can pass across the interface independent of barrier height. The current transport in metal-semiconductor contacts is mainly due to majority carriers, in contrast to p-n junctions in which most current transport is by minority carriers. The mechanisms, illustrated in Fig 22, are (a) emission of electrons from the semiconductor over the top of the barrier into the metal, (b) quantum-mechanical tunneling through the barrier, (c) recombination in the space charge region, (d) recombination in the neutral region ('hole injection').

4.5 Emission over the Barrier.

Before electrons are emitted over the barrier they must first be transported from the interior to the interface, traverse the depletion region subject to the mechanisms of drift and diffusion and on arriving at the interface their emission into the metal is controlled by the number of Bloch states in the metal communicating with states in the semiconductor. These processes are effectively in series and the current is determined by

- (a) emission of electrons from the semiconductor over the top of the barrier into the metal,
- (b) quantum-mechanical tunnelling through the barrier,
- (c) recombination in the space-charge region,
- (d) recombination in the neutral region ('hole injection').

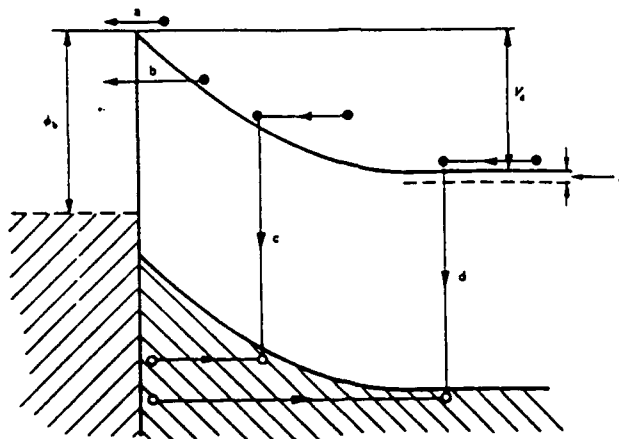


Fig. 22 Transport processes in forward biased Schottky barrier (from Rhoderick and Williams, 1988, p89)

the largest impediment. We assume that the electrons traverse to the interface region the other two processes have been considered as current limiting by Wagner (1931) and Schottky and Spenke (1939) (drift and diffusion) and Bethe (1942) (Bloch states). The difference between these two models is illustrated by the behavior of the quasi-Fermi level for electrons in the semiconductor. (The quasi-Fermi level is a hypothetical energy introduced to describe the behavior of the electron in non-equilibrium conditions. It predicts the number of electrons in the conduction band when equilibrium theory is assumed and the quasi-Fermi level is used in the Fermi-Dirac distribution function.)

In the diffusion theory the concentration of electrons in the semiconductor adjacent to the interface is not altered by the applied bias and the quasi-Fermi level in the semiconductor is equal to the Fermi level in the metal (see Fig. 23). The main obstacle to the flow of current is drift and diffusion in the depletion region. Under the assumptions of thermionic emission of Bethe, electrons emitted from the semiconductor are not in thermal equilibrium with the metal conduction electrons. The energy exceeds the Fermi level by the barrier height. The bottleneck here is due to the process of emission of electrons into the metal.

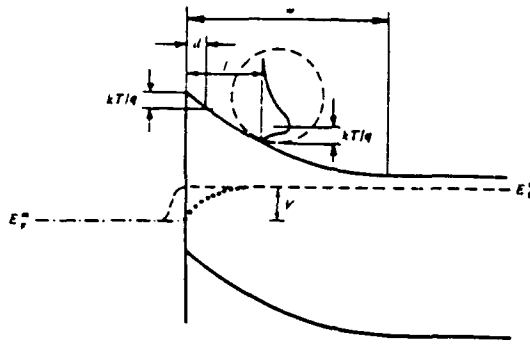


Fig. 23 Electron quasi-Fermi level in a forward-biased Schottky barrier according to diffusion theory, ---- according to thermionic emission theory. The broken circle shows the energy distribution of electrons which make their last collision at a distance l from the interface.

The current density prediction of the diffusion model is

$$J = qN_c \mu \epsilon_{\max} \exp\left(\frac{-q\phi_b}{kT}\right) \left\{ \exp\left(\frac{qV}{kT}\right) - 1 \right\} .$$

The current density for thermionic emission is

$$J = A^* T^2 \exp\left(\frac{-q\phi_b}{kT}\right) \left\{ \exp\left(\frac{qV}{kT}\right) - 1 \right\} ,$$

and that predicted by the work of Crowell and Sze(1966) which combines the two;

$$J = \left(\frac{qN_c V_r}{1 + \frac{V_r}{V_d}} \right) \exp\left(\frac{-q\phi_b}{kT}\right) \left\{ \exp\left(\frac{qV}{kT}\right) - 1 \right\} .$$

These all have the same dependence on ϕ_b and V . Here, V_r is the recombination velocity, V_d is the effective diffusion velocity and N_c is the effective density of states in the conduction band.

4.6 The Schottky Effect

The Schottky effect is the image-force-induced lowering of the potential energy barrier for charge carrier emission when an electric field is applied. Consider a metal-vacuum system first. The minimum energy required for an electron to escape to the vacuum from the Fermi level in a metal is $q\phi_m$ (approx. 2-6 eV). Where $q\phi_m$ is sensitive to metal cleanliness.

When an electron is at a distance x from the metal, a positive charge

is induced on the metal surface. The force of attraction between the electron and the induced positive charge is equivalent to force that would exist between an electron and an equal positive charge located at $-x$. The positive charge is referred to as the image charge. The attractive force, called the image force, is

$$F = \frac{-q^2}{4\pi\epsilon_0 (2x)^2}$$

where ϵ_0 is the permittivity of free space.

Work done by an electron in going from infinity to x is

$$W = \int F dx \qquad W = \int_{\infty}^x \frac{q^2}{16\pi\epsilon_0 x^2} dx$$

This corresponds to the potential energy of an electron at x . When an external field is applied, the total field is

$$PE(x) = \frac{q^2}{16\pi\epsilon_0 x} + qEx \quad (\text{eV})$$

Fig. 24 is the energy band diagram between the metal surface and the vacuum.

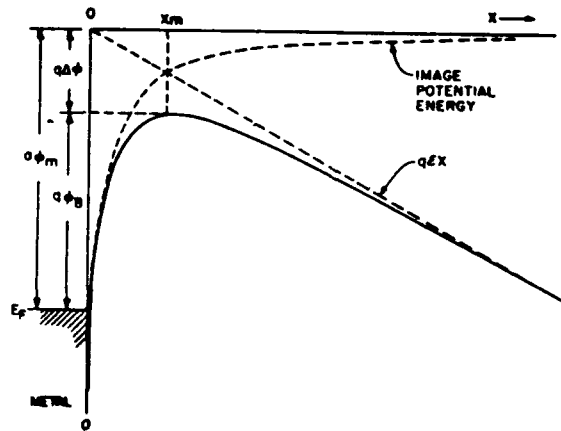


Fig. 24 Energy-band diagram between metal surface and the vacuum. The metal work function is $q\phi_m$. The effective work function or barrier is lowered when the electric field is applied to the surface. The lowering is due to the combined effects of the field and the image force. (After Sze, 1981)

The Schottky barrier lowering (image force lowering) $\Delta\phi$ and the location of the lowering x_m are given by the condition $dPE(x)/dx = 0$.

$$\text{i.e. } \frac{dPE(x)}{dx} = \frac{-q^2}{16\pi\epsilon_0} \frac{1}{x_m^2} + qE$$

So

$$x_m = \left(\frac{q}{16\pi\epsilon_0 E} \right)^{1/2}$$

and

$$q\Delta\phi = PE(x_m) = \frac{q^2}{16\pi\epsilon_0} \left(\frac{16\pi\epsilon_0 E}{q} \right)^{1/2} + qE \left(\frac{q}{16\pi\epsilon_0 E} \right)^{1/2}$$

Hence, $\Delta\phi = 2x_m E$.

These results can also be applied to a semiconductor-metal junction. However, the field should be replaced by the maximum field at the interface and the free space permittivity replaced by the permittivity of the semiconductor, then $\Delta\phi = (qE/4\pi\epsilon_s)^{1/2}$. The value of ϵ_s may be different from the semiconductor static permittivity. For GaAs the image force permittivity for $0 < E^{1/2} < 400$ (V/cm)^{1/2} is expected to be similar to the static value. Because of the larger values of ϵ_s in the metal-semiconductor system, the barrier lowerings are smaller than those of a metal-vacuum system. Although the barrier lowering is small it has a significant effect on the current transport processes in metal-semiconductor systems.

4.7 Tunneling (or Field) Emission Through the Barrier.

Under some circumstances electrons with energies below the top of the barrier penetrate by quantum mechanical tunneling. The current density is of the form

$$J = J_s \exp\left(\frac{V}{E_0}\right), \text{ where } E_0 = E_{00} \coth\left(\frac{qE_{00}}{kT}\right).$$

E_{00} is the diffusion potential of the Schottky barrier and is

$$E_{00} = \frac{h}{4\pi} \left[\frac{N_d}{m^* \epsilon_s} \right]^{1/2}$$

where m^* is the effective mass of an electron.

The current density is proportional to (transition probability) x (occupied probability in semiconductor) x (unoccupied probability) in metal. If the temperature is raised the electrons are excited to higher energy levels and see a thinner and lower barrier, consequently the current density increases. This higher temperature phenomena is known as thermionic field emission and is illustrated in Fig. 25.

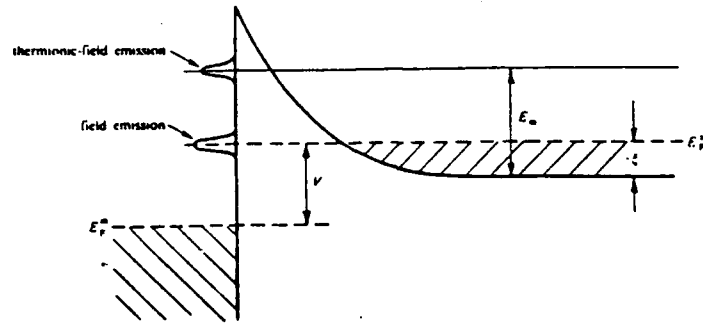


Fig. 25 Field and Thermionic field emission under forward bias. The diagram refers to a degenerately doped semiconductor for which ξ is negative. (Padovini and Stratton, 1966)

4.8 'Ohmic' Contacts and Field Emission

Field emission is important to production of 'Ohmic' contacts. Ohmic contacts do not necessarily obey Ohm's Law but are of low resistance compared to that of the bulk. They are usually Schottky barriers on very highly doped materials. The expression for the contact resistance, R_c , is in general a complicated expression, Yu (1970), but the doping dependence is

$$\exp\left(\frac{\phi_b}{E_{00}}\right) \quad \text{for field emission}$$

$$\exp\left(\frac{q\phi_b}{E_{00} \coth(qE_{00}/kT)}\right) \quad \text{for thermionic field emission}$$

$$\exp\left(\frac{q\phi_b}{kT}\right) \quad \text{for thermionic emission.}$$

where

$$E_{00} = \frac{h}{4\pi} \left[\frac{N_d}{m \epsilon_s} \right]^{1/2}$$

Hence for the field and thermionic and field emission the current increases at higher doping levels.

4.9 Fabrication Techniques.

Ohmic contacts can be fabricated by doping the semiconductor in the contact region. Fabrication requires the deposition of a metal, or mixture of metals, and a dopant followed by an annealing process. The deposition is

by one of a variety of techniques including evaporation, sputtering, pressure contacts, soldering or plating. We chose evaporation. In producing a contact one is faced by a several obstacles. The wetting action of metallic compounds on GaAs is low. The contact materials 'ball up' on annealing forming small islands on the substrate and resulting in a poor contact. When using a mixture of metals it is necessary to evaporate to completion to maintain the correct stoichiometry. The steps in the procedure are

- etch the GaAs substrate to remove oxide layers on the surface
- evaporate and deposit Au-Ge,
- evaporate and deposit Ni,
- anneal to promote interdiffusion,
- evaporate and deposit a metal conducting strip.

Tunneling electron microscopy indicates that the presence of a NiAs(Ge)/GaAs interface (Fig. 26) is important to lower the contact resistance and that carrier transportation via tunneling in Ge doped GaAs could be most important Ogawa (1980) has concluded that high reliability is realized when the Ni layer is thinner than the AuGe and that a rapid anneal to 500 C improves the depth of alloying and the contact character (Fig. 27).

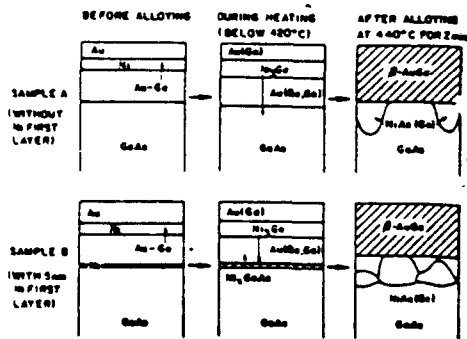


Fig 26 Schematic illustration of the sequence of alloying reactions.

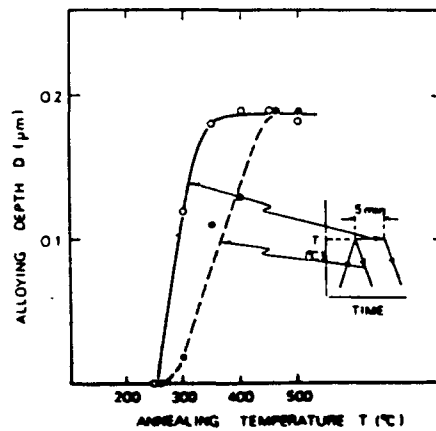


Fig. 27 Alloying depth vs. annealing for two different times at maximum temperature.

Back to back Schottky diodes were fabricated and a chopped, focused laser beam was directed at one contact and then the other (Fig. 28) the resulting output current was oppositely directed when changing from one contact to the other as would be expected (Fig. 29). This indicates that Schottky barriers were indeed fabricated.

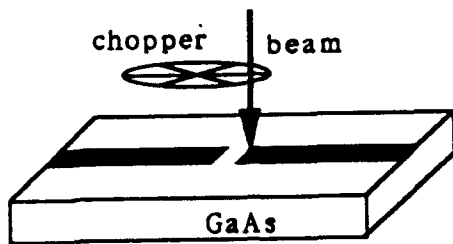


Fig. 28 Geometry of gold electrodes on GaAs substrate illuminated by chopped laser beam.

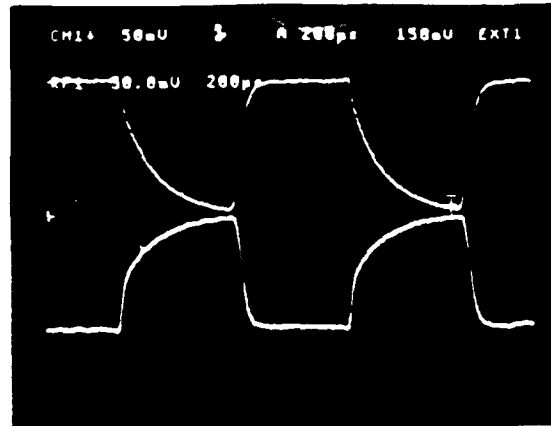


Fig. 29 Current flowing under illumination of one contact (top) and the second (bottom).

Under the assumptions that light changes the barrier by

1. changing the boundary carrier concentration on the bulk side,
2. photoexcitation of traps within the barrier region and subsequent removal of carriers by the high field,
3. the adjustment of the trap occupancies within the space charge region to the new majority and minority carrier concentrations,

Bardeen (1950) and Branbury (1953) obtained an expression for the open circuit voltage

$$V_{oc} = n \frac{kT}{q} \ln \left(\frac{I_1}{I_s} + 1 \right)$$

where I_s is the saturation current, I_1 is the current due to incident

photons and n is the non-ideality factor of the diode. Figure 30 shows the voltage measured by a $1M\Omega$ input impedance oscilloscope across the contact as a function of the incident beam power. The slope of the line for sample 2 is 0.030 and $kT/q = 0.026$ at 300 K. The slope of the curves varies, i.e. n varies. n may take values between 1 and 2. $n = 1$ when diffusion currents dominate and 2 when recombination currents dominate. The curve for sample 6, the sample which was prepared by evaporation to completion, rapidly annealed and on LEC GaAs has the lowest photovoltaic voltage and lowest value of n indicating that it is the most 'Ohmic' of the contacts and that diffusion currents are more important.

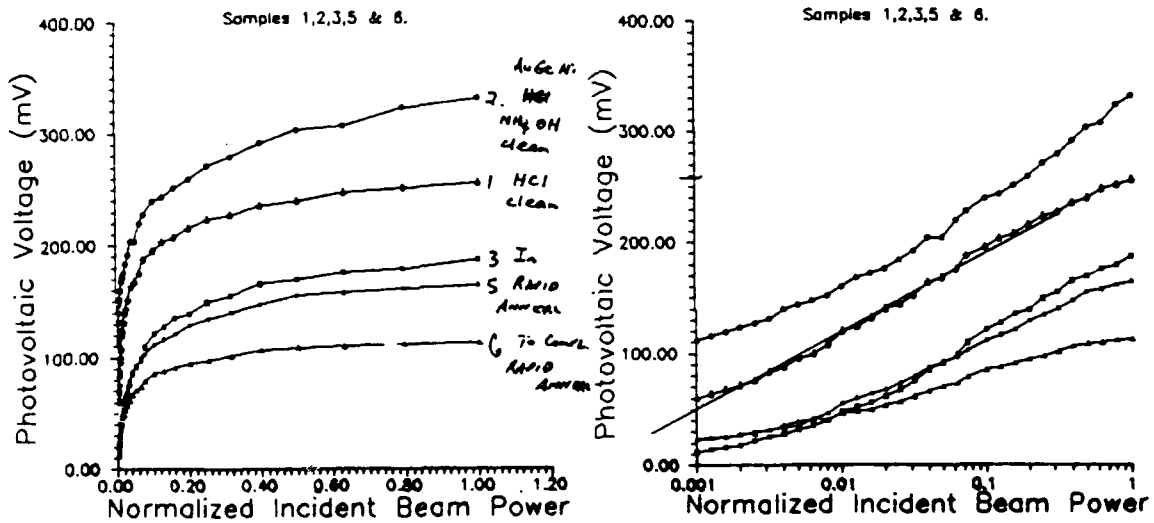


Fig. 30 Photovoltaic response of gold-gallium arsenide contacts to laser illumination.

4.10 Chromium Doped GaAs Switch Response.

Further experimentation with methods of depositing Au/Ge/Ni contacts to Cr:GaAs provided improved contacts as defined by the voltage switched when photoactivated and the time response of the switching circuit. These contacts made feasible the measurement of the switch response to short duration illumination by electro-optic sampling. A detailed description of the technique for contact deposition is provided in appendix B.

To improve the transmission line characteristics over that described

earlier where the fast photodiode was external to the LiTaO_3 electro-optic sampling head, Cr:GaAs was incorporated into the transmission line as shown in Fig. 31. The electrodes continued from the LiTaO_3 across the Cr:GaAs except for a small ($25\ \mu\text{m}$) gap in the top electrode $1\ \text{mm}$ from the $\text{LiTaO}_3/\text{Cr:GaAs}$ interface. An external bias of $6\ \text{volts}$ established a field of $2.4\ \text{KV/cm}$ across the gap which was illuminated from above by $180\ \text{fs}$ FWHM, $76\ \text{MHz}$, $150\ \text{mW}$, $620\ \text{nm}$ laser pulse train.

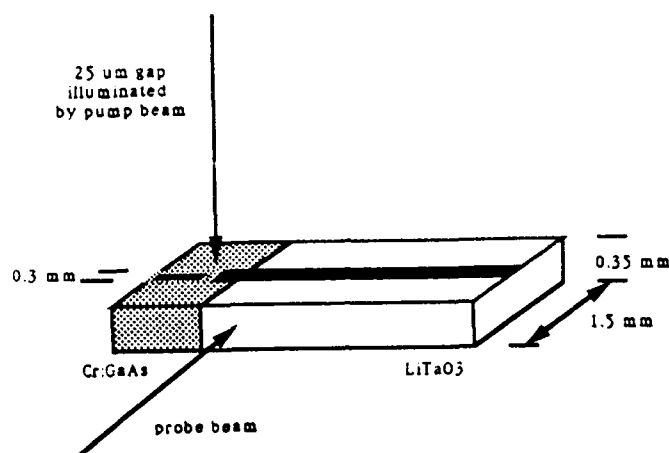


Fig. 31 Cr:GaAs switch incorporated with LiTaO_3 balanced stripline.

This geometry reduced both the number of discontinuities and the distance through which the switching pulse propagated before being sampled. The LiTaO_3 was reduced to $0.35\ \text{mm}$ resulting in a reduced half wave voltage of $2.95\ \text{KV}$. The measured data points are compared in figure 32 with a theoretically determined waveform. This waveform assumes that the voltage pulse decreases exponentially with a (fitted) lifetime of $20\ \text{ps}$ as expected due to charge carrier recombination and that it is reflected from the Cr:GaAs/ LiTaO_3 with a coefficient of $.2886$, determined from the mismatch in the transmission line impedance. The time between successive reflections is $59\ \text{ps}$ as determined from the position of the sampling beam from the edge of the gap and the velocities of the pulse in the two media. Although the peaks align well in time the amplitudes and the shape vary considerably after the first pass of the pulse. Possible reasons for these departures, yet to be confirmed, are that the calculated reflection coefficient is not accurate. This may arise from the use of Hammerstad's expressions for the determination of the characteristic impedance in materials of relative dielectric constant greater than 16 . A value for which their accuracy is not

known. Another obvious shortcoming of the calculated curves are that they make no inclusion of dispersion which is significant for pulses containing high frequency components.

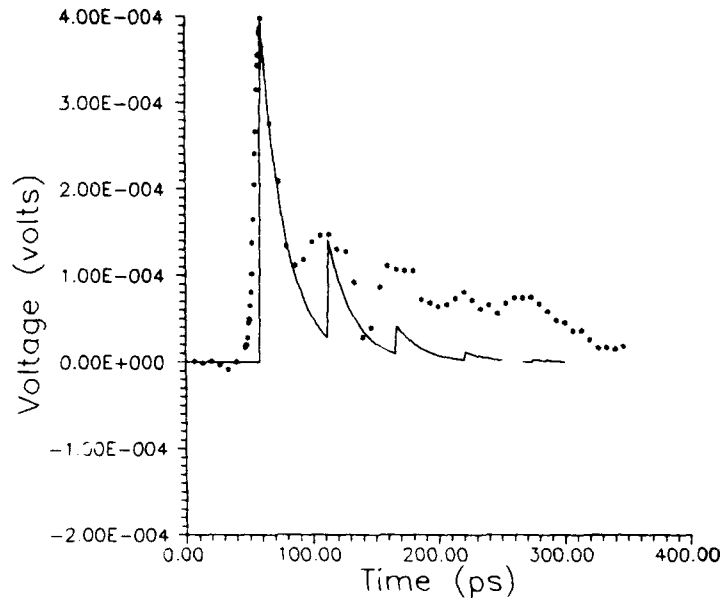


Fig. 32 Electro-optically measured Cr:GaAs switch response to 180 fs FWHM laser pulse.

5.0 Conclusion

An electro-optic sampling system has been demonstrated for measurement of electric fields having variations on ultra-short timescales. The technique has been used to measure the response of both commercially available photodiodes and the photoresponse of biased Cr:GaAs. The field switched in the Cr:GaAs is resolvable because of the lowered impedance of the metal-semiconductor contacts. The contacts are the result of establishing a deposition and annealing procedure for AuGe/Ni on Cr:GaAs. In the absence of such a procedure the photoresponse would not be measurable.

The technique will now be applied to the detailed investigation of electron dynamics in high power semiconductor switches, including the dependence of switching behavior on electric and magnetic fields, and the position of illumination. These investigations will be directed towards the understanding of the persistent photoconductive phenomena known as 'lockon'.

APPENDIX A

Pockels Cell Analysis via Jones Calculus.

The state of polarization of a beam transmitted through numerous optical elements can be determined using Jones calculus. Assume the light to be normally incident on the systems elements, then it is possible to represent the effect of any element on the polarization or intensity as a linear operator acting on the electric vector or the light wave. The operator is represented in the form of a 2 x 2 matrix. In general the effect of an element with different refractive indices and absorption coefficients along the principle axes of the element can be treated. However, we assume absorption is zero.

Assume the y direction is out of the page and we are looking down the y direction from a location at larger y than any element and represent the field in two components.

$$E_x = E_{0x} e^{i(\phi_x + \omega t)} \quad \text{and} \quad E_z = E_{0z} e^{i(\phi_z + \omega t)}.$$

Which we abbreviate to

$$E_x = E_{0x} e^{i(\phi_x)} \quad \text{and} \quad E_z = E_{0z} e^{i(\phi_z)}.$$

The state of polarization of the output of an optical element is related to the input via a matrix known as a *Jones matrix*. For example, consider the change in the polarization state brought about by a linear polarizer orientated at angle ϕ with respect to the x-y coordinate system of Fig.A1 .

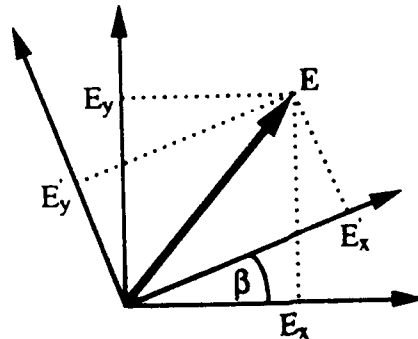


Fig. A1 E components separated by the polarizer rotated to angle ϕ .

$$\begin{pmatrix} E'_x \\ E'_z \end{pmatrix} = \begin{pmatrix} \cos^2 \phi & \sin \phi \cos \phi \\ \cos \phi \sin \phi & \sin^2 \phi \end{pmatrix} \begin{pmatrix} E_x \\ E_z \end{pmatrix}$$

The Pockel's cell Jones matrix

representation is

$$\begin{pmatrix} E'_x \\ E'_z \end{pmatrix} = \frac{1}{2} \begin{pmatrix} \cos\beta & \sin\beta \\ -\sin\beta & \cos\beta \end{pmatrix} \begin{pmatrix} 1 & 0 \\ 0 & e^{i\Gamma} \end{pmatrix} \begin{pmatrix} 1-2\alpha & 1 \\ 1 & 1+2\alpha \end{pmatrix} \begin{pmatrix} E_x \\ E_z \end{pmatrix}$$

(i) (ii) (iii)

where (i) represents the rotation function of the second polarizer at angle β with respect to the z axis, (ii) the total phase shift, and (iii) the polarization matrix of the first polarizer oriented at angle $\alpha + \pi/4$ radians from the z axis, where α is small. After multiplication

$$E'_x{}^2 = \frac{1}{4}[(E_x^2 + E_z^2) - 4\alpha(E_x^2 \cos^2\beta - E_z^2 \sin^2\beta) + \sin 2\beta \cdot \cos\Gamma(E_x^2 + E_z^2) - 2\alpha \sin 2\beta \cos\Gamma(E_x^2 - E_z^2)]$$

$$E'_z{}^2 = \frac{1}{4}[(E_x^2 + E_z^2) - 4\alpha(E_x^2 \sin^2\beta - E_z^2 \cos^2\beta) - \sin 2\beta \cdot \cos\Gamma(E_x^2 + E_z^2) + 2\alpha \sin 2\beta \cos\Gamma(E_x^2 - E_z^2)].$$

These expressions indicate that $E'_x{}^2$ and $E'_z{}^2$ are complicated functions of α and β and that it is of importance to set $\alpha = 0$ and $\beta = \pi/4$. When $\alpha = 0$

$$E'_x{}^2 = \frac{1}{4}[(E_x^2 + E_z^2)(1 + \sin 2\beta \cdot \cos\Gamma)]$$

$$E'_z{}^2 = \frac{1}{4}[(E_x^2 + E_z^2)(1 - \sin 2\beta \cdot \cos\Gamma)]$$

and when $\beta = -\pi/4$

$$E'_x{}^2 = \frac{1}{4}[(E_x^2 + E_z^2)(1 - \cos\Gamma)] = \frac{1}{2}(E_x^2 + E_z^2)\sin^2\Gamma/2$$

$$E'_z{}^2 = \frac{1}{4}[(E_x^2 + E_z^2)(1 + \cos\Gamma)] = \frac{1}{2}(E_x^2 + E_z^2)\cos^2\Gamma/2$$

hence

$$E'_x{}^2 - E'_z{}^2 = \frac{1}{2}(E_x^2 + E_z^2)(\sin^2\Gamma/2 - \cos^2\Gamma/2).$$

$$E'_x{}^2 - E'_z{}^2 = \frac{1}{2}(E_x^2 + E_z^2)[1 - 2\cos^2(\Gamma/2)]$$

Taking the difference between the two signals leads to a doubling in the measured voltage swing for a given change in phase shift. For small Γ both $E'_x{}^2$ and $E'_z{}^2$ have a linear dependence on the introduced phase shift, Fig. A1.

$E'_x{}^2$ and $E'_z{}^2$ are directed to separate diodes, and subsequently to separate inputs of the lockin amplifier differential input. Using the differential input in this manner both increases the signal measured and enables an increased sensitivity measurement to be made.

REFERENCES

- Bahl, I.J. and Trivedi (May 1977), *Microwaves* 174
- Bardeen, J. (1947) *Phys. Rev.* 71 717
- Bethe, H.A. (1942) M.I.T. Radiation Lab. Rep. 43-12
- Buckingham, M.J., '*Noise in Electronic Devices and Systems*', 1983, John Wiley
ISBN 0-470-20164-9
- Carin, L and K.J. Webb, *IEEE Trans. Microwave Theory Tech.* MTT-37 1784
- Chamoun, S.N., R. Joshi, E. Arnold, R. Grondin, K. Meyer, M. Pessot, G. Mourou (1989) *J. Appl. Phys.* 66 236
- Davidov, B (1939) *J. Phys. USSR* 1 167
- Hammerstad, E.O., (1975) *Proc. European Microwave Conference Hamburg (Germany)* 268
- Iverson, A.E., G.M. Wysin, D.L. Smith, and A. Redondo. *Appl. Phys. Lett.* 52 25 1988.
- Khosroffian, J.M. and B.A. Garetz (1983) *Applied Optics* 22 3406
- Kogelnik, H. (1965) *Bell Sys. Tech. J.* 455
- Kolner, B. and D. Bloom (1986) *IEEE J. Quant. Elect.* QE-22 79
- Mead, C.A. (1966) *Solid State Electronics* 9 1029
- Mead, C.A. (1969) '*Ohmic Contact to Semiconductors.*' p 3-16 Ed. by B. Schwartz. Electrochemical Society N.Y.
- Meyer, K., M. Pessot, G. Mourou, R. Grondin and S. Chamoun (1988) *Applied Phys. Lett.* 53 1988
- Nuss, M.C., D.H. Auston and F. Capasso. *Phys. Rev. Lett.* 58 22 2355, 1987
- Ogawa, M. (1980) *J. Appl. Phys.* 5 (1) 406
- Padovini, F.A. and R. Stratton (1966) *Phys. Rev. Lett.* 16 1202
- Rhoderick, E.H. and R.H. Williams (1988) '*Metal-Semiconductor Contacts*' Clarendon Press, Oxford.
- Rodwell, M.J.W., M. Riazat, K.J. Weingarten, B.A. Auld and D.M. Bloom (1986) *IEEE Trans. Microwave Tech.* MTT-34 1356
- Valdmanis, J., G. Mourou and C.W. Gabel (1983), *IEEE J. Quant. Elec.* QE-19 664
- Schottky, W. (1938) *Naturwissenschaftler* 26 843
(1939) *Z. Phys.* 113 367
(1942) *Z. Phys.* 118 539
- Schottky, W. and E. Spenke (1939) *Wiss. Veroff, Siemens-Werken* 18 225

- Schottky, W., Stormer, R. and Waigel, F. (1931) *Z Hochfrequztechnik*, 37 162
- Suzaki, Y and A. Tachibana. (1975) *Applied Optics* 12 2809
- Sze, S.M. (1981) '*Physics of Semiconductor Devices*' John Wiley and Sons, New York.
- Weissenfeld, J., R. Tucker, A. Antreasyan, C. Burrus, A. Taylor, V. Mattera, P. Garbinski (1987) *Appl. Phys. Lett.* 50 1310.
- Yariv, A. and P. Yeh, '*Optical Waves in Crystals*', John Wiley and Sons, 1984.
- Zhang, X.-C., and R.K. Jain (1987) *SPIE* 795 317

Appendix B

Fabrication of GaAs Switches

Materials

1. A doped substrate with one side polished

5mm (0.196 in.) L x 0.135 mm (0.053 in.) w lapped to 0.35 mm (0.014 in.) thick

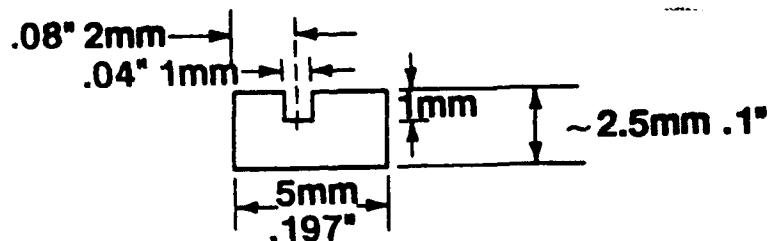
impurity:	Cr
concentration	$8 \times 10^{15} / \text{cm}^3$
resistivity:	$> 10^7 \Omega \text{ cm}$
mobility:	$4000 \text{ cm}^2 / \text{vs}$
thickness:	originally 0.020 inches
Surface direction:	2° off (100)
Estatic	= 12.8
E_{HF}	= 11.0

2. Li Ta O₃ Orientation z parallel to 0.7 mm dimension.

10 mm L x 1.5 mm (0.059) W x 0.7 mm (0.027 in) thick
10 mm 6 x 1.5 mm (0.054 in.) w
x 0.7 mm (0.027 in.) + 0.07 mm W Faces with optical polish, flat,
parallel
1.5 mm W Faces hand lapped and polished

3. Mica Backing

0.0038" thick



4. Au 12% Ge
0.0015 in. thick pieces cut to weigh out exact amount for 500-700 Å thick film when evaporated to completion from Tungsten (W) boat.
5. Nickel wire 99.97% purity 0.010 in. diameter
10 in. wound on Tungsten filament
6. Tra-Con Epoxy
Tra-bond BA-2115

MAJOR STEPS

- I. Deposition of Au 12% Ge (500-600 Å) + Ni (125-150 Å)
- II. High temperature (510-540°C) Alloy
- III. Deposit aluminum (8000Å) electrodes on backs of GaAs + LiTaO₃
- IV. Epoxy GaAs end to LiTaO₃ on mica backing
- V. Deposit aluminum (8000Å) on epoxy junction and over mica and ends
- VI Deposit aluminum (8000Å) electrodes on gap side of assembly with gap masked off.

The following is a detailed description of the above procedures.

Deposit Au 12 % Ge to completion - ~ 600Å thick - on GaAs

I A. Vacuum System - Set-up

1. Diffusion-pumped vacuum system
2. Tungsten (W) "dimple" boat source with 0.0315 gms Au 12% Ge pieces
3. $4\frac{3}{4}$ in. throw - substrate placed directly over source
4. Glow-discharge ring $1\frac{3}{4}$ in. below substrate
5. Quartz crystal oscillator thickness monitor next to substrate
6. Microscope slide plate for thickness measurement on profilometer (Dektak) IIA next to substrate,

Microscope slide next to substrate. Used for thickness measurement on (DEKTAK IIA) after completion of run.

7. Resistance heater over substrate

I B. Clean and Set-up

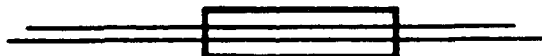
1. Clean substrate

Ultrasonic clean 2 mins. each in trichloroethylene; acetone; methyl alcohol, D.I. H₂O, blow dry with nitrogen. Chemical surface etch:

2 mins. (3) H₃PO₄:(1)H₂O₂:(50) H₂O
5 mins. 20 cc NH₄OH: 7 cc H₂O₂: 97 cc H₂O,
Deionized H₂O rinse and dry nitrogen blow dry

2. Immediately load in mask-substrate holder

The holder centers the GaAs 0.054" polished face over a 0.015 in. wide slot. A 0.001 in. diameter nichrome wire stretched across the slot creates a gap in the AuGe Film contact strip about 0.040 in. from the end of the GaAs



Substrate holder mounted directly over Tungsten boat and Au Ge source to prevent any shadowing of wire masking. Resistance heater sits over holder. Thermocouple on holder to monitor temperature.

I C. Thin Film Deposition Procedure

Pump down to $< 2 \times 10^{-5} \text{T}$
Heat up to $\sim 150^\circ \text{C}$
Cool down to $\sim 80^\circ \text{C}$
Glow-Discharge: 3 mins. 40mA 0.85kv 43mT N₂ 96°C
Pump down to $< 2 \times 10^{-5} \text{T}$

Deposition:

Deposit to completion-to assure proper alloy of Au-Ge-until thickness monitor shows no change
~ 4 kHz change During Deposition - ~ 500-600Åth Typically 80-90 wig 130 sup {o} c.br

Dry N₂ up to atmospheric pressure.

DEPOSIT TOP NICKEL FILM ~ 125Å

Replace W boat + Au Ge with W filament + Ni
GaAs over Ni filament

Without removing from holder, place

Proceed as in IA step C up to deposition

Deposition: 400 Hz change on monitor (shutter controls)

slow DEPOSITION ~ 30 sec.

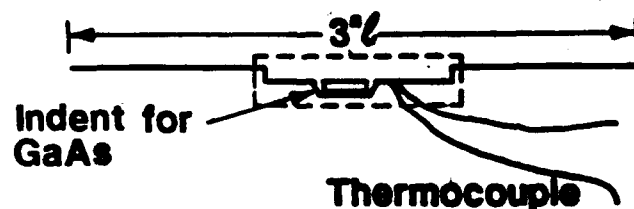
Cool to < 70°C (Dry N₂ ATM)-

EXAMINATION OF FILM -

1. Check width of Gap and " Quality" on digital measuring microscope. If no shadowing and clean edges: ~ 25μ wide then
2. Take picture with filars at edges of Gap,
3. Check thickness of both AuGe and Ni on DEKTAK - print out AuGe:
~ 500-600Å Ni: ~ 125-150Å

II. Alloy-In

Contact deposition for OHMIC contact to GaAs "Rapid Thermal Process": Using Tantalum Boat for rapid heating and cooling



0.005" Tantalum

Ta cover with holes over top to confine heat but let in nitrogen

Nitrogen fed in through needle valve in base plate Weight on bell jar to allow positive pressure of nitrogen

A. Pump down - N₂ flush

Roughing pump and N₂ decrease pressure to 25 mT.

N₂ increase pressure to ~ 1 mm of Hg Several times to flush out other gases

Raise to atmospheric pressure and then POSITIVE PRESSURE with KN₂ Gas flow through a needle valve

B. Heat up in N₂ ATM

Increase the voltage across the tantalum boat in steps.

5V 20 secs.

10V 40in. temperature increased to 340°C

13V 55in. 564°C

~ 12V 5 mins. 30 secs. 540-509°C

(stayed mostly ~ 517°C)

-OFF-

0V 1 min. 63°C

Summary: 55 secs.at temperature increased to 364°C

5 min. 509-540°C (~2½ mins. at 517°C) } positive press N₂ atmosphere

1 min. temperature decreased to 63°C

C. Inspect:

Measure Gap - Take Picture

Gap should be same width as before alloying -

Should be no large globs!!

Very small "Geometric" shapes appear to be preferentially oriented parallel to Gap, across width of GaAs

III. Deposit 8000Å Aluminum Electrodes on Back of GaAs and LiTaO₃

A. Vacuum System

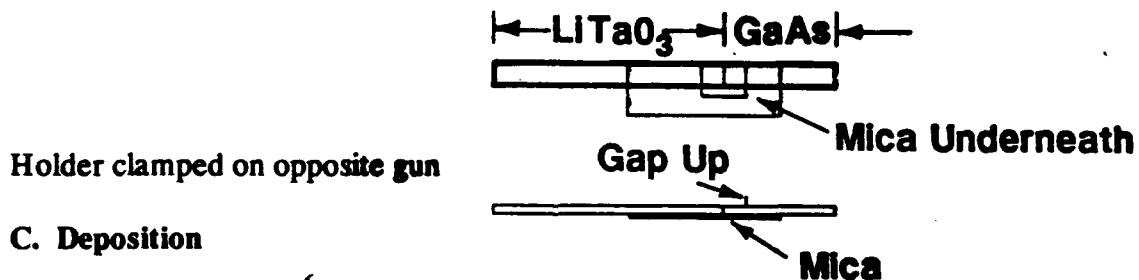
Diffusion pumped system,
Sputter gun with aluminum target,
Throw - Horizontal Gun to Substrates
Glow - Discharge - Ring

- No Heater -

B. Set-Up

- No - Cleaning

Back side of GaAs and 0.054 in. wide hand-polished face of LiTaO₃ over 0.015 in. W slot in holder



C. Deposition

Pump to $< 3.0 \times 10^{-6}$ T

Glow Discharge: 3 mins. 25ma. 85kV - 90mt Argon Pressure

Deposition (Pre-Sputter 5 min.)

FILM DEPOSITION: 8 min. 630V-770 mA 3.0 mT Argon Pressure

8 mm. 630V - 770 ma 3.0mT Argon

cool ~30'

Argon increase pressure to 1000 mT and then introduce air and increase pressure to ATM

IV. EPOXY GaAs TO LiTaO₃ ON MICA BACKING

A special jig is used to line up the GaAs and LiTaO₃ end to end on a mica backing piece. The mica piece is notched at the junction so a thick aluminum film may be deposited after gluing to bridge the gap in the back side electrodes deposited in Step III. Teflon "pushers" from the side, top and end assure flatness and alignment.

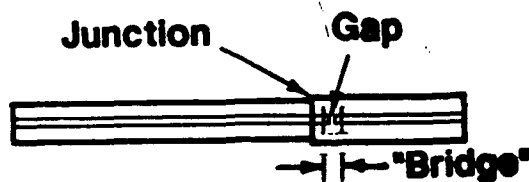
1. Very light film of silicon release agent wiped on jig
2. Small dab of Tra-Con Tra-Bond-2115 put on either side of notch in mica
3. Mica back placed in jig
4. Very small dab of epoxy put on end of LiTaO_3
5. LiTaO_3 now placed in jig, epoxy end centered over notch in mica
6. GaAs, with gap-end nearest junction, now carefully placed in jig
7. Side, top and end "pushers" tightened in place
8. Inspection -- Jig is open underneath at junction so it may be viewed under microscope
9. Cure epoxy: over night or 4 hrs. at 65°C

V. DEPOSIT ALUMINUM 8000Å THICK ON EPOXY JUNCTION -SAME PROCEDURE AS STEP III

1. Clean mica and ends carefully with trichloroethylene on swab.
2. Place epoxied assembly over 0.015 in. wide slot so aluminum is deposited on back side - at junction, on mica and exposed ends.
3. Deposition as in III C.

VI. DEPOSIT ALUMINUM ELECTRODES 8000Å THICK ON SIDE GAP.

1. The epoxied assembly is now placed on the 0.015 in. wide slotted jig so that the gap is centered over a 0.025 wide bridge which masks off the gap. The electrodes are deposited on either side.
2. Deposition as in III C.



APPENDIX B: ABSTRACT OF PAPERS PRESENTED

A TRANSPORT MODEL FOR CARRIERS IN SMALL SPATIAL/TEMPORAL SCALE
COMPOUND SEMICONDUCTOR DEVICES¹

MING-CHENG CHENG, Member of IEEE
Department of Electrical Engineering
University of New Orleans
New Orleans, LA 70148

and

E. E. KUNHARDT, Member of IEEE
Weber Research Institute
Polytechnic University
Farmingdale, NY 11735

Abstract - A non-equilibrium multi-valley transport model for carriers in compound semiconductor devices has been developed. This macroscopic transport model provides an efficient scheme for device modeling, and can overcome the difficulty in evaluating the relaxation times in multi-valley conservation equations without a *a priori* assumption of the displaced-Maxwellian distribution. This model has been successfully applied to modeling of electron transport in GaAs subjected to a rapidly time-varying field.

I. Introduction

Most of transport models that have been used [1]-[6] to account for non-equilibrium phenomena in compound semiconductor devices is based on the single-valley conservation equations. It has been assumed that the energy and momentum relaxation times (τ_e and τ_m , respectively) only depend on mean energy (theoretically, on all moments [7] of the distribution) and is described by the phenomenological equations [3],[4]. In compound semiconductor devices, carrier behavior is described by the distribution in each valley. The distributions in different valleys obey the Boltzmann transport equations (BTEs) that are coupled by intervalley scattering. Consequently, the macroscopic description is given by a set of multi-valley conservation equations. These equations in different valleys are thus coupled by intervalley transitions. However, the relaxation times in multi-valley conservation equations can not be determined from the phenomenological equations [3],[4]. The difficulty in determining these times has led to the fact that the use of conservation equations has assumed [1]-[6] only a single valley where the carrier density, mean energy and average momentum are averaged over all valleys.

In order to determine the relaxation times and to account for intervalley transfer effects, an assumption has been made in most papers [8]-[12] using multi-valley conservation equations that the distribution function in each valley is displaced Maxwellian. These distributions are then used to evaluate the relaxation times. However, this assumption is rather severe since the distribution in compound semiconductors is appreciably different from a displaced Maxwellian.

In this paper, a transport model based on the concept of the Macro-kinetic distribution (MKD) function [7],[13],[14] (whose time scales are characterized by moments of the distribution) has been developed. The description provides an efficient scheme for device modeling, and can account for intervalley transfer effects without a *a priori* assumption of a displaced Maxwellian distribution.

II. Multi-Valley Transport Model

The BTE in each valley is given by

$$\frac{\partial f_i}{\partial t} + \frac{qE}{h} \cdot \nabla_k f_i = \left(\frac{\partial f_i}{\partial t} \right)_{\text{intr}} + \sum_{j=1, j \neq i}^N \left(\frac{\partial f_i}{\partial t} \right)_{\text{int}} + \sum_{j=1, j \neq i}^N \left(\frac{\partial f_i}{\partial t} \right)_{\text{ex}}, \quad (1)$$

where $f_i(k_i)$ is the distribution in the i th valley, N is the number of valleys, k_i is the wave vector, E is the electric field, and h is the Plank constant divided by 2π . The first term of the RHS represents the intravalley scattering, and the intervalley scattering processes out of and into the i th valley are described by the second and third terms, respectively. The carrier density, energy and momentum conservation equations in each valley can be obtained from Eq. (1) by averaging over the distribution, and are written as

$$\frac{\partial n_i}{\partial t} + \nabla \cdot (n_i u_i) = \sum_{j=1, j \neq i}^N n_j v_{ji} - \sum_{j=1, j \neq i}^N n_i v_{ij}, \quad (2)$$

$$\frac{\partial (n_i \bar{p}_i)}{\partial t} + \nabla \cdot (n_i \bar{p}_i \cdot u_i) = qE n_i - \nabla \cdot (n_i k_B T_{ei}) - \frac{n_i \bar{p}_i}{\tau_{mi}} - \sum_{j=1, j \neq i}^N \frac{n_i \bar{p}_i}{\tau_{mj}}, \quad (3)$$

$$\nabla \cdot (n_i \bar{e}_i) + \nabla \cdot [n_i u_i (\bar{e}_i + k_B T_{ei})] = qE \cdot n_i u_i - \frac{n_i (\bar{e}_i - e_g)}{\tau_{ei}} + \sum_{j=1, j \neq i}^N \frac{n_j \bar{e}_j}{\tau_{ej}} - \sum_{j=1, j \neq i}^N \frac{n_i \bar{e}_i}{\tau_{ej}}, \quad (4)$$

where k_B is the Boltzmann constant, and T_{ei} is the electron temperature related to carrier energy \bar{e}_i by

$$\bar{e}_i = \frac{1}{2} m_i^* u_i^2 + \frac{3}{2} k_B T_{ei},$$

m_i^* is the macroscopic effective mass of carriers, and n_i , \bar{p}_i , and u_i are carrier density, average momentum, and average velocity in the i th valley, respectively. The averaged intervalley carrier transition rates (v_{ij}) are defined as

$$n_i v_{ij} = \int P_{ij}(k_p, k_j) f(k_i) dk_i dk_j, \quad (5)$$

where P_{ij} is the transition rate from the i th to j th valley. The intravalley and intervalley momentum exchange times (τ_{mi} and τ_{mj} , respectively) are given by

$$-\frac{n_i \bar{p}_i}{\tau_{mi}} = \int P_i P_{ij}(k_p, k_i) f(k_i) dk_i dk_j - \int P_i f(k_i) dk_i, \quad (6a)$$

$$-\frac{n_i \bar{p}_i}{\tau_{mj}} = - \int P_j f(k_i) dk_i. \quad (6b)$$

and the intravalley and intervalley energy exchange times (τ_{ei} , τ_{ej} , and τ_{ej}) are defined as

$$\frac{n_i (\bar{e}_i - e_g)}{\tau_{ei}} = \int dk_i \int dk_j e_i P_i P_{ij}(k_p, k_i) f(k_i) - \int dk_i \frac{e_i f(k_i)}{\tau_{ei}(k_i)}, \quad (7a)$$

¹supported by the Air Force Office of Scientific Research

$$-\frac{n_i \bar{e}_i}{\tau_{eij}} = -\int dk_i \frac{e_i f_i(k_i)}{\tau_v(k_i)}, \quad (7b)$$

$$\frac{n_j \bar{e}_j}{\tau_{eij}} = \int dk_j \frac{(e_j + \Delta e_{ji} + h\omega_{ji}) f_j(k_j)}{\tau_v(k_j)}, \quad (7c)$$

with

$$\frac{1}{\tau_v(k_i)} = \int P_{ij}(k_p, k_j) dk_j,$$

$$\frac{1}{\tau_u(k_i)} = \int P_{ij}(k_p, k_i') dk_i'.$$

The energy separation between the j th and i th valleys is $\Delta e_{ji} = E_{gj} - E_{gi}$, where E_{gj} (E_{gi}) is the energy gap between the j th (i th) valley and valence band, and $h\omega_{ji}$ is the intervalley phonon energy.

In the previous work, [7],[13],[14] the concept of the MKDs has been introduced to describe carrier behavior in various time scales. Depending on the device scale, a MKD in each valley corresponding to the scale of interest is chosen to evaluate the relaxation times. The coarseness of the macroscopic description, therefore, depends on the choice of the MKD f_M . The choice is based on the fact that, generally, $\tau > \tau_e > \tau_m$ in semiconductors, where τ is the carrier density relaxation time. For example, if the scale of interest is in the order of τ_e , the MKD is chosen to be $f_{Me}(k) = f_{Me}(k, n, \bar{e})$ whose time scale is described by τ and τ_e ; thus f_{Me} contains only information to the scale greater than or as small as τ_e . Similarly, in the scale smaller than τ_e (therefore near τ_m), a higher-resolution MKD can be taken as $f_{Mm}(k) = f_{Mm}(k, n, \bar{e}, \bar{k})$. In this paper, only the energy-time-scale MKD f_{Me} is discussed. The momentum-time-scale MKD f_{Mm} will be studied in the future.

In the energy time scale, the time scale of the carrier distribution in the i th valley can be changed [7],[14] in the form:

$$f_i(k, r, t) = f_{Mei}[k_p, n_i(r, t), \bar{e}_i(r, t)] \quad (8)$$

That is, in the τ_e scale, the space-time dependence of f_i is taken to result from changes in n_i and \bar{e}_i . Using Eq. (8) in the BTE, given in Eq. (1), to change the scale of evolution of the distribution, it leads to a "macro-kinetic" equation for the MDK in the scale of τ_e . The equation for the τ_e -scale MKD has been found to be, for field along z direction

$$qE_{\text{eq}} \frac{\partial f_{Mei}}{\partial k_{zi}} = \left(\frac{\partial f_{Mei}}{\partial t} \right)_e \quad (9a)$$

where

$$qE_{\text{eq}} = \frac{\bar{e}_i(t) - e_i}{u_{ie} \tau_{ei}} \quad (9b)$$

with

$$n_i u_{ie} = \int f_{Mei}(k_p, n_p, \bar{e}_p) u_i dk_i. \quad (9c)$$

u_i is the carrier velocity. Eq. (9a) represents a distribution that obeys a steady-state BTE with a time-varying "equivalent" field of the i th valley, E_{eq} as the driving field, and E_{eq} is given by Eq. (9b) in terms of \bar{e}_i . This MKD thus responds instantaneously to E_{eq}

and the information in the time scale smaller than τ_{ei} is filtered. f_{Mei} can be obtained from Eq. (9a) in terms of E_{eq} or \bar{e}_i , and the relaxation times or rates in each valley can be evaluated from the integrals given in Eqs.(5)-(7) using f_{Mei} . These rates or times are, therefore, tabulated for solving the multi-valley conservation equations given in Eqs. (2)-(4).

III. Results and Conclusion

The developed multi-valley transport model has been applied to the study of electron transport in GaAs subjected to a step electric field of finite rise time. The velocity response to the step change in field is shown in Fig. 1 where included are results obtained from the developed multi-valley transport model, Monte Carlo simulations using a multi-valley band model, and the single-valley approximation. The average velocity, shown in Fig. 1, obtained from the single-valley conservation equations is very similar to the previous results given in [5]; i.e. the single-valley approximation leads to faster relaxation than the Monte Carlo simulations. This is due to the fact that at the applied field electron behavior strongly depends on the intervalley scattering. The single-valley approach can not properly account for slower averaged intervalley transitions, and thus results in faster response. However, as can be seen in Fig. 1, the multi-valley transport model can take into account the intervalley transfer, and therefore provides a better description than the single-valley approach.

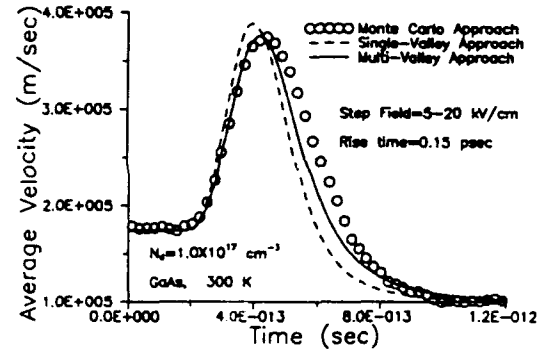


Fig. 1. Average velocity of electrons in n-type GaAs subjected to a step change in field.

References

- [1] W.R. Curtice and Y.H. Yun, IEEE Trans. Elect. Dev. ED-28, 954 (1981).
- [2] T.J. Maloney and J. Frey, J. Appl. Phys. 48, 781 (1977).
- [3] M. Shur, Elect. Lett. 12, 615 (1976).
- [4] R.S. Huang and P.H. Sadbrooke, J. Appl. Phys. 48, 4791 (1977).
- [5] B. Carnez, A. Cappy, A. Kaszynski, E. Constant, and G. Salmer, J. Appl. Phys. 51, 786 (1980).
- [6] N. Goldsman, J. Frey, IEEE Trans. Elect. Dev. ED-35, 1524 (1988).
- [7] E.E. Kunhardt, M. Cheng, and J. Wu, J. Appl. Phys. 64, 1220 (1988).
- [8] T. Toyabe and H. Kodera, Jpn. J. Appl. Phys. 13, 1404 (1974).
- [9] K. Blotekjaer, IEEE Electron Dev. ED-17, 38 (1970).
- [10] D. Jones and H.D. Rees, Elect. Lett. 8, 566 (1972); Elect. Lett. 8, 363 (1972); Elect. Lett. 9, 105 (1973).
- [11] R. Bosch and H.N. Thim, IEEE Trans. Elect. Dev. ED-21, 16 (1974).
- [12] E. Rosencher, J. Phys. 42, C7-351 (1981).
- [13] M. Cheng and E.E. Kunhardt, J. Appl. Phys. 67, 1907(1990).
- [14] Ming-Cheng Cheng, "Non-Equilibrium Transport of Carriers in Multi-Valley Semiconductors", Ph.D. Dissertation, Polytechnic University, 1990.